



Università Campus Bio-Medico di Roma

School of Engineering

PhD Course in Biomedical Engineering

(XXIX – 2014/2016)

**Tactile Sensing System for Biomechatronic Prosthetic
Hands and Grasp Analysis**

Rocco Antonio Romeo

Coordinator

Prof. Giulio Iannello

Supervisor

Prof. Loredana Zollo

Co-supervisor

Prof. Eugenio Guglielmelli

July 2017

Tesi di dottorato in Bioingegneria e bioscienze, di Rocco Romeo,
discussa presso l'Università Campus Bio-Medico di Roma in data 16/10/2017.
La disseminazione e la riproduzione di questo documento sono consentite per scopi di didattica e ricerca,
a condizione che ne venga citata la fonte.

Tactile Sensing System for Biomechatronic Prosthetic Hands and Grasp Analysis

A thesis presented by

Rocco Antonio Romeo

in partial fulfillments of the requirements of the degree of

Philosophiae Doctor

in Biomedical Engineering

Coordinator

Prof. Giulio Iannello

Supervisor

Prof. Loredana Zollo

Co-supervisor

Prof. Eugenio Guglielmelli

July 2017

Tesi di dottorato in Bioingegneria e bioscienze, di Rocco Romeo,
discussa presso l'Università Campus Bio-Medico di Roma in data 16/10/2017.
La disseminazione e la riproduzione di questo documento sono consentite per scopi di didattica e ricerca,
a condizione che ne venga citata la fonte.

Table of contents

Abstract.....	8
Chapter 1 Introduction.....	12
Chapter 2 Instrumented objects for grasp force analysis.....	18
2.1 The humand hand: anatomy and functionality.....	19
2.1.1 Bones and joints.....	19
2.1.2 Muscles.....	20
2.1.3 Hand movements.....	23
2.2 Tools for studying grasping forces: instrumented objects.....	25
2.2.1 Different approaches: background.....	25
2.2.2 The proposed approach: force sensors coupled with accelerometer.....	27
2.3 Set of instrumented objects: features.....	28
2.3.1 Design of the objects.....	29
2.3.2 Tactile sensing: sensing element and electrical design....	32
2.3.3 Static calibration.....	35
2.3.4 Slip detection: sensing element and electrical design.....	38
2.3.5 Accelerometer as an inclinometer.....	43
2.4 Experimental validation and results.....	47
2.4.1 Force measurement: comparison with ground truth.....	47
2.4.2 Slip detection: validation though automated set-up.....	49
2.4.3 Validation on human subject.....	52

2.5	Experimental session with human subject.....	54
2.5.1	Grasping forces.....	55
2.5.2	Object orientation and grasping forces dynamic compensation.....	58
2.5.3	Slip detection.....	61
2.6	Conclusions.....	64
Chapter 3	Prosthesis sensorization.....	67
3.1	Sense of touch: classifications.....	69
3.1.1	Sense of touch: definitions.....	69
3.1.2	Sense of touch: neurophysiology.....	70
3.1.3	Skin mechanics and information encoding.....	71
3.2	State of the art on tactile sensing for prosthetic hands.....	73
3.2.1	Sensorized prosthetic hands: state of art.....	74
3.2.2	Artificial tactile systems: specifications.....	78
3.3	The proposed tactile sensory system.....	80
3.3.1	Tactile sensitive elements.....	80
3.3.2	Tactile sensors positioning.....	84
3.4	Sensory system: integration in the IH2 hand.....	86
3.4.1	CAD design: mechanical parts.....	86
3.4.2	Sensors data acquisition.....	89
3.5	Optimal positioning.....	93
3.6	Conclusions.....	98
Chapter 4	Slip detection algorithm.....	102

4.1 Slip detection: from classical approaches to the proposed one.....	103
4.1.1 Slip detection in prosthetics: state of the art.....	103
4.1.2 Slip detection: proposed approach.....	105
4.2 Slip detection procedure.....	106
4.2.1 Block 1 – Filter network.....	108
4.2.2 Block 2 – Rectification and exponentiation.....	110
4.2.3 Block 3 – Envelop.....	111
4.3 Experimental setup.....	113
4.3.1 Sensors: brief description.....	113
4.3.2 Experimental protocol and set-ups.....	115
4.4 Experimental validation and results.....	117
4.4.1 MEMS sensors.....	119
4.4.2 FSR sensors.....	130
4.4.3 Strain gauge sensors.....	137
4.4.4 Online application.....	138
4.5 Conclusions.....	144
Chapter 5 Conclusions and future works.....	147
5.1 Work overview.....	147
5.2 Future works.....	151
Bibliography.....	155
List of publications.....	167

Tesi di dottorato in Bioingegneria e bioscienze, di Rocco Romeo,
discussa presso l'Università Campus Bio-Medico di Roma in data 16/10/2017.
La disseminazione e la riproduzione di questo documento sono consentite per scopi di didattica e ricerca,
a condizione che ne venga citata la fonte.

Abstract

The development of the artificial tactile sensing began in the 1970s. During the last decades, tactile sensors based on different sensing principles have been developed; the emulation of the physiological sense of touch has gained growing interest in fields such as robotics, as the modern robots are increasingly moving towards *unstructured* environments. Thus, the acquisition of information about interaction forces and surface properties (such as roughness, hardness, shape etc.) became highly desirable. Several technological solutions have been employed to design tactile sensors; nonetheless, their inclusion within artificial systems still remains problematic in several fields. This is also true when the prosthetic domain is considered. Although tactile sensing is an essential element for autonomous dexterous manipulation, no prosthesis endowed with tactile sensors is available in the market.

The present PhD thesis deals with the *sensorization* of a mechatronic, prosthetic hand, featuring the twofold objective of: i) allowing the control system embedded in such a prosthesis to use sensory information in a closed-loop control, optimizing the applied forces (e.g., during a grasping task) and preventing the manipulated object from slipping; ii) providing the prosthesis user with the aforementioned sensory information, obtaining a closed-loop system which gives the amputee the possibility to properly interact with the external world through the tactile feedback.

Starting from the study of human and robotic hands, particularly in terms of tactile characteristics, a solution for an artificial sensory system adoptable for prosthetic hands has been elaborated. This system has been evaluated on a mechatronic hand, namely IH2 Azzurra (Prensilia srl, Pontedera, Italy), similar to the commercial ones but conceived for

research scenarios and thus open to both hardware and software modifications.

In order to understand the pressure applied onto the objects and its hardness level, force regulation is crucial as well as the avoidance of slippage events. To this end, force and slip sensors are needed for an effective prosthesis sensorization. With the aim of deepening the comprehension of the aforementioned applied pressure, a preliminary evaluation of the grasping forces exerted by human subjects has been done by means of *instrumented* objects, purposely designed (through CAD software) and developed. These objects have common shapes and dimensions as objects of daily life, but are equipped with sensors for monitoring various physical quantities (such as force, acceleration, temperature etc.). The developed objects have been provided with piezo-resistive sensors for force measurement and with an accelerometer for estimating object orientation and detecting slippage. Suitability for the performance of some Activities of Daily Living (ADLs), such as bi-digital and tri-digital grasps, has driven the design of the objects. The quantities measured with the objects can help obtain insight into the grasping strategies employed by the users.

The objective of measuring the force levels applied by an artificial hand can be accomplished by means of tactile sensors. This leads to the sensorization of the above mentioned prosthetic hand. First, a given transduction technology has been chosen within the available ones for the force measurement. This choice has been followed by the identification of the areas to sensorize, which have coincided with the five fingertips, with the metacarpophalangeal joints (MCP) and with the thenar eminence. These areas have been redesigned through CAD software for the inclusion of tactile sensors, given that the IH2 Azzurra (hereafter indicated as IH2) is not equipped with this kind of sensors.

Piezo-resistive sensors have been employed: opportune circuitry has been developed for the conversion of the sensors output (i.e., electrical resistance variation) into a force signal, with the realization of dedicated PCBs for the sensors output collection and conditioning. Moreover, an algorithm for identification of slip phenomena has been developed. This algorithm can be easily applied on the force sensor output, allowing the measurement of the force and the generation of an ON/OFF signal relating to the presence or absence of slip events during grasp. The algorithm has rigorously been validated on different typologies of resistive sensors and used for an online implementation into a prosthetic control.

Tesi di dottorato in Bioingegneria e bioscienze, di Rocco Romeo,
discussa presso l'Università Campus Bio-Medico di Roma in data 16/10/2017.
La disseminazione e la riproduzione di questo documento sono consentite per scopi di didattica e ricerca,
a condizione che ne venga citata la fonte.

Chapter 1 Introduction

Due to its capability of interacting with a wide number of objects, the human hand is considered as the highest example of a *dexterous* system.

In many application fields, the importance of artificial hands is in continuous growth, ranging from robotics to rehabilitation, from tele-manipulation to prosthetics and to humanoid robotics. The latter two require a high dexterity, which is fundamental to assure a high variability of movements in relation to different objects to grasp and manipulate and to guarantee a safe and natural human-robot interaction (Lee, 1999). Consequently, an important challenge in the development of artificial hands is to confer the capability of mimicking the human dexterity, in terms of versatility and manipulation skills.

Moreover, the development of dexterous artificial hands assigns a fundamental role to the human grasp analysis, both in neuroscience and robotics, as well as in biomechanics. In neuroscience, the characterization of the grasping strategies is useful to understand how our brain controls and adapts hand motions and forces applied to accomplish different types of task (Serio, 2014). In robotics, the knowledge and the studies of the human hand can inspire robot hand control algorithms, paving the way to bio-inspired algorithms. However, it must be pointed out that, even if hand posture recordings are today quite easy to obtain, e.g. with motion capture systems, the measurement of forces and torques that the hand exerts on the object is still more difficult than can be imagined.

Concerning the field of prosthetics, the most ambitious challenge is related to the development of prosthetic hands capable to achieve performance comparable to the human hand. To this end, considering

the Activities of Daily Living (ADLs), different issues need to be addressed. These are: the control of a high number of degrees of freedom, the restoration of the sense of touch, slippage control, and the restoration of the bidirectional link between the device and subject's peripheral nervous systems (Raspopovic, 2014).

The present thesis is focused on the study of human grasping, and on providing advancements about the tactile sensorization of biomechatronic hands, with particular attention to the prosthetic domain. The first task might take advantage of purposely developed objects, i.e. instrumented objects. Such objects, with common shape and dimension, embed various sensors for the measurement of several physical quantities. Force, torque, slippage, temperature, velocity, acceleration etc. can be detected by means of one or more instrumented objects. In particular, the found force values might constitute an input for the prosthetic hand control system, as they can be set as reference values. Additionally, instrumented objects can allow comparing the performance of artificial hands with respect to the human one, especially in terms of applied forces.

Tactile sensing is fundamental for enhancing the performance of a robotic hand. It is well known that one of the main limitations of robotic end-effectors resides in the lack of reliable tactile perception; robots are usually called to operate in structured environments, interacting with a priori known items (Kapassov, 2015). Control algorithms which are embedded into the robots usually do not foresee the use of tactile information, relying rather on the aprioristic knowledge of the environment. Nevertheless, in the last years the interaction of robots with the surrounding environment is increasingly moving towards the inclusion of human beings, in addition to unanimated objects; i.e., unstructured environments are becoming highly common. Thus, a

major adaptability comes to be necessary; in this sense, fine manipulation and grasping capabilities are highly desirable for robotic hands/grippers. Such capabilities imply the necessity of tactile systems able to gather information about the objects properties, e.g. shape and hardness, and about the interaction forces with the object itself.

A crucial issue, both in human and in artificial tactile sensing, is to properly detect the slippage phenomena that may occur during manipulation and grasping. Robotic hands should be able to control slip events in a dexterous manner, avoiding the damage of the object as well as grasp instability. While the robot performs an action, unpredictable events might occur, hindering the success of the action itself. This situation results particularly problematic when the action involves the manipulation of an object; the availability of control strategies relying on tactile data could greatly improve the robot ability when facing such a situation.

To date, the number of applications using tactile information is limited (Kapassov, 2015). Robotic end-effectors mainly act within structured environments, and even when endowed with any kind of tactile sensory system, the dexterity of the human hand is highly difficult to be achieved. For this reason, increasing the robustness of the tactile information can predispose the robots towards a more natural behavior, including e.g. the reaction to unexpected events and situations. Hence, sensory feedback from tactile sensors would be of great help in many domains, such as robotic manipulation. In this context, particular benefit might be achieved by the prosthetic field. The current state of art regarding commercial prosthetic hands reports only one case of device provided with a feedback, employed for slip control, from tactile or force sensors (Ciancio, 2016); this confirms that tactile sensing technologies are not easily applicable to prosthetic systems yet.

Besides, it is worth noticing that the number of research groups and activities focused on tactile investigation has traditionally been minor than on other sensing principles investigation (e.g., artificial vision), thus leading to a slower development of the tactile technology (Dahiya, 2013).

As a consequence, prosthetic devices do not allow the user to reliably control slip events; nonetheless, considerable effort has been produced since the late years of 1980s in order to integrate slip information in the prosthesis control system (Francomano, 2013). It is rare to find a prosthetic hand with a tactile sensory system, and even rarer to include in such a system a dedicated information which is relevant to the slippage. This implies the lack of tactile feedback, and consequently the impossibility for the prosthesis wearer to regulate the applied pressure levels onto the grasped objects, and even less so to manage slip events occurring during manipulation. The importance of the tactile sensing is twofold: it would not only allow the control system of the prosthetic device to modify the forces that the prosthesis is exerting, but would put its user in the condition to *sense* again the touched objects. That is, it would increase the naturalness of every grasping and manipulation task, which comes to be significantly damaged when (at least) one of the natural hands is lost.

In light of these considerations, the aims of the research presented here have been the following:

- Development of instrumented objects for biomechanical analysis of human grasp. The main activities have regarded:
 - Design and fabrication;
 - Validation experiments with both robotic and human hand;
 - Experimental session with human healthy subjects;

- Sensorization of a mechatronic hand prosthesis for grasp and manipulation control. The main activities have regarded:
 - Force sensors calibration and output conditioning;
 - Development of a slip detection algorithm;
 - Integration of the sensory system in the prosthesis and experimental validation;

The contents of this thesis are organized as follows:

- ❖ *Chapter 2* is focused on the study of the human grasping, and provides an overview of the state of the art on instrumented objects for force analysis. In this context, three instrumented objects have been developed; the features, as well as the design and fabrication of the developed instrumented objects will be shown, together with the validation procedure executed by means of a robotic hand (namely DLR/HIT Hand II) acting as ground truth and the experimental results obtained on the human hand.
- ❖ *Chapter 3* illustrates the tactile sensory system developed for prosthetic application, with particular attention to the adopted transducing principle (e.g., piezo-resistive). After the presentation of the state of the art regarding both the research and the commercial prosthetic hands, the characteristics (metrology, response etc.) of the chosen tactile force sensors will be described, as well as their integration within a prosthetic hand (IH2 by Prensilia srl). Moreover, the new CAD prosthesis parts designed for hosting the sensors will be shown.
- ❖ In *Chapter 4* an overall state of the art about the slip detection procedures used in robotics and prosthetics will be reported; subsequently, a novel method for slippage detection will be

described. It makes use only of one input signal (e.g., the normal force) measured through a resistive sensor, leading to an ON/OFF slip information. Indeed, it is well known the difficulty of measuring slippage events starting only from normal force amplitude (Van Ho, 2014); by applying the proposed method to the voltage output of a simple, low cost mono-axial sensor (i.e., normal axis), it is possible to obtain information about slippage along with the force information itself.

- ❖ *Chapter 5* is dedicated to the conclusions of the work, starting from the results obtained on all the presented experiments. The main achievements from every activity will be summarized in this Chapter, including the sensorized objects, the sensory system, its integration in the IH2 hand and the slip detection algorithm. Finally, future research activities will be listed.

Chapter 2 Instrumented objects for grasp force analysis

Given its capabilities, its sophisticated kinematics and dynamics, its surprisingly high number of DoF (Degrees of Freedom), the human hand can be considered the most complex organ of the human body after the brain. The complex mechanical structure, the composite sensory system and the bidirectional communication between hand and brain make the human hand capable to accomplish a wide variety of tasks with a high level of versatility. The dexterity of hand manipulation is a distinctive feature of human beings that current humanoid robots can barely replicate. Nonetheless, human hands can be regarded as a benchmark for the design of future artificial hands. The study of the human hand features is the starting point for the design and control of anthropomorphic robotic hands. To this end, force analysis during grasping is a fundamental issue to face while studying human grasping strategies, as well as robotic grasping capabilities.

In this Chapter, hints about the human hand anatomy and functionalities, as well as about the use of instrumented tools for prehension forces analysis will be reported. Then, the new instrumented objects developed in this study will be described, focusing on their characteristics and the validation procedures followed.

Graphic and textual excerpts have been reused from (Romeo, 2015) and (Romeo, 2017a); such excerpts have totally been created by the candidate himself, who is also the first author of the cited papers.

2.1 Human hand: anatomy and functionality

The structure of the human hand can be studied in terms of bones and associated joints and muscles.

2.1.1 Bones and joints

The skeletal structure of the human hand (Figure 2.1b) includes (Schwarz, 1955):

- 8 carpal bones composing the wrist;
- 5 metacarpal bones composing the palm;
- 14 phalangeal bones composing the digits.

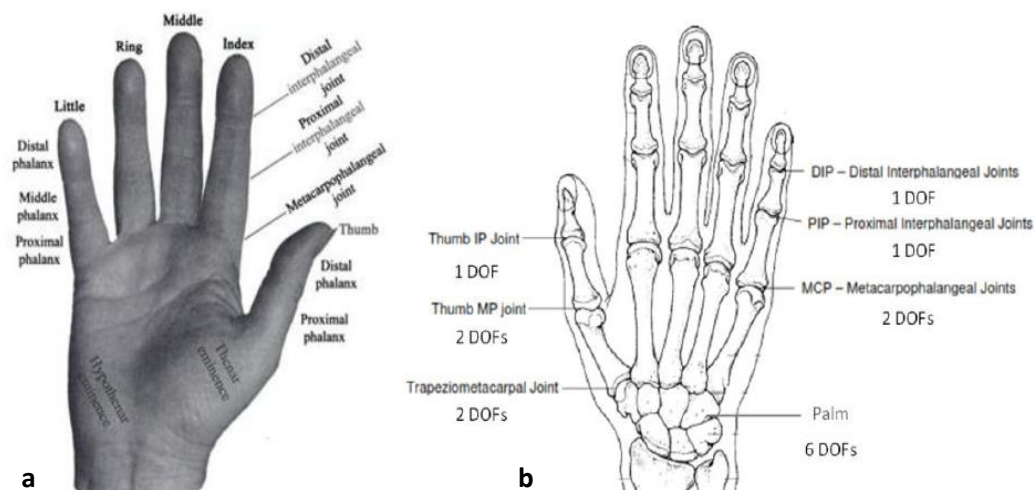


Figure 2.1. Standard nomenclature of the human hand (a); DOFs and joints of the human hand (b). (Jones, 2006).

Manipulation skills are mainly due to the fingers. Each finger has three bones, which are: Proximal Phalanx, Middle Phalanx and Distal Phalanx. The thumb makes exception, being composed of Proximal and Distal phalanges only (Figure 2.1a).

The number of DOFs of the human hand is quite high. More in detail, there are 4 DOFs for each long finger (index, middle, ring and little), of which 3 are deputed to flexion/extension and the remaining is for

adduction/abduction, 5 DOFS for the thumb with and finally 6 DOFs of rotational and translational wrist movements (Agur, 1999).

Long fingers include 3 joints: Metacarpophalangeal (MCP), Proximal Interphalangeal (PIP) and Distal Interphalangeal (DIP). The MCP joint is characterized by 2 DOFs, i.e. adduction/abduction and flexion/extension. The PIP and DIP joints have both 1 flexion/extension DOF only.

The thumb differs from other digits because it does not feature the middle phalanx. Nonetheless, the Trapeziometacarpal (TMC) joint, also known as Carpometacarpal (CMC) joint (regarded as a saddle joint), confers to the thumb 2 more DOFs: adduction/abduction and flexion/extension. The MCP joint of the thumb is characterized by two DOFs, similarly to the long fingers. The fifth DOF (flexion/extension) of the thumb is given by the Inter-Phalangeal (IP) joint.

2.1.2 Muscles

The human hand and wrist movements are controlled by 29 muscles (Jones, 2006). The majority of them are located in the forearm and are called *extrinsic* hand muscles (Figure 2.2).

Three functional groups of these muscles (Agur, 1999) are located in the anterior side of the forearm and arranged in three layers (Figure 2.2a): the superficial layer consisting in four muscles (Pronator Teres, Flexor Carpi Radialis, Palmaris Longus and Flexor Carpi Ulnaris), middle layer consisting of one muscle (Flexor Digitorum Superficialis) and profundus layer (Flexor Digitorum Profundus, Flexor Pollicis Longus and Pronator Quadratus). These muscles can be also classified in relation to the type of movement supported: forearm pronator (Pronator Teres and Pronator Quadratus), wrist flexors (Flexor Carpi Radialis, Flexor Carpi Ulnaris, Palmaris Longus) and flexors of long

fingers (Flexor Digitorum Superficialis and Flexor Digitorum Profundus) and thumb (Flexor Pollicis Longus).

The muscles of the posterior side of the forearm compose two groups arranged in two levels (Figure 2.2b): superficial group (Brachioradialis, Extensor Carpi Radialis Longus, Extensor Carpi Radialis Brevis, Extensor Digitorum, Extensor Digiti Minimi, Extensor Carpi Ulnaris, Anconeus), and deep group (Supinator, Abductor Pollicis Longus, Extensor Pollicis Longus and Extensor Indicis). On the basis of the movement, the muscles can be classified in: forearm supinator (Brachioradialis, Supinator), elbow extensor (Anconeus), wrist extensor (Extensor Carpi Radialis Longus and Brevis, Extensor Carpi Ulnaris) and extensor of long fingers (Extensor Digitorum, Extensor Digiti Minimi, Extensor Indicis) and thumb (Extensor Pollicis Longus and Brevis).

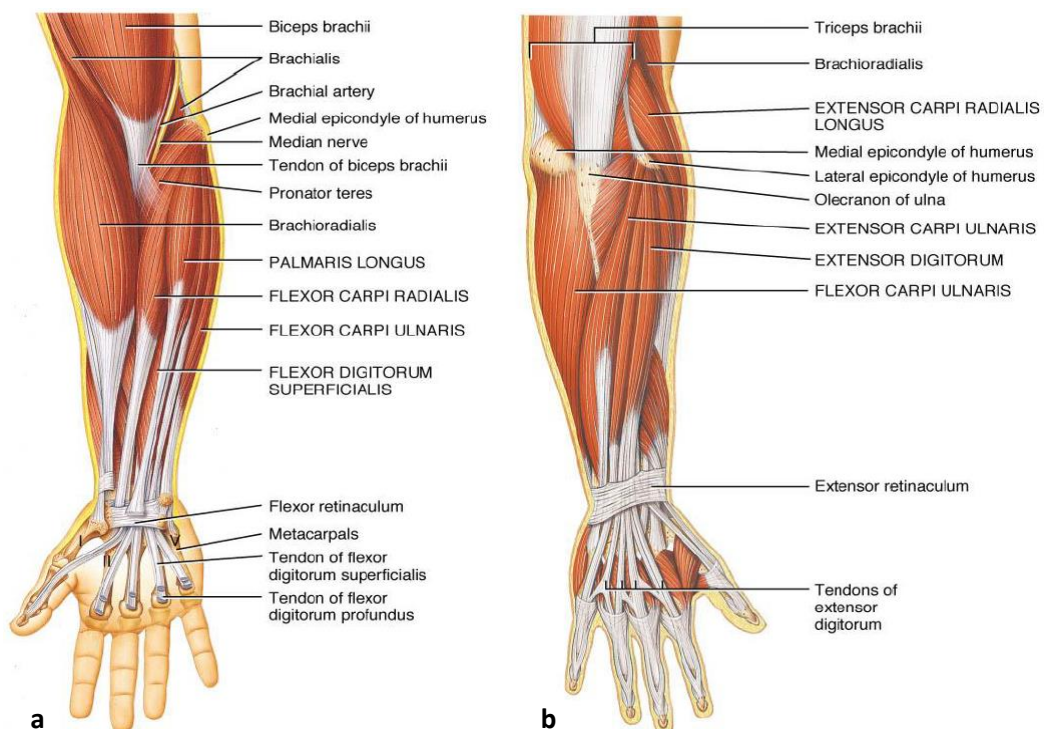


Figure 2.2. Extrinsic muscles of the human hand. Anterior side view (a); posterior side view (b).

The intrinsic muscles located in the hand are grouped in Figure 2.3: Thenar, Hypotenar, Interossei and Lumbricals muscles. The thenar muscles are responsible of the thumb movements: abduction (Abductor Pollicis Brevis), flexion (Flexor Pollicis Brevis) and opposition (Opponens Pollicis). The Hypotenar muscles control the little finger motion: abduction (Abduction Digiti Minimi), flexion (Flexor Digiti Minimi Brevis) and opposition (Opponens Digiti Minimi). The Interossei muscles are positioned both in the dorsum and in the palm of the hand: four Dorsal Interossei and three Palmar Interossei responsible respectively for the abduction and adduction of long fingers. The four Lumbrical muscles are involved in the flexion of the metacarpophalangeal joints and in the extension of the interphalangeal joints. The four palmar and four Dorsal Interossei muscles occupy the spaces between the metacarpal bones and are responsible of the respectively of the adduction and abduction movements of the long fingers.

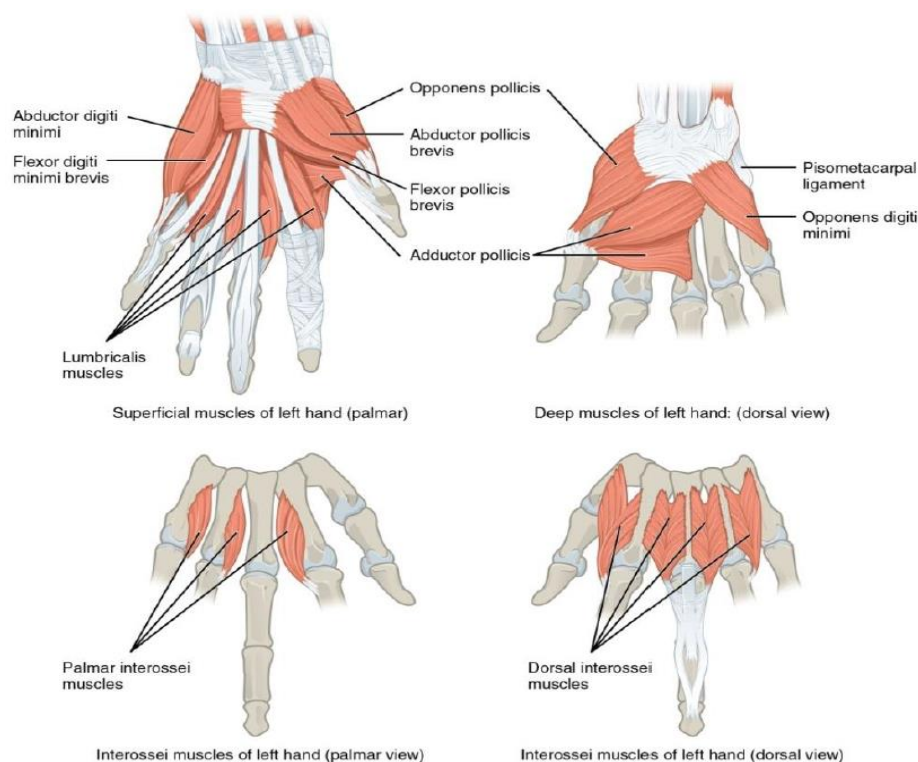


Figure 2.3. Intrinsic muscles of the human hand ([link](#)).

2.1.3 *Hand movements*

A wide number of movements, and consequently of tasks, can be executed by the human hand. Tools with disparate shapes can be managed; the various tasks are commonly classified according to the features of the involved object. This is fundamental when trying to simplify the high complexity of the hand motion, so as to facilitate the transition on artificial hands, such as robotic and prosthetic ones (Bullock, 2011).

It is possible to address two different types of hand operations: grasping and manipulation (Pons, 1999). Grasping is defined as a combination of procedures and operation with the aim to hold an object in static position with respect to the hand. On the contrary, manipulation can be regarded as a dynamic operation, requiring the coordinated motion of the fingers to manipulate an object within the hand (Pons, 1999).

Although manipulation and grasping problems are addressed separately, they are evidently characterized by common features related to physical and geometrical conditions. These somehow complicates to obtain a clear distinction between the two typologies of action. Sometimes the manipulation is regarded as a dynamic grasping and its study is collocated inside the grasping domain.

The grasp taxonomies have widely been studied in the literature. A satisfactory classification of human grasping has been proposed in (Cutkosky, 1989) (Figure 2.4). In it, two main classes of grasp are identified: Precision and Power grasps. These two classes and can be further investigated according to task and object shape.

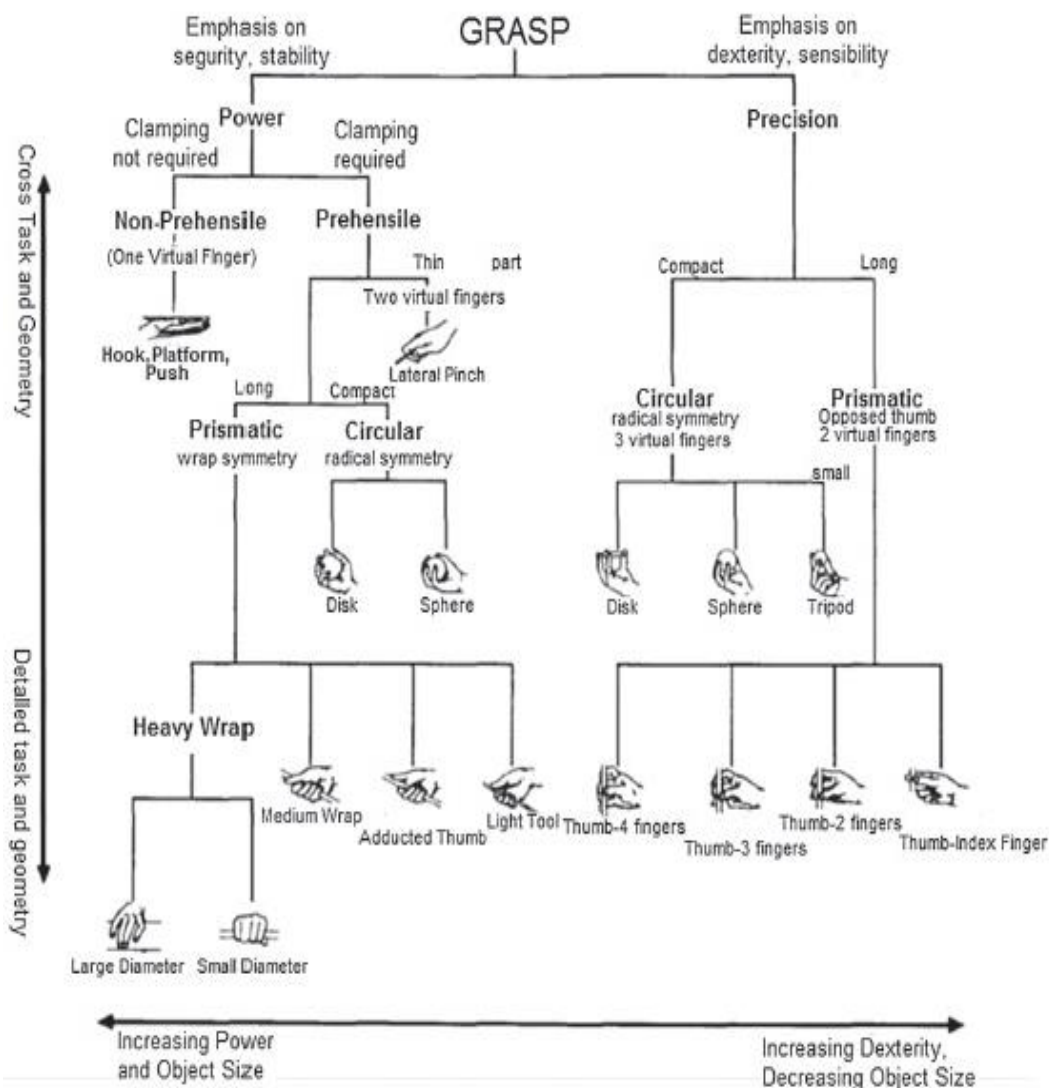


Figure 2.4 Hand grasping taxonomy (Cutkosky, 1989). © [1989] IEEE.

On the other hand, the human manipulation is more complex to classify due to the dynamic nature of the task and to the wide variety of object motion (Bullock, 2011). The human manipulation taxonomy presented in (Bullock, 2011) can be regarded as one of the most complete. It operates a classification based on the nature of the contact with the object and of the type of motion imparted by the hand. Such a taxonomy will not be shown here, as this thesis is more focused on grasping.

2.2 Tools for studying grasping forces: instrumented objects

2.2.1 Different approaches: background

As it can be observed in Figure 2.4, there are two typologies of grasps that are mainly considered for multi-fingered hands: power grasps, which make use of the whole surface of the hand to hold the object, and precision grasps, which use only the fingertips to the same end. In general, given an object and a biological or artificial hand, there is more than one of the possible grasps that fulfills the grasping requirements, both in terms of force and fingers position. Humans successfully grasp almost any kind of object in an intuitive way. A person might choose a particular grasp rather than another one relying on several criteria; these criteria take into account factors such as comfort, task type and object-specific characteristics, though the experience come to be the main guide.

One criterion that may contribute to the design and dimensioning of the artificial hands, especially prosthetic, is the study of contact forces during grasping. Different solutions have been proposed in the literature to acquire information about the forces involved in the grasping action. It is possible to distinguish between two principal approaches: the former is based on wearable devices while the latter is grounded on not-wearable devices. Sensorized gloves belong to the first category. The datagloves can measure forces (Hendrich, 2010), (Adnan, 2010) or contact events (Matsuo, 2008) by means of piezo-resistive force sensors or switches embedded into the glove. Notwithstanding, gloves of different dimension can be developed to address the different hand sizes, the glove wearability is often not perfect, thus implying a not perfect alignment between the hand joints and the glove sensors. This

drawback, together with the need of calibrating them for each subject and the fact that the glove makes movements less natural, have led to develop also different devices for grasp force evaluation. Other wearable solutions consist in the sensorization of the hand, either robotic or human, and the recording of the applied forces during grasping. In (Kargov, 2004), twenty FSR sensors have been located on predefined positions of human and prosthetic hands in order to evaluate grip force distribution over the different points. On the other hand, a hybrid of wearable and not-wearable solution is proposed in (Radwin, 1992). A strain gauge dynamometer has been used for estimating the resulting forces applied by the five hand fingers. The held object was the dynamometer itself, while piezo-resistive force sensors have been placed on the fingertips.

A variety of instrumented objects, i.e. objects commonly grasped in everyday life embedding tactile or force sensors, belong to the non-wearable solutions and have been adopted for studying grip force during pinch, tripod and power grasps. Different transduction technologies have been used in previous studies: force transducers (Flanagan, 1993; Johansson, 1994), strain gauges (Memberg, 1997; Keller, 2000), load cells (Memberg, 1995), tactile sensors (Koiva, 2011; Roa, 2012) for providing information about force values and spatial distribution of contact points, and six-axis force-torque sensors for determining the correct positioning of the fingers during tripod grasps (Flanagan, 1999), or for measuring the three components of the force applied during tripod grasp by human subjects (Baud-Bovy, 2001; Burstedt, 1999) or else for multi-touch detection as in (Serio, 2014). The main limitation of the object developed in (Serio, 2014) is that it does not allow recognizing the forces applied by each finger during the

contact. Furthermore, the use of six-axis F/T sensors implies very high costs.

2.2.2 The proposed approach: force sensors coupled with accelerometer

One of the purposes of this work has been to design, develop and test instrumented objects for grasp analysis. Such objects must be: (i) able to individually analyze the force applied by each finger during the task; (ii) capable of detecting slippage phenomena; (iii) based on low-cost technology, which can be easily applied to other types of objects for different grasps.

The choice of working with instrumented objects instead of wearable solutions allows avoiding all the problems related to the different anthropometries of robots and humans and all the aforementioned drawbacks of sensorized gloves. Additionally, the proper choice of the sensors to be embedded into the object also allows drastically reducing the costs of the technology, e.g. with respect to the solution proposed in (Serio, 2014), and developing a high number of objects to be used in multiple tasks. The objective of this work has been to create a set of daily life instrumented objects for force analysis during grasping in both human and robotic scenarios, possibly in addition to hand kinematic analysis (Cordella, 2012). The set of objects is conceived to be low-cost and simple enough to allow developing a wide number of objects to potentially study grasping and manipulation capabilities in several tasks. All the fabricated objects are thus endowed with small, low cost mono-axial force sensors for measuring the normal component of the applied force, and with an accelerometer for slippage detection during grasping. Force sensors embedded in the object have been statically

calibrated and validated through a compared analysis with a robotic hand featuring torque sensors.

As regards the use of accelerometers for slip detection, one must note that it dates back to the end of 80s. In (Howe, 1989; Tremblay, 1992), a slip sensor has been obtained placing an accelerometer on a rubber skin, which covered a plastic foam layer. Later, an additional accelerometer has been mounted in the sensor structure (Tremblay, 1993) to discriminate between vibration caused by the sensor itself and actual slippage. In (Rodriguez-Cheu, 2006), an accelerometer has been jointly used with a piezoelectric sensor. Slippage is recognized when both sensors overcome a certain threshold. In (Abhinav, 2009) an accelerometer has been used to verify the reliability of a pressure sensor to estimate slippage. However, the cited works do not report a systematic analysis of the use of the accelerometer to detect slippage. Furthermore, after an exhaustive investigation of the literature, it can be affirmed that there are not previous examples of instrumented objects executing slip analysis through accelerometers. In this work an ad hoc experimental setup for slip analysis has been developed: spectral analysis of accelerometer outputs has been performed to evaluate the sensor behavior when the object is slid thanks to a linear actuator upon surfaces with different *a priori* known roughness values. Afterwards, the instrumented object has been preliminary tested during tripod grasping tasks performed by one human subject.

2.3 Set of instrumented objects: features

In order to study prehension forces in humans, three instrumented objects have been designed. Bipod and tripod grasps have been initially selected, being one of the more commonly used ADLs (Cloutier, 2013). In more detail, the objects have been assigned to the following tasks:

- Bipod grasp (both human and robotic hands)
- Tripod grasp (human hand)
- Tripod grasp (robotic hands)

The objects have a spherical shape, with a diameter of 5.9 cm, similar to a tennis ball. The location of the contact areas (1.8x2.2 cm) has been chosen according to (Flanagan, 1993). The force sensors mounted on the contact areas boasted a continuous force resolution and a measurement range of [0.2, 20] N.

2.3.1. Design of the objects

Inside the objects, a cavity (60 mm diameter for the tripod grasp objects, 45 mm for the bipod grasp one) hosts the electronic board (printed circuit board, PCB). *Ad hoc* extrusions have been cut in the object inner walls to stick the board. The sensors have been directly connected to the board through *ad hoc* holes created within the object. A 2.5 cm diameter hole has been designed to connect the board to an external DC power supply. The total weight of the instrumented objects was around 60 g for the tripod grasp ones, and around 90 g for the remaining one; this is due to the thicker shell, as the inner cavity diameter is smaller for the bipod grasp object. Each contact area is composed of a quadrangular cavity, with the sensor put in the middle, and a movable part with a cylindrical probe which allows conveying the applied normal force onto the sensitive part of the sensor. Figure 2.5 gives some graphical details.

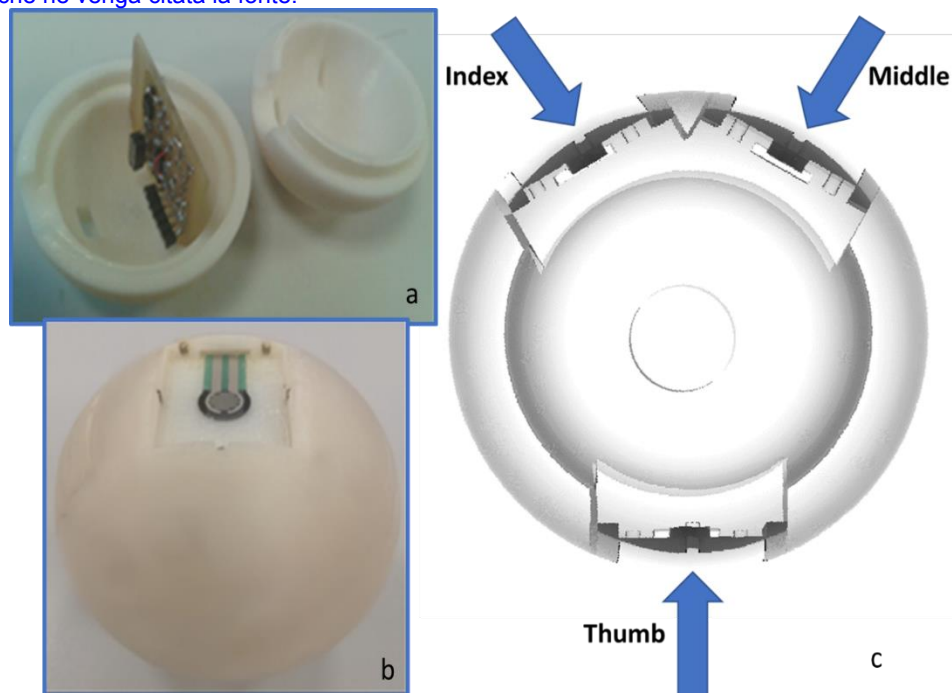


Figure 2.5. Detail of the PCB placed in the object (a); FSR sensor fixed in its quadrangular cavity (b); CAD of the instrumented object (c).

Two objects have been designed for the tripod grasp: one for the human hand, the other one for robotic hands. The difference between the two objects resides in the position of the sensorized of index and middle fingers. In fact, the object for the human hand has the two mentioned areas inclined at an angle of 30° with respect to the normal direction, whereas the object for robotic hands the same angle is 24° . This position difference has been necessary for the following reason: robotic hands like IH2, Michelangelo, Bebionic and iLimb do not feature the abduction degree of freedom at the MCP joints. It has been observed that during a tripod grasp using small ball, the closure positions of index and middle fingers for the aforementioned hands is very close. Instead, for the human tripod grasp, it has been preferred to keep their positions more distant; this is more comfortable for the human grasp, which is clearly more natural. Figure 2.6 illustrates the configurations of the various objects.

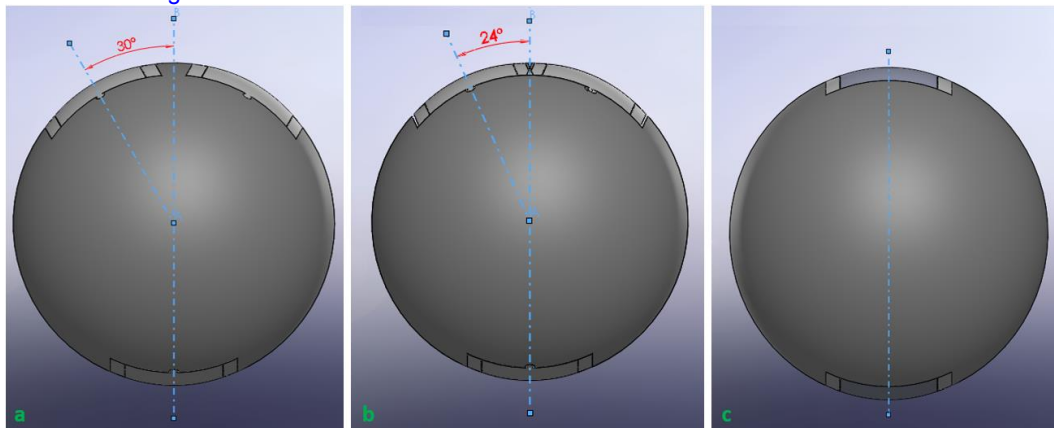


Figure 2.6. Configuration for every object. Tripod grasp object, human hand (a); tripod grasp object, robotic hands (b); bipod grasp object (c).

Very small mechanical springs (mean coil diameter: 1 mm) have been mounted in five rails at the sides of each hole (Figure 2.7), in order to restore the equilibrium position of the moveable parts. The gap between the cylindrical probe and the fixed part of the contact area is equal to the thickness of the sensor (i.e., 0.35 mm). A high stiffness value has been chosen for the springs, i.e., 4.09 N/mm; this choice is motivated by the necessity of avoiding phenomena of pre-loading when the object is not being held.

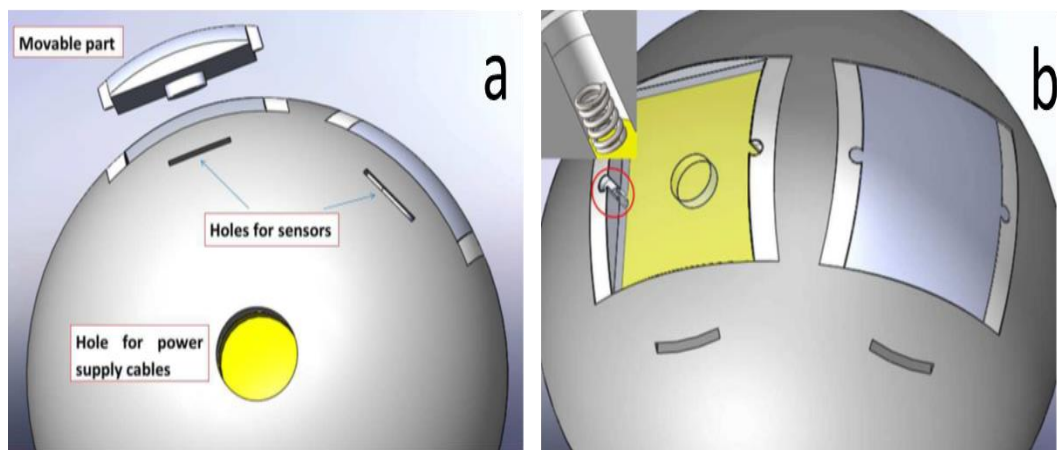


Figure 2.7. The movable part with the cylindrical probe, the hole for connecting the electronic board to the external power supply and supplementary holes for eventually connecting the sensors to an external board (a); the mechanical springs mounted in the rails (b).

2.3.2 Tactile sensing: sensing element and electrical design

Forces applied to the movable part of the contact areas have been recorded by Force Sensing Resistor sensors ([FSR, Model 400](#) by Interlink Electronics, Inc.) mounted on the fixed part, immediately below the cylindrical probe of the movable part. Each sensor has a circular active area, with a diameter of 5.08 mm, a discrimination threshold of 0.2 N and a measurement range up to 20 N. Their working principle is based on the piezo-resistivity, i.e., the electrical resistance of such a sensor varies as a force is applied onto it. Therefore, the force generates a variation of the electrical resistance (R_{FSR}): the highest is the force, the lowest is the resistance. The input-output relationship is almost linear in double logarithmic coordinates over the force range [0.2, 20] N, as reported in the sensor datasheet and in Figure 2.8. Thus, the relationship between the R_{FSR} and the Force F can be expressed as:

$$R_{FSR} = 10^{a \cdot \log_{10}(F) + b} \quad (2.1)$$

where a and b are constants that depend on the sensor response. Resistance value R_{FSR} has been transduced into voltage through a Wheatstone bridge with three nominally identical resistances R_w (equal to 2.2k), as shown in the schematics of the analog conditioning circuit (Figure 2.9).

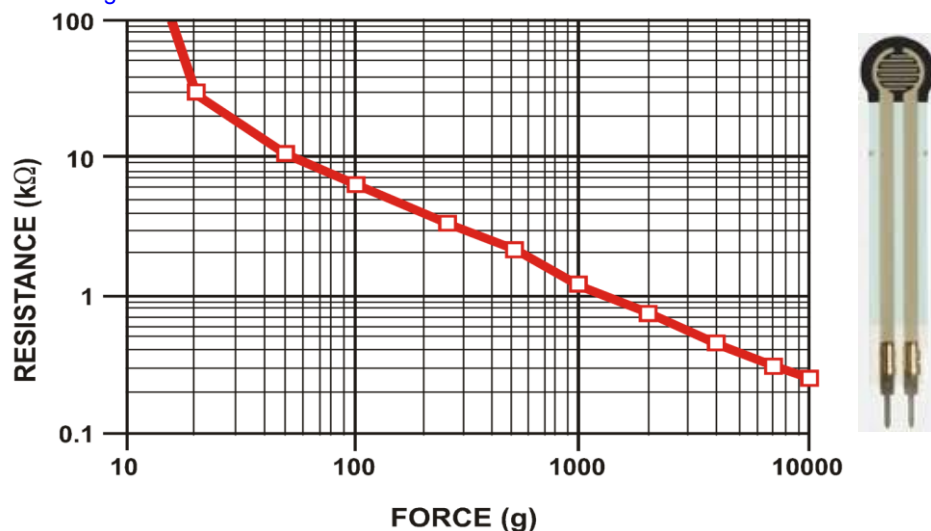


Figure 2.8. Characteristic output of a FSR400 sensor (on the right) in logarithmic diagram.

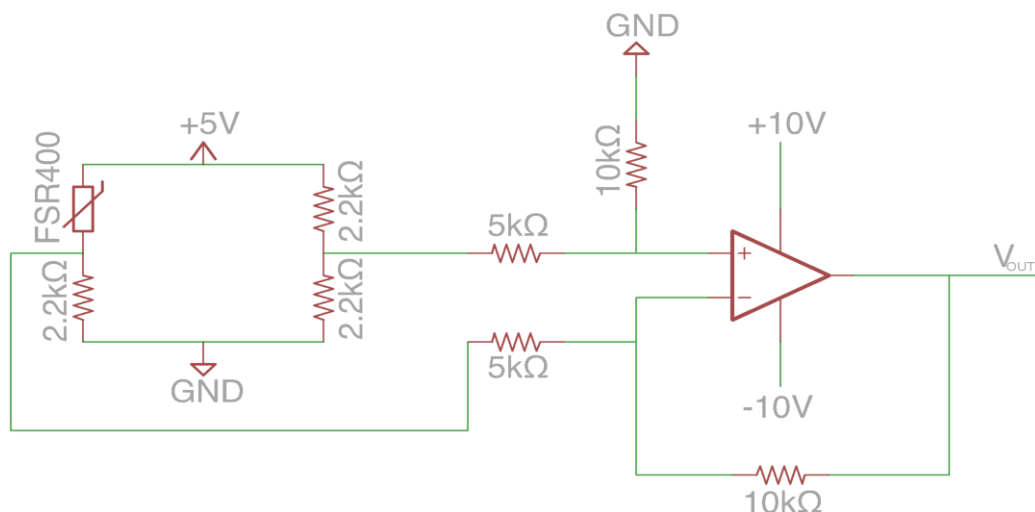


Figure 2.9. The schematics of the analog conditioning circuit, which transduces a resistance variation into a voltage variation.

The voltage output (V_{out}) of the measurement chain has been obtained by amplifying the Wheatstone bridge output through an operational amplifier (TL074 by Texas Instrument, Inc.) set in differential configuration, with a nominal gain of 2.

By taking into account Equation (2.1), the input-output relationship of the Wheatstone bridge, and the amplification stage, the voltage output can be expressed as

$$V_{out} = \frac{c}{R_w + 10^{a \cdot \log_{10}(F) + b}} - d \quad (2)$$

where a and b are the same as in (2.1), while c and d are constants that depend on the actual gain of the amplification stage. All the four constants can be estimated e.g. by means of the *Curve Fitting Tool* available with the software Matlab. Figure 2.10 plots the theoretical trend of V_{out} as a function of the applied force, considering a gain of 2 for the circuit shown in Figure 2.9 and different values of the Wheatstone bridge resistances: the choice of and $R_w = 2.2k$ allows obtaining a good tradeoff between sensitivity at low force and resolution at high force in the whole range of interest (i.e., up to 10 N). In fact, observing the logarithmic threads depicted in Figure 2.10, it is easy to notice that a value below 2.2k leads to a too low resolution, being the variation of V_{out} really low if compared to the force variation. For instance, assuming $R_w = 1k$, in the range 4-6 N, or 6-8 N as well, the voltage variation is lower than 1 V. This might conduct to insufficiently accurate force measurements. Likewise, choosing too high values for R_w (e.g. 30k) leads to really high sensitivity at low forces, but on the other hand it implies the loss of resolution as the force value overcomes 3 N.

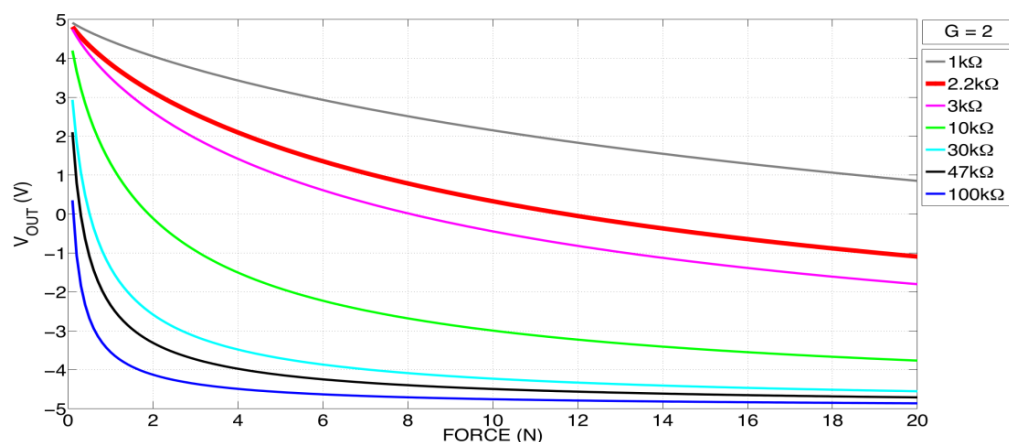


Figure 2.10. Theoretical curve of V_{out} as a function of force F , for different values of R_w .

The electronic circuit has been designed to be fully embedded within the instrumented objects, in order to perform the analog preconditioning of the signal as close as possible to the sensor unit. To this purpose, components with small SMD (surface-mount device) layout have been chosen for the resistances and capacitors (0603 package) and for the operational amplifier (SOIC14 package). The first version of the PCB, structured in two layers, has been designed using the Eagle CAD software, fabricated through chemical etching and wedged in the object (Figure 2.5a). Latest versions have been fabricated by an external company (OSH Park), specialized for this task.

2.3.3. Static Calibration

The FSR sensors mounted in the instrumented objects have been statically characterized in order to extract the logarithmic relation between voltage and force. The best fitting calibration curves in the range 0.2-8 N, according to mathematical model represented by (2.1) and (2.2), are shown in Figure 2.11 for the tripod grasp object (human hand).

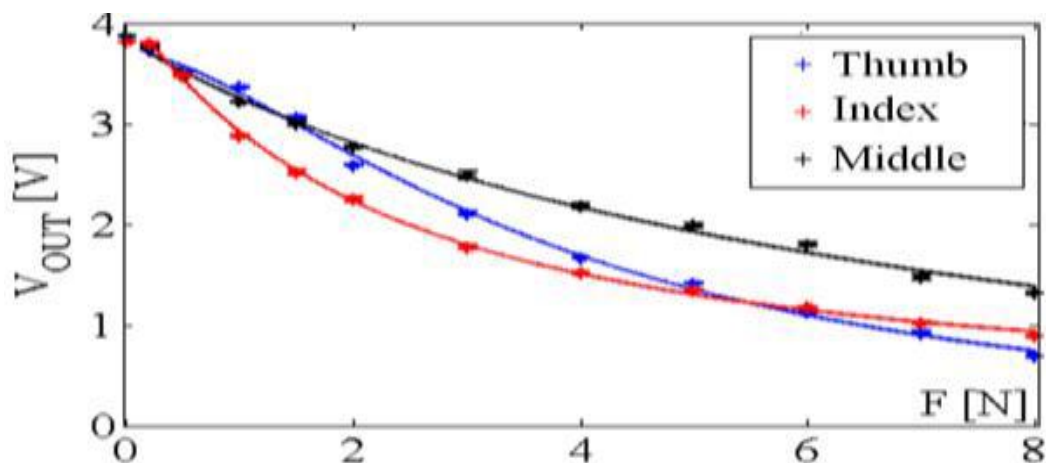


Figure 2.11. Best fit curves for the FSR sensors for the tripod grasp (human hand) instrumented object (Romeo, 2015). © [2015] IEEE.

A mechanical testing system (series 5900, Instron) has been used to apply controlled compression load to the three sensors. This system

(Figure 2.12) has been equipped with a load cell (range of measurement up to 10 N) that measures and records the applied force with a sample frequency of 100 Hz. A probe, designed with SolidWorks and built by a rapid prototyping printer (Project 3000 by 3D Printer Inc.), allowed applying the force on a circular surface (diameter of 5 mm) which might be considered equal to the active area of the sensors. A digital oscilloscope (1540, Yokogawa) has been used for the visualization of all the sensor outputs (V_{out}).

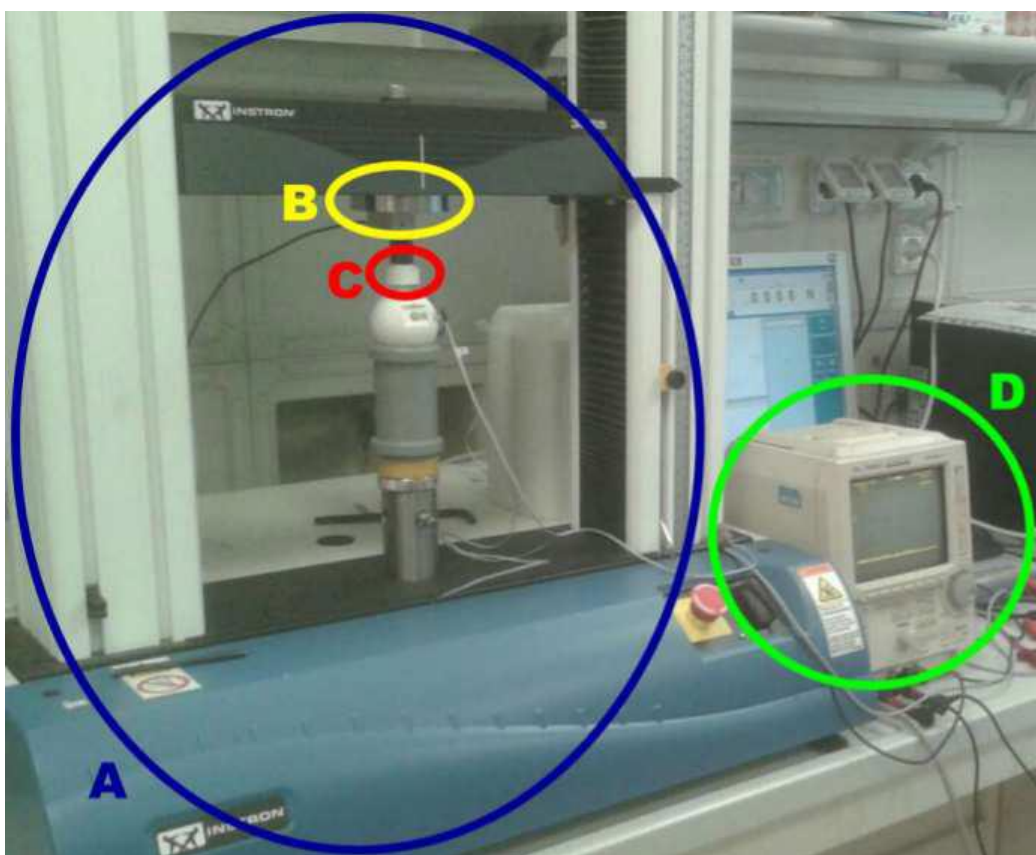


Figure 2.12. Experimental setup for the FSRs static calibration. Mechanical testing system a); load cell b); probe c); digital oscilloscope d).

Experimental data have shown a good agreement with the non-linear theoretical model described by (2.1) and (2.2) as confirmed by the high coefficient of determination R^2 and the low root-mean-square error RMSE. Table 2.2.1 reports the results of the calibration for all the three instrumented objects. It is worth mentioning that the described process,

though it can be generally indicated as a static calibration, is more properly a *quasi-static* calibration; in fact, during the calibration trial the probe actually moves, even if its velocity is rather low (below 1 mm/s).

Table 2.2.1. Results of static calibration of all the instrumented objects.

Object	Sensor	a	b	c	d	R ²	RMSE (V)	S _{mean} (VN ⁻¹)
Tripod grasp (human hand)	Thumb	-1.585	4.267	-8542	-3.722	0.9979	0.0648	-0.37
	Index	-0.962	4.211	-10760	-3.834	0.9965	0.064	-0.32
	Middle	-1.093	3.725	-8591	-4.077	0.999	0.038	-0.4
Tripod grasp (robotic hands)	Thumb	1.591	2.5	8155	-0.242	0.9992	0.0415	-0.37
	Index	1.539	1.538	14110	2.502	0.9992	0.0174	-0.17
	Middle	1.528	2.846	4258	-1.941	0.9937	0.0693	-0.23
Bipod grasp	Thumb	1.343	1.692	14250	2.566	0.9964	0.0474	-0.22
	Index	-2.691	4.917	-5426	-3.901	0.9991	0.0335	-0.27

Moreover, hysteresis, which is a well-known issue regarding the piezo-resistive force sensors, has also been analyzed. Three repeated cycles of load and unload have been carried out for each sensor; hysteresis has been calculated considering the maximum difference of V_{out} at the same F value, as a percentage of full-scale output range (Figliola, 2015). Hysteresis values ranged from a minimum of 2.3% (for the index sensor) to a maximum of 11.5% (for middle sensor), confirming the

manufacturer specifications. Figure 2.13 reports the results for the thumb sensor.

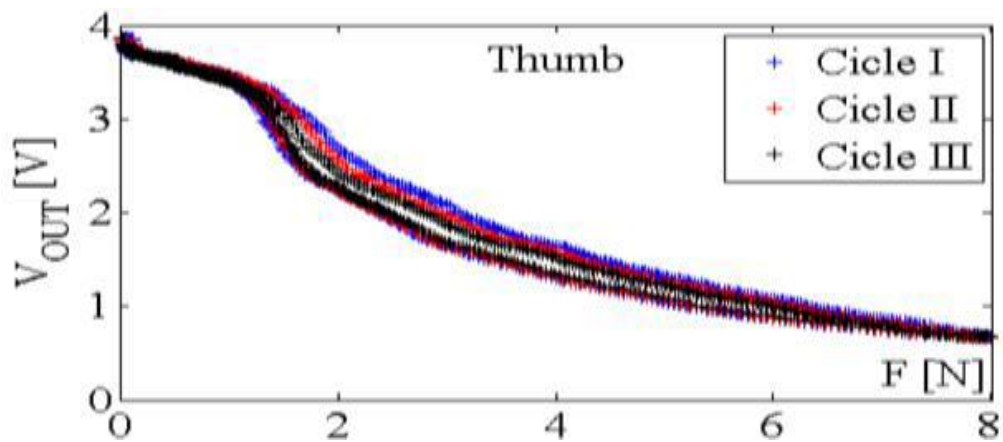


Figure 2.13. Sequential tests for assessment of the hysteresis error (thumb, tripod human grasp object) (Romeo, 2015). © [2015] IEEE.

This analysis has been performed only for the tripod grasp object (human hand), with the intent of evaluating the performance of the sensors in the first object prototype. Based on the obtained results, it has been assumed that the FSRs performance, in terms of hysteresis, is acceptable and that the same analysis is not mandatory for the future prototypes.

2.3.4 Slip detection: sensing element and electrical design

The electronic board also included a tri-axial accelerometer (ADXL330 by Analog Devices, Inc.) and a dedicated voltage regulator (MCP1700, Microchip Technology, Inc.). First order RC low-pass filters have been built on the PCB in order to reduce the band. The accelerometer bandwidth can extend up to 1600 Hz, but to reduce aliasing errors it has been limited to 500 Hz. A resistor R is embedded inside the accelerometer package (32k); thus, for achieving a [0-500] Hz bandwidth, a 10n capacitor has been placed between each accelerometer output and the PCB ground. Schematic design of the accelerometer connections is provided in Figure 2.14.

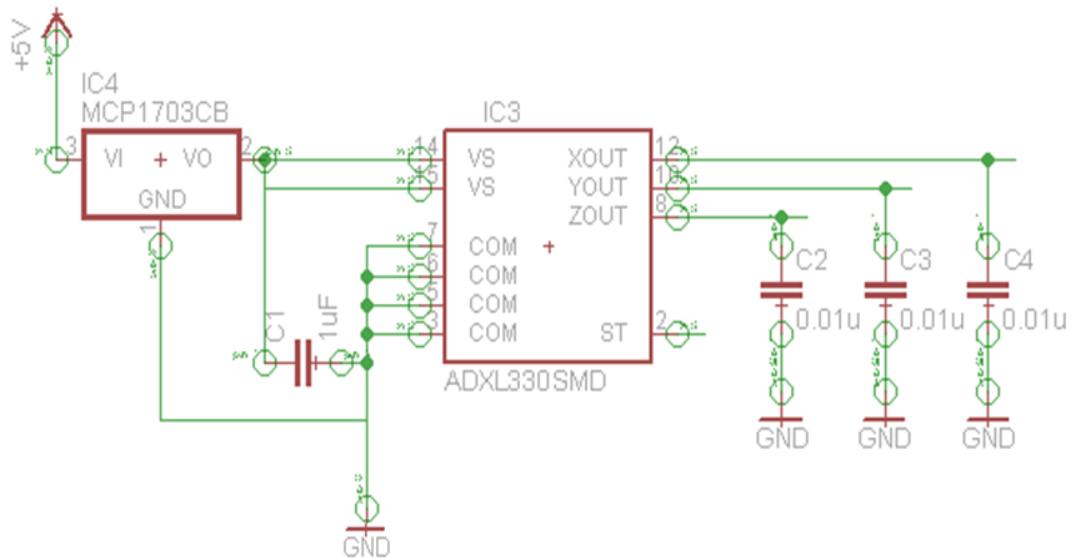


Figure 2.14. Accelerometer pin-out and connections.

The accelerometer had a twofold function, acting as:

- Slip detection sensor
- Inclinometer

The second of the two functions will be described in the next Subsection. Regarding the first one, it has been achieved through the application of an algorithm which works in the frequency domain. It is well known, indeed, how an acceleration sensor is able to detect vibrations when rubbed upon a surface. The highest is the surface roughness, the highest will be the vibrations amplitude, with a frequency content that may vary from a surface to the other. Thus, the vibrations can be associated to the slip event; this can lead to the identification of the slip events, provided that false positives are correctly avoided.

To this end, an algorithm operating in the frequency domain, namely *Welch's Method*, has been applied to the accelerometer output. The Welch's Method serves as a tool for the estimation of the power of a generic signal at different frequencies. Though this method is based on the concept *periodogram*, it represents a considerable improvement

on the standard periodogram spectrum estimating method. In the same way, it overcomes the Bartlett's method, in that it significantly reduces noise in the estimated power spectra. A conceptual explanation of the method working principle applied to a generic signal $x[k]$ is summarized below:

1. Signal $x[k]$ is divided into N segments $x_m(t)$ that have the same length n ($m=1, 2 \dots N$; $t=1, 2 \dots n$). Each segment $x_m(t)$ overlaps the adjacent one $x_{m+1}(t)$ of a pre-established number of samples (in this case, 50% of the segment);
2. The overlapping segments are then windowed: a given window is applied to the individual N data segments;
3. The Discrete Fourier Transform (DFT) is computed for each windowed segment and, subsequently, the squared modulus is computed.
4. The sum of the moduli of all the DFTs segments is finally averaged by dividing by N .

For each segment $x_m(t)$, windowed DFT, named $d_m(\omega_j)$, can be expressed as:

$$d_m(\omega_j) = \frac{1}{\sqrt{n}} \sum_{t=1}^n w(t) \cdot x_m(t) e^{-2\pi i \omega_j t}, \quad (2.3)$$

where $\omega_j = 0, \frac{1}{n}, \dots, \frac{n-1}{n}$, and $w(t)$ is the chosen window (in this case, Hamming window). The squared modulus $P_m(\omega_j)$ for all the $d_m(\omega_j)$ is given by

$$P_m(\omega_j) = \frac{1}{\sum_{t=1}^n w^2(t)} |d_m(\omega_j)|^2. \quad (2.4)$$

At this point, all the segments moduli are summed and averaged on N . The final result, which is used for the slippage detection, has the following form:

$$\widehat{S}_{xx}(\omega_j) = \frac{1}{N} \sum_{m=1}^N P_m(\omega_j). \quad (2.5)$$

Therefore, the algorithm output is an array of power measurements, one per every *bin* ω_j . The computation of $\widehat{S}_{xx}(\omega_j)$ allows reducing the variance in the computation of the several $P_m(\omega_j)$, which is high due to their statistical oscillations. As a consequence, the noise is drastically reduced with respect to classical Power Spectrum Density (PSD) estimation.

The main advantage of this approach, compared to the classical techniques such as Fast Fourier Transform (FFT), is the drastic reduction of noise. This comes to be highly useful when noisy peaks might have a comparable amplitude to the meaningful peaks. An example of the algorithm application to a non-deterministic signal is illustrated in Figure 2.15. The signal has been obtained by manually rubbing an FSR force sensor onto a ridged surface, whose pace Δp (i.e., the spatial distance between 2 consecutive ridges) was 1 mm. The fundamental frequency of the signal should be:

$$f_{fund} = \frac{v(t)}{\Delta p} \quad (2.6)$$

where $v(t)$ is the velocity of the sliding movement upon the ridged surface. When the sensor is moved manually, the velocity is not a priori known, and cannot be considered to be constant. On the contrary, Equation 2.6 can be assumed as valid when the sensor is moved automatically, like in (Oddo, 2011a). Thus, it is more appropriate to expect a range of frequencies Δf rather than a single, fundamental frequency f_{fund} .

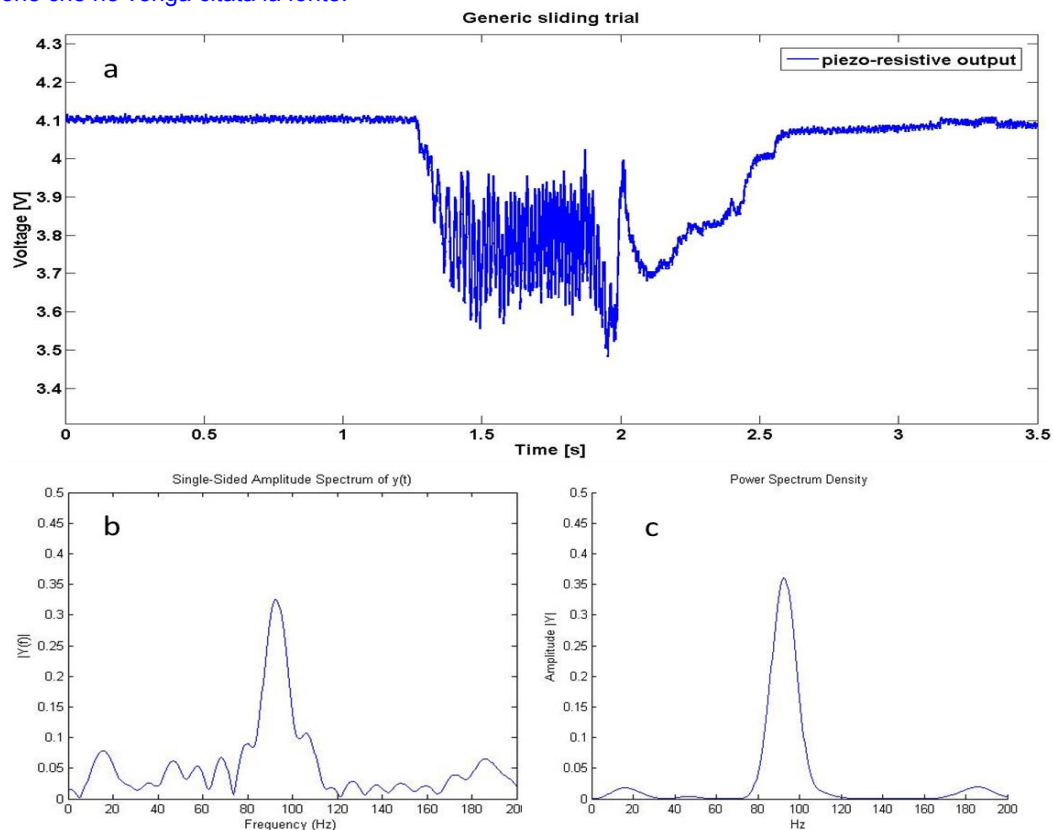


Figure 2.15. The original FSR signal during a generic sliding trial (a); spectrum estimation through the FFT (b); spectrum estimation through Welch's Method (c).

From Figure 2.15c one can observe the almost total absence of noise, particularly outside the meaningful spectrum region, which is located in the range $\Delta f = [80 - 105] \text{ Hz}$. The Δp value suggests that the rubbing velocity has been $[8-10.5] \text{ cm/s}$.

In the same way, by applying the algorithm to the accelerometer output, the obtained power density spectrum appears with low noise and reflects the frequencies contained in the slip signal portion. Again, the original time signal is non-deterministic: the object incorporating the PCB with the accelerometer has been rubbed manually onto the same surface as in the previous case. Figure 2.16 shows the original tri-axial output of the accelerometer, and the PSD computed on the x-axis. This axis was the one directed towards the gravity direction during the trial, and thus its signal was the one with the highest amplitude. Similar result

would be achieved on the other two axes, but for sake of brevity only the one with the main amplitude has been reported.

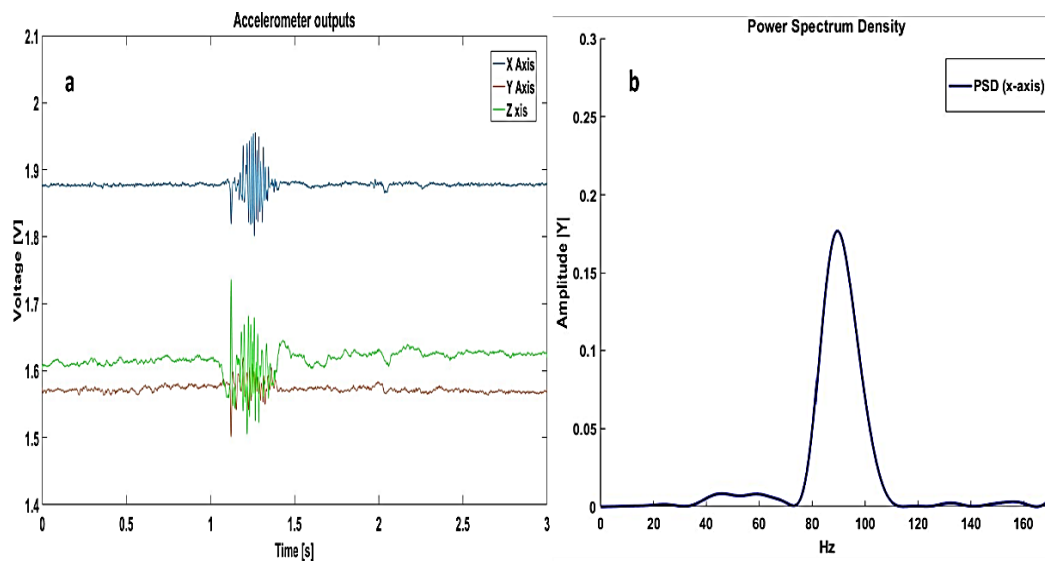


Figure 2.16. Tri-axial output of the accelerometer during a generic sliding trial (a); PSD of the x-axis voltage (b).

2.3.5 Accelerometer as an inclinometer

The tri-axial output of the accelerometer has also been employed to estimate the orientation angles during quasi-static grasping tasks. Indeed, accelerometers are not only sensitive to linear acceleration \bar{a} , but to the local gravitational field as well. That is, they sense the acceleration $\overline{(g - a)}$, rather than the mere \bar{a} . Thanks to this capability, they provide information on the orientation angles (i.e., *pitch* and *roll*) allowing a smartphone or tablet display to automatically switch between portrait and landscape settings. The same applies to the instrumented objects described in this document; the PCBs wedged inside the objects host an accelerometer, placed as shown in Figure 2.17. Pitch and roll angles can be determined starting from the accelerometer output voltages when it is hold statically, so that the condition $a \ll g$ is true.

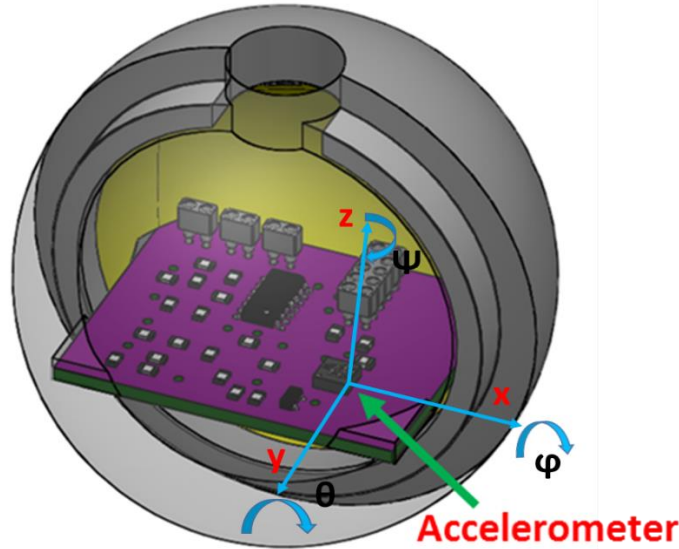


Figure 2.17: CAD detail of the accelerometer position and reference frame inside the instrumented object (Romeo, 2017a). © [2017] IEEE.

The mathematical relationship which relates the voltage output V_a of the accelerometer to the overall acceleration vector $\overline{(g - a)}$ has the following form:

$$V_a = S \cdot R_1 \cdot \overline{(g - a)} + \overline{O_a}. \quad (2.7)$$

Equation (2.7) can be more accurately expressed in matrix form:

$$\begin{bmatrix} V_{ax} \\ V_{ay} \\ V_{az} \end{bmatrix} = \begin{bmatrix} S_x & 0 & 0 \\ 0 & S_y & 0 \\ 0 & 0 & S_z \end{bmatrix} \cdot \begin{bmatrix} G_x \\ G_y \\ G_z \end{bmatrix} + \begin{bmatrix} O_{ax} \\ O_{ay} \\ O_{az} \end{bmatrix}, \quad (2.8)$$

where S_x, S_y, S_z (Vs^2/m) are the sensitivities of the accelerometer axes, O_{ax}, O_{ay}, O_{az} (V) are the axes offsets and

$$\bar{G} = \begin{bmatrix} G_x \\ G_y \\ G_z \end{bmatrix} = R_1 \cdot \bar{g} = R_{xyz} \cdot \bar{g}. \quad (2.9)$$

In (2.9), R_{xyz} is the rotation matrix relative to the earth's coordinate frame, whereas $\bar{g} = [0 \ 0 \ 1]$ is the normalized gravity vector. Moreover, it is assumed that $a \ll g$; consequently, the sensitivities S_x, S_y and S_z and the offsets O_x, O_y and O_z are easily calculable for each

accelerometer axis. This is the result of the accelerometer calibration: by imposing some pre-fixed rotations in order to determine R_{xyz} , the $[G_x G_y G_z]^T$ components can be computed and hence, the sensitivities and the offsets. Calibration values for all the instrumented objects are reported in Table 2.2: they do fully respect the accelerometer specifications. Another calibration technique (Campolo, 2006) has been implemented; though, results have been almost identical to the ones obtained by means of the procedure illustrated above.

Table 2.2. Results of the calibration of all the fabricated instrumented objects (*the accelerometer has been supplied with 1.8 V rather than 3.6, leading thus to half lower values).

Object	S_x $(\frac{Vs^2}{m})$	S_y $(\frac{Vs^2}{m})$	S_z $(\frac{Vs^2}{m})$	O_x (V)	O_y (V)	O_z (V)
Tripod grasp object (human hand)	0.284	0.283	0.280	1.585	1.626	1.598
Tripod grasp object* (robotic hands)	0.175	0.174	0.181	0.890	0.887	0.958
Bipod grasp object	0.349	0.348	0.343	1.668	1.676	1.692

The pre-fixed rotations used for the accelerometers calibration have been the following:

- Around x-axis
 - $\varphi = 0$
 - $\varphi = -\pi$
- Around y-axis
 - $\vartheta = \frac{\pi}{2}$

- $\vartheta = -\frac{\pi}{2}$
- Around x-axis
 - $\varphi = -\frac{\pi}{2}$
 - $\varphi = \frac{\pi}{2}$

Once the sensitivities and offsets are known, starting from Equation (2.9) every couple of roll and pitch angles can be calculated. If three rotations following the order X-Y-Z are made, one has:

$$\begin{bmatrix} G_x \\ G_y \\ G_z \end{bmatrix} = R_{xyz} \cdot \bar{g} = \begin{bmatrix} -\sin(\theta) \\ \cos(\theta) \sin(\varphi) \\ \cos(\theta) \cos(\varphi) \end{bmatrix} \quad (2.10)$$

$$\varphi = \tan^{-1}\left(\frac{G_y}{G_z}\right), \quad (2.11)$$

$$\theta = \tan^{-1}\left(\frac{-G_x}{\sqrt{G_y^2 + G_z^2}}\right), \quad (2.12)$$

Looking at (2.10), the singularities of the X-Y-Z configuration can be determined, i.e. $\vartheta = \pm \frac{\pi}{2}$. To correctly estimate the orientation angles, such conditions must be avoided; otherwise, one of the two degrees of freedom will be lost, as φ will be undetermined according to (2.10) and (2.11). Orientation angles can be alternatively estimated modifying the order of the three rotations, such as the rotation about Y-axis is imagined to be performed first. In this way, the Y-X-Z configuration gives:

$$\begin{bmatrix} G_x \\ G_y \\ G_z \end{bmatrix} = R_{yxz} \cdot \bar{g} = \begin{bmatrix} -\sin(\theta) \cos(\varphi) \\ \sin(\varphi) \\ \cos(\theta) \cos(\varphi) \end{bmatrix} \quad (2.13)$$

$$\theta = \tan^{-1}\left(\frac{-G_x}{G_z}\right), \quad (2.14)$$

$$\varphi = \tan^{-1}\left(\frac{G_y}{\sqrt{G_x^2 + G_z^2}}\right), \quad (2.15)$$

In this case, singularity occurs for $\varphi = \pm \frac{\pi}{2}$. Evidently, each representation has its own singularities. By using a different rotation order from the two ones shown above, undetermined systems would be obtained. This because the G vector would include terms with the yaw angle ψ , leading to mathematically unsolvable configurations. In this regard, it is worth noticing that the yaw angle cannot be estimated through the sole use of an accelerometer, neither if more accelerometers are employed. Indeed, Equation (2.10) and (2.13) are the same even if only two rotations (X-Y or Y-X) are made: that is, the rotation about Z-axis is redundant. This implies the impossibility to determine the rotation (yaw) about such an axis: accelerometers are insensitive to rotation about the earth's gravitational field vector.

2.4 Experimental validation and results

Before proceeding with the usage of the instrumented objects, several tests have been carried out with the aim of demonstrating the validity of their performances (Romeo, 2015). In this section, experiments done with the human hand tripod grasp object, and the relevant set-ups will be illustrated. Three experimental sessions have been executed, with the following order: (i) validation of FSRs force measurements by means of a sensorized robotic hand; (ii) investigation on the object capability to detect slippage; (iii) grasp analysis with a human subject.

In every described trial, sensor outputs have been acquired through a DAQ board (NI-6009) at a sampling rate of 2000 Hz.

2.4.1 Force measurement: comparison with ground truth

The initial experiments have been done for ensuring that the force levels measured by the force sensors embedded in objects are reliable. An external, objective mean of comparison was needed for this task; a

comparative analysis with the force values measured by a robotic hand, i.e. DLR/HIT Hand II (Liu, 2008) has been performed. Each finger of the robotic hand has three torque sensors and three Hall-effect sensors for measuring joint positions. By means of the hand Jacobian and the measured torques τ^T , the forces applied by the hand tips have been computed as follows:

$$F_{TIP}^{tip} = R_{mcp}^{tip} J_P^{-1} \tau^T = R_{mcp}^{tip} F_{TIP}^{MCP} \quad (2.16)$$

where R_{mcp}^{tip} is the rotation matrix of the MCP joint reference frame with respect to the fingertip reference frame, J_P^{-1} is the Jacobian matrix related to linear velocity, F_{TIP}^{MCP} is the force applied by the fingertip with respect to the MCP joint reference frame and F_{TIP}^{tip} is the fingertip force expressed in the fingertip reference frame.

Figure 2.18 depicts the set-up including the robotic hand and the object. The instrumented object has been located on a support and the normal force applied by the middle finger of the robotic hand on one sensorized area of the object surface has been simultaneously measured by the FSR sensor in the object and the torque sensors in the hand. Eight repetitions of the task have been performed. Force mean value extracted from the torque sensors through Equation (2.10) was equal to 3.3584 N (± 0.1404), whereas the corresponding force mean value recorded by FSRs was 3.3495 N (± 0.1523).

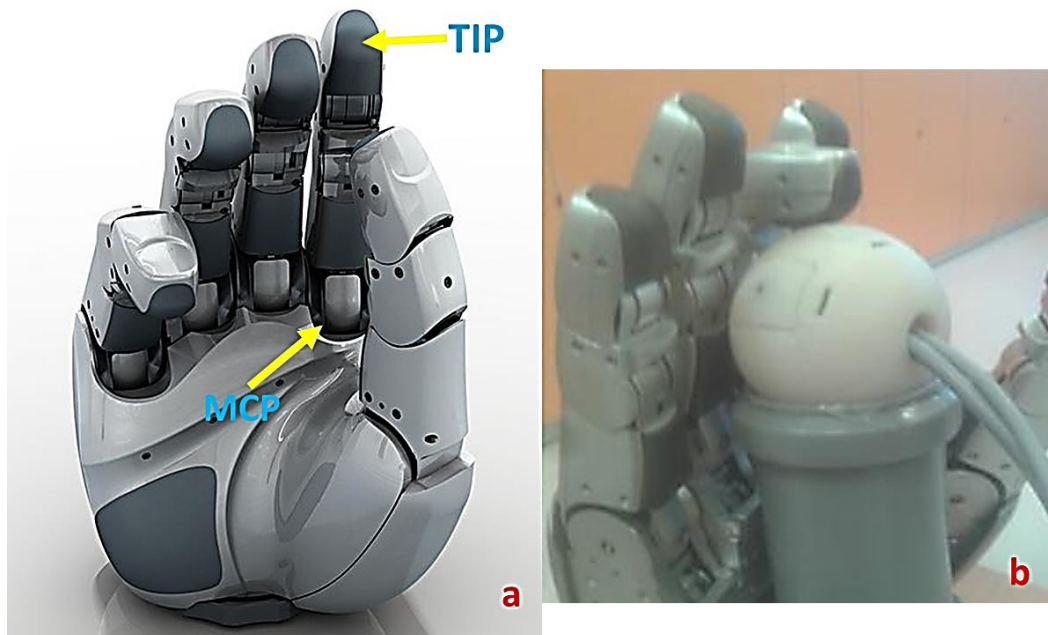


Figure 2.18. Robotic hand with the detail of the involved joints (a); the experimental set-up, with the support for the object and the robotic hand pressing one of the object sensorized areas (b).

Given the surprisingly closeness of the found values, it has been possible to conclude that the forces acquired with the instrumented object were reliably comparable to those measured by the torque sensors embedded in the robotic hand.

2.4.2 Slip detection: validation through automated set-up

A specific experimental setup has been arranged to rigorously analyze slippage detection by means of the accelerometer embedded in the object. It consisted of a linear actuator, which translated the object onto some selected surfaces at a fixed velocity, so as to avoid the inconvenience described in Subsection 2.4.4. Three metallic surfaces with given roughness, i.e. $0.2 \mu\text{m}$, $0.8 \mu\text{m}$ and $3.2 \mu\text{m}$, have been employed for the sliding tests. Such roughness values have been chosen to replicate the roughness of tools and objects that one person can daily meet, which are even coarser. The actuator (M-235.2DD by PI, Inc.) was position controlled by means of a PID servo control and an

incremental encoder with 11-bit resolution and incremental resolution of $0.5 \mu\text{m}$.

Again, the validation procedure has been applied to the first developed prototype, and then extended to the remaining ones. The object has been constrained to the actuator shaft through a gripper purposely designed (through SolidWorks) and realized, which made the object travel for 1 cm upon the test surfaces. The tests have been performed at three different velocities (15 cm/s, 25 cm/s, 35 cm/s), with corresponding accelerations of 30 cm/s^2 , 40 cm/s^2 and 50 cm/s^2 . In each trial, the object was fixed to the gripper so that the x-axis of the accelerometer was oriented towards the gravity direction, thus yielding the response with the greatest amplitude. Figure 2.19 shows the automated set-up, with details about the instrumented object coordinate frame.

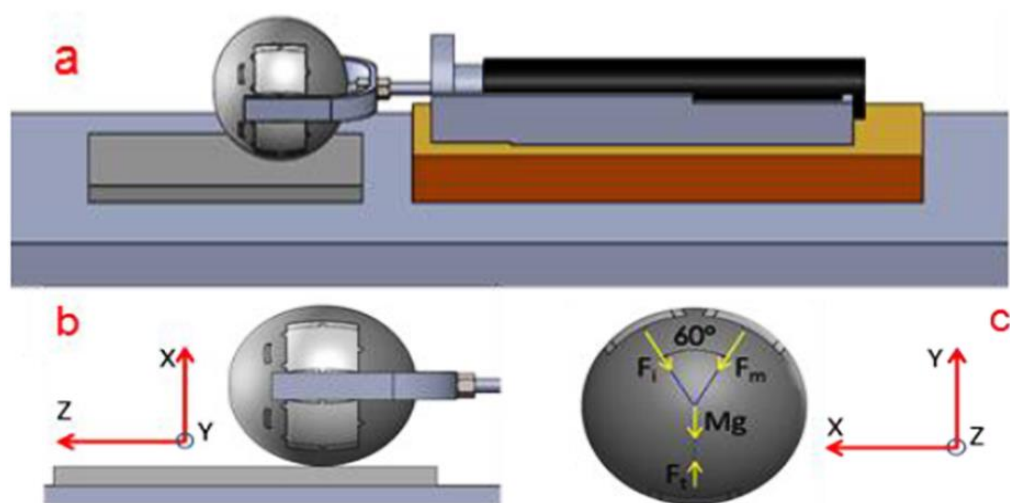


Figure 2.19. Slip set-up with test surface and linear actuator (a); accelerometer axes during the slip tests (b); accelerometer axes and forces scheme during the human grasp trial without slip (c) (Romeo, 2015). © [2015] IEEE.

Figure 2.20 shows the Power Spectrum Density (PSD) of the x-axis for the three trials performed on each surface. The spectra have been computed by means of the Welch's Method previously described. It is clearly noticeable how the significant frequency ranges tend to decrease

with the roughness, ranging from 700 Hz for 3.2 μm roughness to below 100 Hz for 0.2 μm roughness, enabling slippage detection also in the totality of the cases, also for very low roughness values. This behavior is reasonable, as a rougher surface naturally produces higher frequency vibrations when a relative movement between the surface itself and an object occurs.

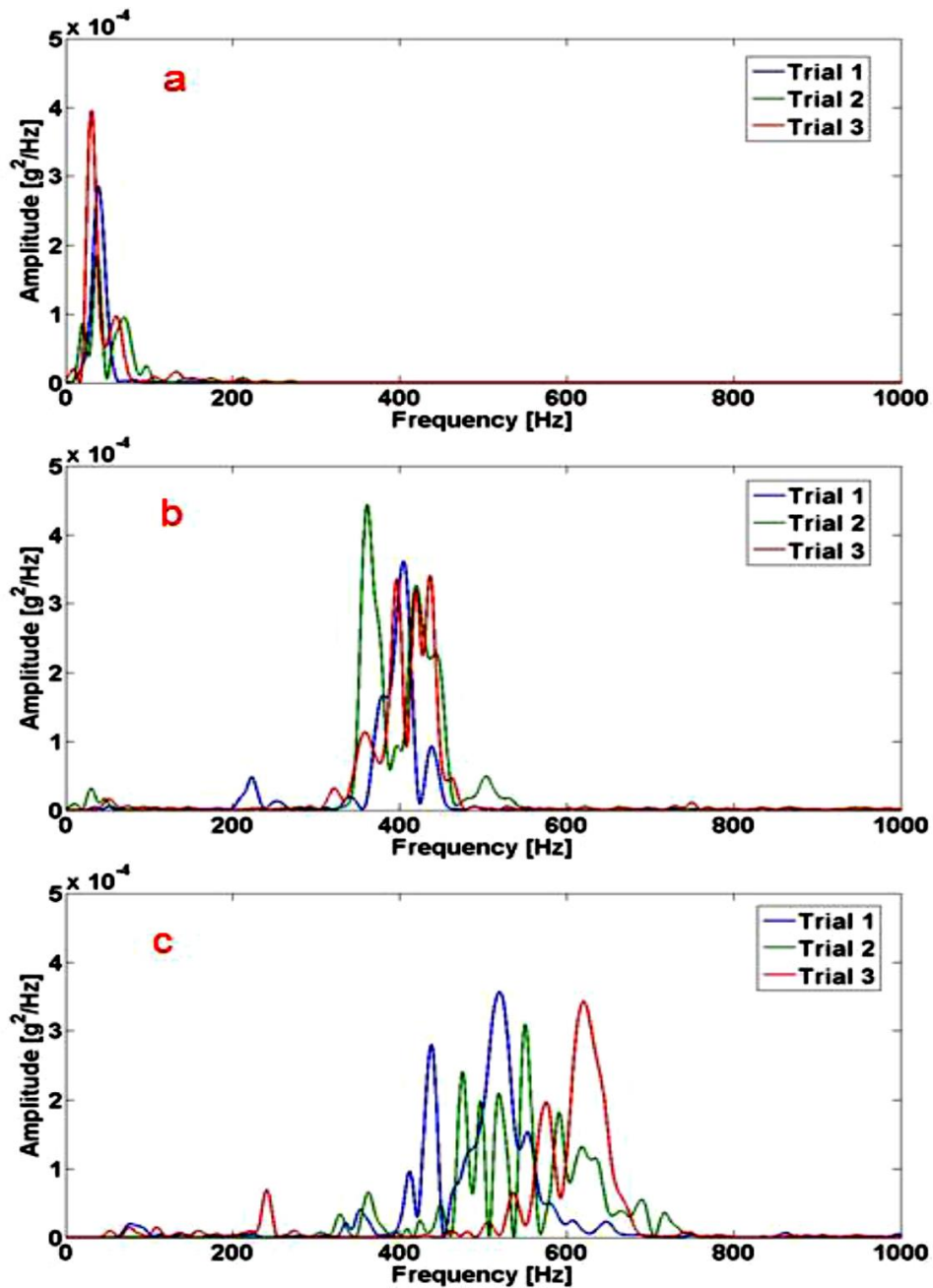


Figure 2.20. PSDs estimated with the Welch's Method for roughness: 0.2 μm (a); 0.8 μm (b); 3.2 μm (c) (Romeo, 2015). © [2015] IEEE.

2.4.3 Validation on human subjects

For an initial evaluation on human subject, grasping tests have been executed with the relevant object created for the tripod grasp. A pre-defined configuration has been selected, as shown in Figure 2.19c: this helped to achieve an as easier as possible force decomposition, along the three axes. One human subject was required to grasp the object and to steadily hold it for around 5 seconds, according to Figure 2.19c. At the equilibrium, when the hand is stably grasping the object with the fingers pushing on its sensitive areas, the measured forces are expected to (approximately) respect the following relation:

$$F_t = Mg + (F_i + F_m) \cdot \sin\left(\frac{\pi}{3}\right) \quad (2.17)$$

where F_t , F_i and F_m are the forces exerted by thumb, index and middle fingers, respectively, while M is the mass of the object and g is the gravity acceleration. Figure 2.21 depicts the force trends of one representative trial performed by the human subject. Considering the force values between the two vertical black bars, i.e. during the stable grasp, it can be stated that they respect the relation (2.11), with a mean error of 0.12 N (± 0.06).

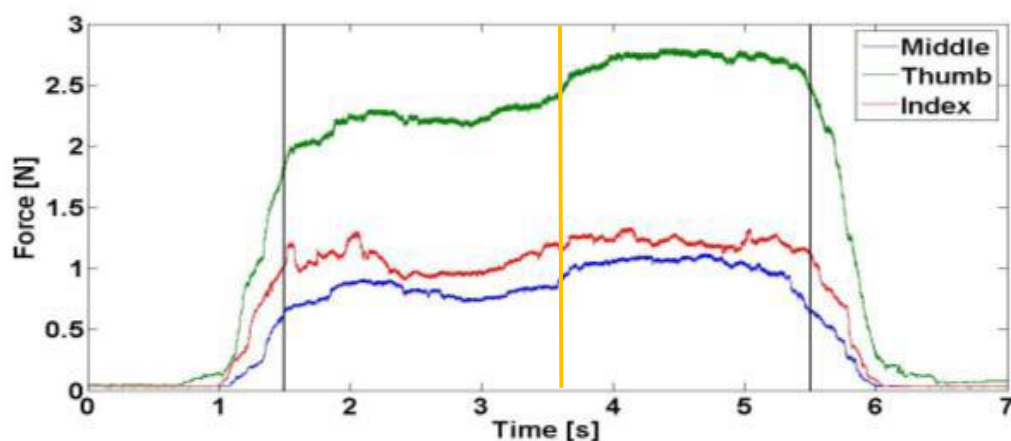


Figure 2.21. Forces exerted by human fingers during a representative trial (Romeo 2015). © [2015] IEEE.

In Figure 2.21, the left black bar was set when all forces reached 70% of the maximum, considering the first half of the plot (i.e., until the orange line). The same applies to the right black bar, but considering the second half of the plot.

Additionally, the subject was also required to grasp the object oriented as in Figure 2.19b, and then to slowly release it until the object fell (in order to simulate slippage conditions). Figure 2.22 shows the outputs of both FSR sensors and accelerometer, as well as the PSD of the accelerometer voltage. For sake of clarity, only the signal relating to the axis directed towards gravity direction (x-axis) is reported in the plot. Black bars delimitate the time window used for spectral analysis: it has been chosen immediately before the object fall, which is highlighted by the peak in the accelerometer signal. It is in this time window that incipient slip occurs, as forces critically decrease. Spectral content corresponding to the slippage event is concentrated below 100 Hz: this is reasonable, considering the very smooth surface of the object.

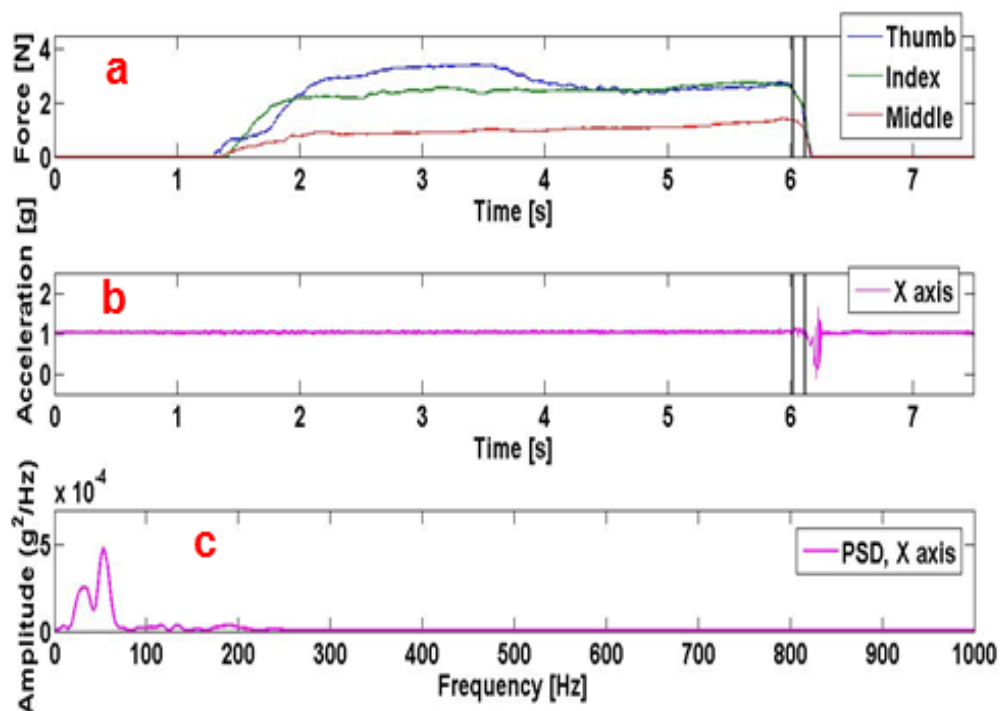


Figure 2.22. Fingers forces (a); x-axis component of acceleration (b); corresponding PSD (c) (Romeo, 2015). © [2015] IEEE.

When the object is held still with the hand, there is not frequency content in the accelerometer voltages. Even when waving the hand grasping the object, the accelerometer signal results in a sinusoid signal with a frequency content inferior to 10 Hz. Considering that the estimated spectrum in Figure 2.22c has significant content up to 70 Hz, it can be affirmed that the described trial has demonstrated the ability of the accelerometer to sense slip events. For this preliminary test, the time window between the black bars has been set to 100 ms, but it can be smaller.

As concerns the forces trend, it can be noticed that the thumb force balances the index and middle fingers, which according to configuration of Figure 2.19b, oppose their action to the one of the thumb. Around the 4th second of the trial, the subject starts to slowly release the object, though the thumb force is the only one that appears to diminish. This is due to the peculiar grasping strategy of the subject; a different subject may have acted in a different way.

2.5 Experimental session with human subjects

After the validation phase, which has been conducted with the aim of verifying the bounty of the first instrumented object prototype, an experimental session has been executed at *Centro Protesi INAIL*, Vigorso di Budrio (BO), Italy. In this experimental session, 7 healthy human subjects have been involved, and have been asked to perform 8 trials. Such trials have been similar to the last one described in Section 2.4: after an initial phase of stable grasp, the subject has been required to slightly release the object until it finally slips. A kinematic analysis, exploiting a given number of markers positioned on every subject hand, has been carried out together with the force and slip analysis, but it will

not be covered by this thesis. Details about the experimental session are given in (Romeo, 2017a).

The configuration employed in these experiments is illustrated in Figure 2.23. During every trial, the subjects have been asked to perform the following actions:

- 1) grasp the object;
- 2) hold it stably for 1-2 seconds;
- 3) start to release the object until it slips.

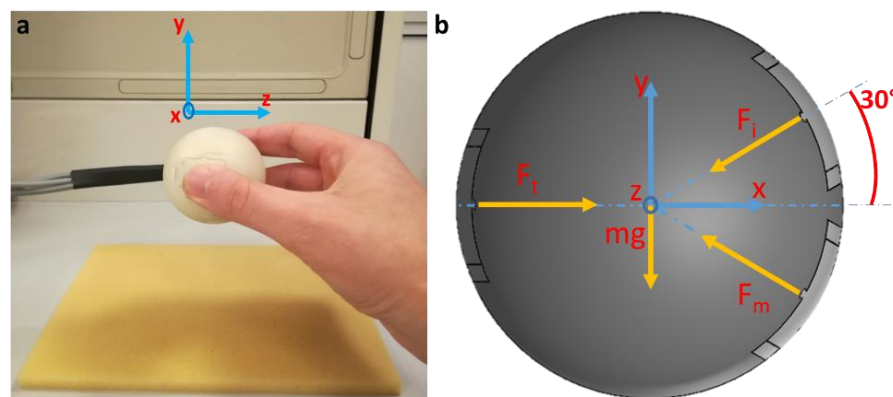


Figure 2.23. Grasp configuration during experimental trials. Lateral view (a); subject frontal view (b) (Romeo, 2017a). © [2017] IEEE.

2.5.1 Grasping forces

When grasping the instrumented object, four different phases can be distinguished, as illustrated in Figure 2.24. Initially, the force level arises quickly because of the finger pressure onto the sensorized areas of the object. After the peak, forces tend to stabilize and then to slowly decrease until the object is completely released. During (1), the subject applies force values between T_{1g} and T_{2g} that are too high for the specific task and that justify the peak in (2). Such a peak is subsequently damped by slowly decreasing grasping forces during (3); this is particularly evident for thumb and middle fingers. Forces go to 0 from T_{r1} to T_{r2} ; the middle finger is firstly removed from the object. As expected, thumb force is greater than index and middle forces. Phases

(1) and (2) comprise the first of the three actions that the subjects have been required to perform (i.e. grasp and lift the object), while (3) and finally (4) correspond to the second and third actions, respectively (i.e. hold it stably for 1-2 seconds, and start releasing the object until it slips).

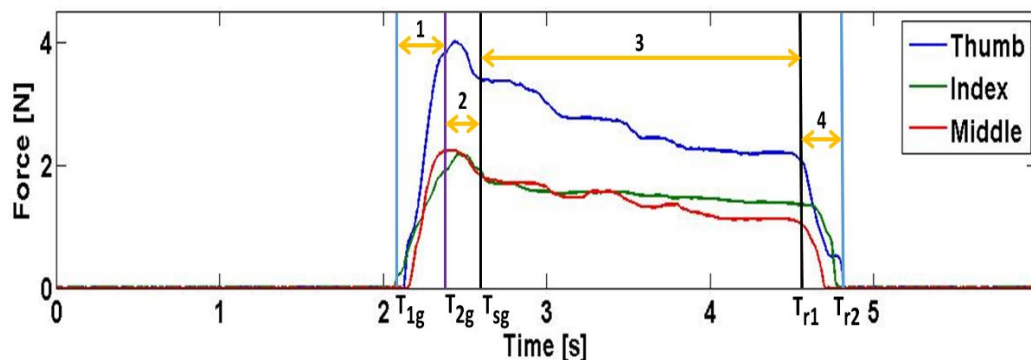


Figure 2.24. Example of grasping task executed by a subject (Romeo, 2017a).
© [2017] IEEE.

Force peak within (2) characterizes the grasping trials in the majority of cases. When the object is grasped, the stable grasp is often preceded by the application of excessively high forces, as for the case in Figure 2.25, for a different subject.

Table 2.3 shows the mean duration of the four grasping phases. A rather high variability can be observed, suggesting that the various subjects exploit diverse strategies for grasping the object; even if phase (2) seems to have similar duration among the subjects, the other phases are characterized by different times, e.g. phase (3) whose mean duration varies from 1.02 to 4.81 seconds. A certain variability can be noticed in the mean grasping forces as well (Table 2.4): maximum mean forces almost reach up to 6 N, whereas some subjects barely overcome 2 N.

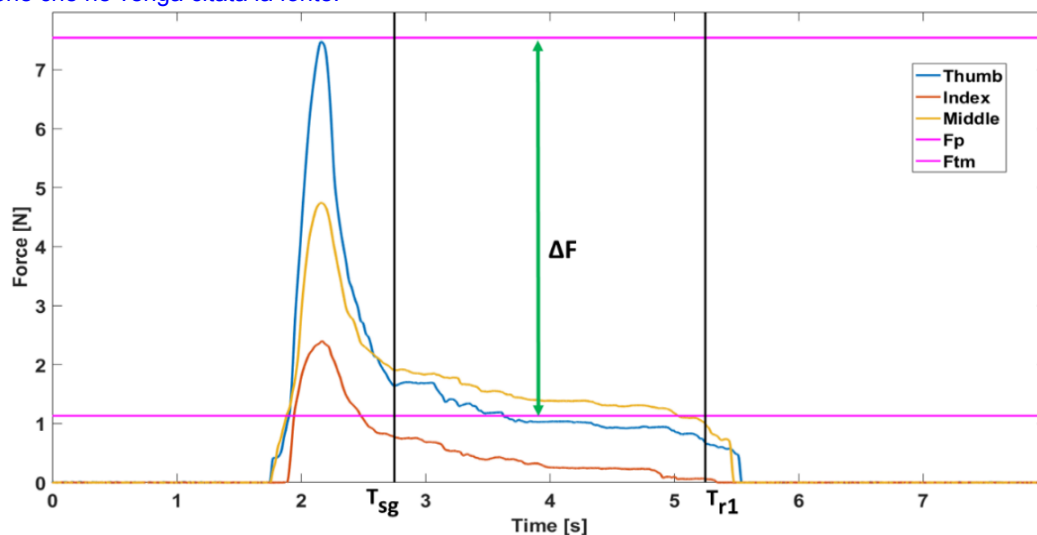


Figure 2.25. Example of grasping trial performed by a subject. F_p represents the greatest thumb force level, while F_{tm} is the thumb mean force value (Romeo 2017). © [2017] IEEE.

Table 2.3. Mean Duration (s) of the Grasping Phases (Romeo, 2017a). © [2017] IEEE.

Subject	Phase 1	Phase 2	Phase 3	Phase 4
1	0.54±0.05	0.69±0.47	3.13±0.43	1.85±0.34
2	0.92±0.03	0.86±0.09	4.81±0.55	2.33±0.73
3	0.51±0.04	0.45±0.13	2.34±0.43	0.98±0.51
4	0.38±0.03	0.54±0.46	2.16±0.48	0.29±0.11
5	0.28±0.02	0.65±0.31	1.02±0.52	0.40±0.14
6	0.19±0.04	0.74±0.21	1.41±0.35	0.53±0.14
7	0.48±0.09	0.73±0.13	1.59±0.74	0.93±0.43
Grand mean	0.47±0.23	0.66±0.13	2.35±1.28	1.04±0.77

Table 2.4. Mean Forces (N) During the Grasping Phases (Romeo, 2017a). © [2017] IEEE.

Subject	Finger	Phase 1	Phase 2	Phase 3	Phase 4
1	Thumb	3.33±1.41	5.51±0.18	5.82±0.15	2.23±1.65
	Index	1.09±0.70	2.19±0.16	2.22±0.05	0.98±0.70
	Middle	1.45±0.59	1.98±0.12	2.32±0.13	0.67±0.71
2	Thumb	1.41±0.85	2.27±0.18	2.05±0.08	0.82±0.38
	Index	0.85±0.37	1.12±0.15	0.98±0.12	0.27±0.36
	Middle	1.21±0.93	2.13±0.08	2.10±0.08	0.83±0.43
3	Thumb	1.74±1.54	4.04±0.99	1.97±0.19	0.93±0.43
	Index	0.72±0.88	2.02±0.35	1.27±0.12	0.50±0.40
	Middle	1.55±0.91	2.72±0.43	1.73±0.13	1.03±0.38
4	Thumb	1.73±1.21	3.73±0.22	2.60±0.40	0.88±0.51
	Index	1.23±0.55	2.32±0.13	1.74±0.11	0.96±0.60
	Middle	1.13±0.94	2.41±0.18	1.59±0.25	0.36±0.43
5	Thumb	1.86±1.33	3.61±0.20	2.00±0.55	0.85±0.38
	Index	1.02±0.57	1.61±0.17	1.08±0.26	0.35±0.31
	Middle	0.64±0.64	1.66±0.11	0.95±0.21	0.45±0.24
6	Thumb	1.74±1.12	2.64±0.30	2.10±0.46	1.19±0.40
	Index	1.10±0.55	1.16±0.21	1.10±0.33	0.49±0.68
	Middle	1.60±1.01	2.51±0.27	2.16±0.26	1.22±0.69
7	Thumb	1.36±1.27	3.85±0.69	1.65±0.09	0.87±0.28
	Index	0.55±0.62	1.66±0.28	0.95±0.15	0.12±0.39
	Middle	1.29±0.80	2.71±0.41	1.39±0.09	0.65±0.05
Grand mean	Thumb	1.88±0.66	3.67±1.04	2.60±1.44	1.11±0.50
	Index	0.94±0.24	1.73±0.47	1.34±0.47	0.52±0.33
	Middle	1.27±0.32	2.30±0.39	1.75±0.48	0.74±0.32

However, the behavior of the subjects appears in this case to be more coherent, as the thumb force dominates in almost all cases, while index and middle fingers balance each other. In some cases, the middle finger exerts a greater force, which is close to the thumb one. In general, it appears to be a common strategy to apply high force values after T_{lg} , leading immediately after to a force adjustment towards lower values.

2.5.2 Object orientation and grasping forces dynamic compensation

The configuration in Figure 2.23 implied a 90-degree rotation with respect to the configuration shown in Figure 2.17, used for the accelerometer calibration. Hence, the starting values of the orientation angles should ideally be 90° (roll) and 0° (pitch). Nevertheless, human subjects cannot perfectly control the two rotations, resulting in a roll

angle $\varphi=90^\circ\pm\alpha$ and a pitch $\theta=0^\circ\pm\beta$; in particular, the pitch angle affects the projection of the forces upon the object frontal plane, enclosed by the X-Y directions in Figure 2.23b. Such a projection allows expressing forces components on the X-axis and Y-axis in the following manner:

$$\begin{pmatrix} F_{xt} \\ F_{xi} \\ F_{xm} \\ F_{yt} \\ F_{yi} \\ F_{ym} \end{pmatrix} = \begin{pmatrix} F_t \cos(\theta_c) \\ F_i \cos(30 + \theta_c) \\ F_m \cos(30 - \theta_c) \\ F_t \sin(\theta_c) \\ F_i \sin(30 + \theta_c) \\ F_m \sin(30 - \theta_c) \end{pmatrix}, \quad (2.18)$$

where 30° is the angle between X-axis and the applied forces of index and middle fingers, and θ_c is the current (absolute) value of the pitch angle during the grasping action.

Figure 2.26 shows the overall forces together with the relevant X-axis components for a given trial. The subject applied a counterclockwise rotation w.r.t. Figure 2.23, starting from $\theta_c = -16^\circ$. Clearly, the most influenced component is the index one, as the value of θ_c is summed to 30° , leading to a lower value of the cosine function. Conversely, thumb and middle components are expected to be very similar to the original ones. It can be noticed from Figure 2.26b that in the middle of the grasping trial the object has been slightly rotated about both pitch and roll axes; the subject has not been required to perform such actions, though he/she involuntarily rotates the object. Such a behavior is present in all the trials.

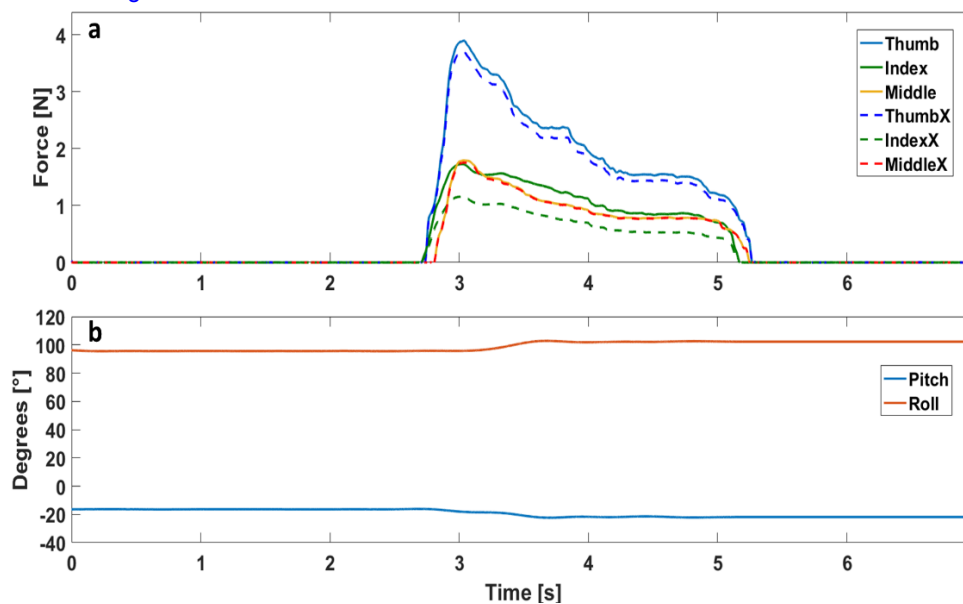


Figure 2.26. Forces and their projections along X-axis during a trial (a); estimated pitch and roll angles (b) (Romeo, 2017a). © [2017] IEEE.

On the other hand, forces along Y-axis (Figure 2.27a) follow the inverse trend: thumb and middle components resulted to be heavily penalized, while index force is quite similar to its overall value. Looking at the accelerometer output in Figure 2.27b, one can observe that the object Y-axis, whose acceleration measurement is close to 1 g, is approximately oriented along the gravity direction (upwards) for the whole trial duration. This is confirmed by the roll angle value (Figure 2.26b), which starts from 95°, in accordance with Figure 2.23.

Table III reports the mean pitch and roll rotations performed during all the trials by the subjects. Such rotations have been calculated as the difference between the last θ_{cf} and the first estimated angle θ_{ci} in each trial. E.g., rotations for the trial in Figure 2.26 are approximately equal to $\varphi=21^\circ-16^\circ=5^\circ$ and $\theta=105^\circ-95^\circ=10^\circ$. Mean rotations values across the whole duration of the trial reported in Table III suggest that the subjects mostly tend to rotate the grasped object about the roll axis. This fact can in some way be due to the power supply cables, whose inertia

induces the object to rotate about X-axis, i.e. the roll axis (see Figure 2.23a).

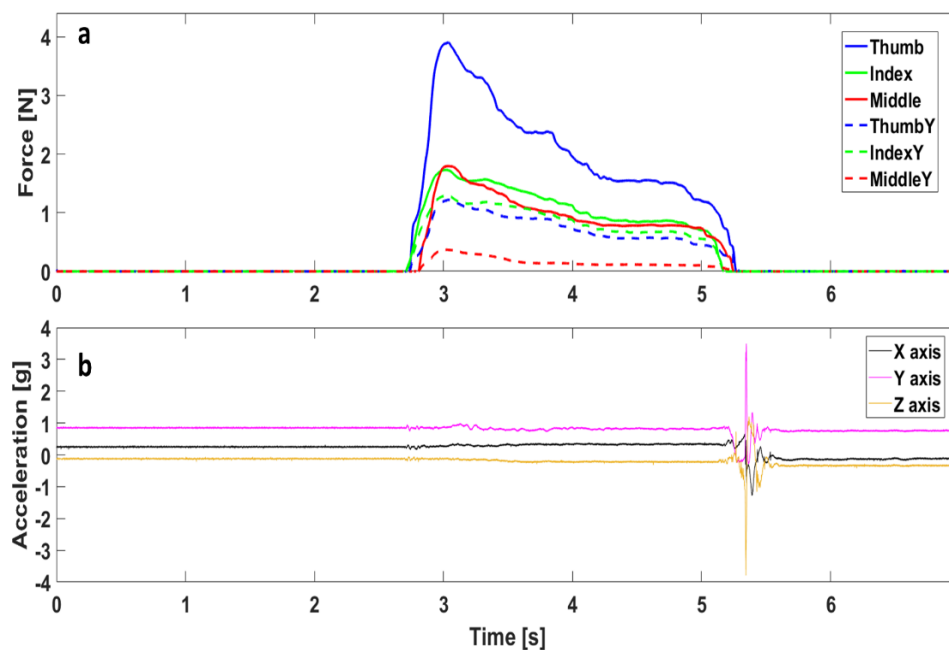


Figure 2.27. Forces and their projections along Y-axis during a trial (a); accelerometer output expressed in g units (b). The peaks after 5 seconds in (b) relate to the fall of the object after it slipped. (Romeo, 2017a). © [2017] IEEE.

Table 2.5. Mean Pitch and Roll Rotations (Romeo, 2017a). © [2017] IEEE.

Subject	Pitch (°)	Roll (°)
1	4.5±1.93	7.65±2.38
2	0.62±0.45	3.65±1.13
3	2.37±1.62	9.28±3.59
4	4.22±2.45	13.83±2.81
5	1.60±0.62	16.81±4.05
6	3.43±1.86	10.98±2.65
7	5.16±2.43	12.15±3.76
Grand mean	3.12±1.65	10.62±4.28

C. Slip detection

The final part of the grasp trials was characterized by the relative movement between sensorized areas and fingers. This movement produced small vibrations that were detected by the accelerometer; such vibrations are associated to a quick drop of the forces, relating to the

contact loss due to slip. The PSD estimation of the vibrations gives an indication about the onset of a slip condition; when the object slips, frequencies up to 250 Hz have been observed. The voltage output of the accelerometer has been high-pass filtered above 10 Hz to prevent false positives from being detected. Figure 2.28c depicts the PSD (estimated through the Welch's method) of the shadowed window (W) for a representative trial.

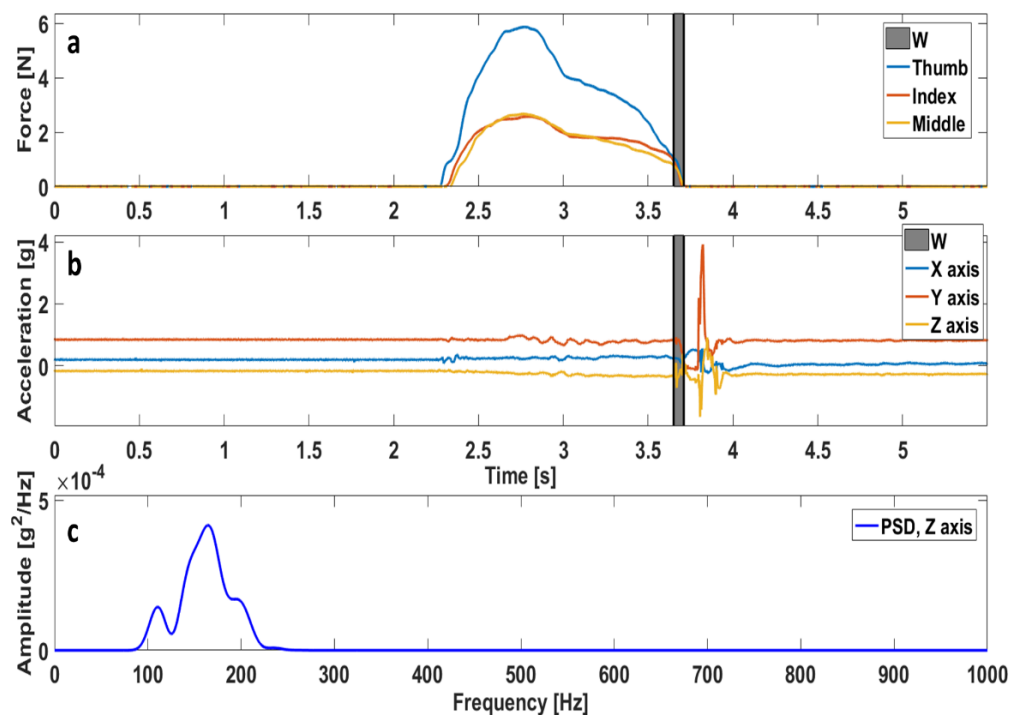


Figure 2.28. Forces (a) and acceleration (b) during a trial. The PSD of the window in the shadowed area is plotted in (c) (Romeo, 2017a). © [2017] IEEE.

The spectrum has been computed on the Z-axis acceleration, although computing it on the other axes yields comparable results. The actual fall of the object is evidenced by the high amplitude acceleration peaks in Figure 2.28b (noticeable in Figure 2.27b as well); it appears about 100 ms after the slippage event, which corresponds to phase (4). The window width W has been set to 60 ms, in order to attain a computational time close to the physiological ones needed for a force adjustment [21].

Frequencies in the band [100-200] Hz attest the slip condition, and forces decrease from approximately 1 N to 0 N. The spectrogram of the Z-axis acceleration shown in Figure 2.29 confirms this finding: high frequency content is absent until the relative movement is occurring, as a strong signal can be appreciated after 3.6 seconds. Indeed, the window W starts at the same time instant, whereas the subsequent peak in the spectrogram relates to the object fall.

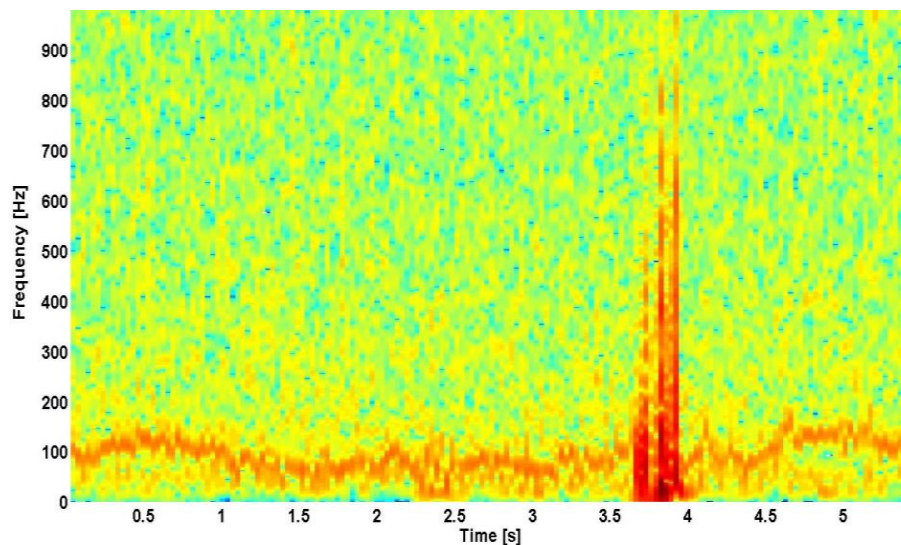


Figure 2.29. Spectrogram computed on the Z-axis acceleration, relating to the trial of Figure 2.30 (Romeo, 2017a). © [2017] IEEE.

A random background noise does characterize the whole spectrogram, although it is more likely to be related to the power supply rather than to the spectrum computation technique. Unfortunately, this noise cannot be filtered out, as it is comprised in the accelerometer meaningful bandwidth; however, its amplitude is inferior than the signal peak due to slip. Moreover, the spectrogram computation in Figure 2.29 is based on the Fast Fourier Transform (FFT), generating thus a noisier outcome than the Welch's Method.

Data related to the slip phase (4) are reported in Table I (in terms of mean duration) and in Table II (in terms of mean forces). Within this phase, mean force values are the lowest of all the phases: this is

reasonable, given that the object is being released by the subject. These values rarely overcome 1 N. Moreover, it can be seen how the mean duration of the slip phase (4) is inferior than 1 second in most cases. The subject spends less than 1 second between the time instant when he/she starts releasing the object and completely releases it. It can be noticed from Table I that the two subjects (Subject 1 and Subject 2) whose trials has the longest mean duration are also evidently slower in releasing the object. This might be a part of their grasping strategy, which induces them to perform grasping actions in a slower way. The window W is applied within phase (4); although its duration is limited to 60 ms, the slip event has been correctly detected for all the 56 trials.

2.6 Conclusions

In this Chapter, the development of a set of three instrumented objects for evaluating the applied force during grasping has been illustrated. The objects embedded sensors for force measurement and an accelerometer for acceleration as well as orientation estimation. A printed electronic board has been wedged inside the objects, hosting the accelerometer and the connectors for interfacing with the force sensors; the board served for collecting the outputs signals from the all the sensors, and was powered by an external power supply.

In order to guarantee an appropriate usage during experimental phases, the sensors embedded in all the instrumented objects have been calibrated; a static calibration has been done to retrieve the best fit curves of the force sensors, while the accelerometer has been calibrated so as to quantify its axis sensitivities and offsets. Such values are indispensable for using the accelerometer as an inclinometer, in addition to its traditional function of acceleration sensor.

After the calibration procedures, the reliability of the instrumented objects has been evaluated on the human hand tripod grasp object, and extended to the other two. Performed experiments have regarded: (i) comparison of the force sensors measurements with a ground truth; (ii) investigation of the accelerometer ability to detect slippage for different roughness values; (iii) assessment of grasp trials performed by a human subject with the object.

In the first step, forces measured by means of a robotic hand (DLR-HIT Hand II) torque sensors have acted as ground truth. In the second step, low roughness surfaces have been employed to execute slip tests through an automated set-up, in which the instrumented object was moved upon the surfaces with fixed velocities and accelerations. In the third step, a human healthy subject has been asked to grasp the object and to grasp it stably, but also to simulate the slip condition by slowly releasing it until the object fell. An experimental session has been carried out at the Centro Protesi INAIL, Vigorso di Budrio (BO), Italy, involving seven human healthy subjects. Analysis in terms of force, slippage and orientation has been performed for every involved subject.

At this first stage, the instrumented objects have been used for increasing the comprehension of the grasping strategies in healthy subjects. The obtained results encourage to utilize the designed objects as evaluating tools for grasp capabilities in humans as well as in robotic and prosthetic hands.

Tesi di dottorato in Bioingegneria e bioscienze, di Rocco Romeo,
discussa presso l'Università Campus Bio-Medico di Roma in data 16/10/2017.
La disseminazione e la riproduzione di questo documento sono consentite per scopi di didattica e ricerca,
a condizione che ne venga citata la fonte.

Chapter 3 Prosthesis sensorization

Chapter 2 has already pointed out the importance and the complexity of the human hand. Its intrinsic and extrinsic muscles allow producing every hand movement: the former are placed within the hand structure, while the latter are included in the forearm. The median, ulnar and radial nerves are responsible for all the hand muscles activation: intrinsic ones are innervated by median and ulnar nerves, which allow a fine control of each finger movement, whereas extrinsic ones, mostly innervated by median and radial nerves, are involved in flexion/extension tasks of the whole hand and in delivery of high forces.

A crucial feature of the human hand (and more in generally, of the human body) is the *sense of touch*. Thanks to this sense, when the human hand grasps an object, its properties can be inferred, e.g. roughness, temperature, weight etc. Moreover, it is fundamental for avoiding the slippage of the grasped object; it also allows to correctly apply forces onto the object, so as not to damage it. Human hand tactile signals, collected by different kinds of receptors, can be restored through the joint use of artificial sensors placed on a prosthesis, and of neural interfaces for the stimulation of peripheral nerves.

The hand loss causes severe impairment for the amputee and can significantly reduce quality of life. The relevance of the upper-limb loss in the international scenario (4000 people per year in Italy (Ciancio, 2016) and 340000 people living with limb loss in USA (NLLIC, 2007)) motivates the flourishing research in the field of upper-limb prosthetics. In the last 70 years, there have been significant improvements in the upper limb prosthetic field thanks to the advancements in the technological field and in the surgical procedures.

Prostheses are more and more conceived to reproduce aesthetical as well as functional features of the lost limb, thus fostering improvements in hand design, control and sensory feedback, in order to meet prosthetic user needs (Biddiss et al., 2007). Notwithstanding, the current state of art regarding commercial prosthetic hands reports only one case of device (Sensorhand Speed by Ottobock©) provided with a feedback from tactile or force sensors (Ciancio, 2016); this confirms that tactile sensing technologies are not easily applicable on prosthetic systems yet. Commercial prostheses are typically velocity- or position-controlled; no tactile system is integrated in the hand and the success of the grasp is based on the visual feedback of the amputee (Ninu, 2014). Furthermore, it is worth noticing that research groups and activities focused on tactile investigation have traditionally been minor than on other sensing principles (e.g., artificial vision), thus leading to a slower development of the tactile technology (Dahiya, 2013).

In this Chapter, a tactile sensorization system for a prosthetic hand, namely IH2 Azzurra (by Prensilia srl), will be described. Its specifications, as well as its implementation, will be detailed in order to provide an advancement in the relevant state of art. Besides the fingers, the IH2 palm has been sensorized with a given number of tactile sensors, so as to extend the sensorization to the whole hand; the idea is to allow closing the control loop both in terms of force/slip information collected by the control system and of restored tactile feedback for the prosthesis wearer. To this end, the sensorized prosthesis has been implanted in an amputee subject for the final experimentation of the PPR2 Project, funded by INAIL (cup E58C13000990001). Its scientific focus was the control of a prosthetic hand, provided with tactile feedback, through invasive stimulation of peripheral nerves.

3.1 Sense of touch: classifications

3.1.1 Sense of touch: definitions

The *sense of touch* in humans comprises two main sub-modalities, i.e. *cutaneous* and *kinesthetic*, depending on the site of sensory inputs (Dahiya, 2009). The first modality gathers sensory inputs from the receptors embedded in the skin, requiring physical contact with the stimuli and providing awareness of the stimulation itself (Loomis, 1986). The second modality takes sensory inputs from the receptors of muscles, tendons, and joints (Loomis, 1986; Graziano, 2002), providing information about body postures, both static and dynamic. This information relates to the position of the body segments, such as limbs, torso and head, and is not independent from the cutaneous information as it exploits afferent information from skin.

According to more recent definitions (Klatzky, 2003), a third modality should be mentioned when discussing the tactile system: i.e., the haptic perception. It can be regarded as the integrated use of the sensory information achieved at the cutaneous level, due to physical interaction with the grasped object, and of kinesthetic information provided by proprioception. As a consequence, the perception of a stimulus can be not only categorized as cutaneous or kinesthetic, but also as haptic. In general, cutaneous events are defined as *tactile* or *tactual*, though the last adjective might be considered as a synonym of haptic. Commonly, the act of touching an object can be distinguished between *active* and *passive*:

- in the first case, the finger, or whatever body embedding tactile sensors, explores a given tactile stimulus or an object,

- vice-versa, in the second case the finger touching the tactile stimulus is maintained still, with the moving and thus producing the tactile sensation.

From these definitions, it is easy to imagine how the ADLs usually imply active touch. An exception is represented by slippage: in this case, the grasped object moves with respect to the hand fingers.

3.1.2 Sense of touch: neurophysiology

Human skin embeds a great number of sensing units. These units are responsible for all the tactile perception induced by external stimulation; i.e., not only mechanical stimuli but also temperature and pain sensation. Mechanical stimuli are mediated by *mechanoreceptors*, while *thermoreceptors* and *nociceptors* encode temperature and pain sensation, respectively. The spatial distribution across the human body is variable: e.g., an estimated mechanoreceptors number of 241 units/cm² characterizes the fingertip, whereas only 58 units/cm² are on the hand palm (Johansson, 1979).

Figure 3.1 gives an illustration of the mechanoreceptors morphology, classification and positioning in the glabrous skin. According to the characteristics of the response, they can be distinguished between slow-adapting (SA) and fast-adapting (FA). The former show a slow rate of adaptation, while the latter have a quicker rate. Each of the two groups includes receptors with small receptive field (type I) and receptors with large receptive field (type II). More specifically, human mechanoreceptors are classified as follows:

- Meissner corpuscles (FA I)
- Pacinian corpuscles (FA II)
- Merkel discs (SA I)
- Ruffini endings (SA II)

Fast-adapting receptors are sensitive to skin vibrations, with FA I coding the low-frequency vibrations and FA II coding the high-frequency vibrations. They respond during the transient phases of the stimulus, while slow-adapting receptors activate during static stimulation as well and are responsible for the perception of roughness (SA I) and skin stretch (SA II).

3.1.3 Skin mechanics and information encoding

Human skin intermediates every tactile sensation, being the first elaboration stage of the tactile sensation. It has a multilayered structure, with nonlinear and viscoelastic characteristics. The *epidermis*, i.e. the most external layer, is separated from the *hypodermis*, i.e. the most internal layer, by the *dermis*. Every layer has its own stiffness: notably, the epidermis is 10000 times stiffer than the dermis (Dahiya, 2009), and the relative sliding of the two layers is avoided as they are solidly interlocked. Intermediate ridges, which must not be mistaken with papillary ridges (placed superficially), produce an amplification in the tactile signal thanks to their *micro-lever* behavior. Figure 3.1 gives an illustration of the skin layers and ridges. On the other hand, papillary ridges are highly useful when grasping an object as their presence results into a significant grip augmentation (Maeno, 1998). Though papillary ridges are different from intermediate ones, their centers coincide (Dahiya, 2009).

Many phenomena, of various nature, normally take place from the skin stimulation until the generation of a clear perception. The skin adapts its surface to the object which comes to be grasped or simply touched. A huge number of mechanoreceptors is thus involved, and each of them activates with a threshold mechanism yielding voltages spikes as the

stimulus overcomes the threshold. In this way, the stimulus is coded through a train of action potentials.

Figure 3.1 shows the whole path followed by tactile signal. Information related to the contact between the skin and the object is brought to the CNS after being collected by PNS nerves (such as forearm nerves), where higher elaboration is done. The principal pathways are the spinothalamic and the dorsal-column-medial-lemniscal (DCML); the former carries pain and temperature sensation, at slower velocities than the latter, which relays information related to pressure and vibration, besides helping in spatio-temporal discrimination.

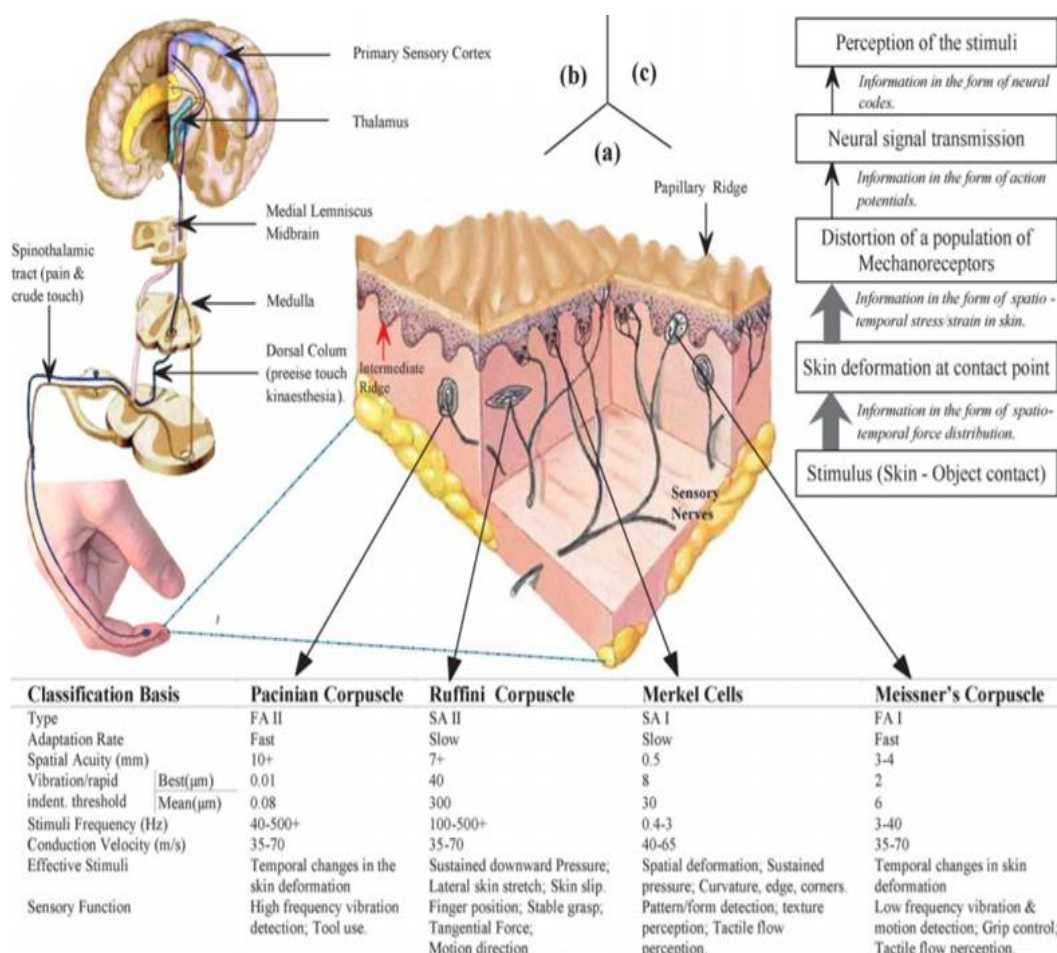


Fig. 3.1. Section of glabrous skin with detail of mechanoreceptors location and properties (a); tactile signal path (unidirectional) from fingertip to somatosensory area of brain (b); events sequence during tactile signal transmission from contact point to the brain (c) (Dahiya, 2009). © [2009] IEEE.

3.2 State of the art on tactile sensing for prosthetic hands

As in humans, touch sensing would be of great help in augmenting the naturalness and the biomorphism of humanoid robots, which are more complex than common industrial robots as they are called to interact with men, simulating human structure and behavior (Dahiya, 2009). Sense of touch is fundamental for understanding the interaction with a real-world object, which depends on its weight and stiffness, on how its surface feels when touched, how it deforms on contact, and how it moves when pushed. Even though sense of touch has great importance, it has not yet paid any major attention to it if considering the development of other sensory modalities. This could partly be attributed to the complex and distributed nature of sense of touch and partly to the absence of satisfactory tactile sensors or *taxels* that can be incorporated in humanoid robots (Dahiya, 2009), as well as in a prosthetic limb. Over the past two decades, investigation of artificial tactile sensing has resulted in a large number of touch sensors, exploring variegated modes of transduction. Production of tactile sensors with innovative designs still continues, but they largely remain unsatisfactory for prosthetic (for robotic in general) usage either because they are too big to be used without sacrificing dexterity or because they are slow, fragile, lack elasticity, lack mechanical flexibility, and lack robustness. Moreover, the information provided to the prosthesis control system is often not reliable.

As a consequence, prosthetic hands endowed with an artificial tactile system are almost nonexistent. The current state of art regarding commercial prosthetic hands reports only one case of device provided with a feedback from tactile or force sensors (Ciancio, 2016); this confirms that tactile sensing technologies are not easily applicable on prosthetic systems yet.

3.2.1 Sensorized prosthetic hands: state of the art

The content of this Subsection can be found in (Ciancio, 2016), coauthored by the author of the present thesis, and is the result of his contribution to the cited paper (including Figure 3.2).

The sensors usually embedded in artificial hands, for prosthetics as well as robotic applications, typically belong to two different categories: position sensors, for providing hand proprioceptive-like information, and force/tactile sensors, for measuring the interaction with the external environment. Over the years, a number of researchers has developed tactile sensors based on a huge variety of functioning principles. Force measurements as well as surface properties (e.g., hardness, roughness, temperature etc.) can be inferred from tactile sensors. Yet, providing a prosthetic device with reliable tactile information still represents a very tough challenge in the robotic and prosthetic fields.

Piezo-resistivity is one of the more commonly adopted principles for tactile sensors being quite simple and cheap. Piezo-resistive force sensors were employed in the fingertips of the Utah-MIT Hand (1986) (Figure 3.2A), one of the first developed robotic hand for prosthetic use. The sensing element (Allen, 1990) comprised 256 elements organized in a 16×16 matrix inserted between two deformable Kapton sheets. Similarly, the Belgrade-USC Hand (1988), used piezo-resistive elements located in the fingertips for force measurements and contact detection (Martell, 2007).

The MARCUS hand (1992), a device with a three-fingered polyarticulated for myoelectric prosthesis, was developed. The hand was equipped with position, force and slip sensors while a sensor-based control allows it to maintain a stable grasping of the object without affecting the user attention.

Force Sensitive Resistors (FSR) technology exploits piezo-resistivity too. They have been largely used in prosthetics since 90s. FSR sensors are made of polymeric thin films with variable electrical resistance, their small size is ideal for hand prosthetic usage. They suffer from a certain non-linearity in the response; however, their great sensitivity at low forces constitutes a remarkable feature from a tactile point of view (Chappell, 2011). In the Gifu Hand II, 2001 (Figure 2B) a total number of 624 active elements collecting the tactile signals thanks to a layer of conductive ink whose electrical resistance changes in relation to the applied stress on the active elements surface. In addition, 6-axis force sensors have been placed on each fingertip (Kawasaki, 2002). In the successive release of the hand, the Gifu Hand III (Mouri, 2002) 235 additional active elements have been used.

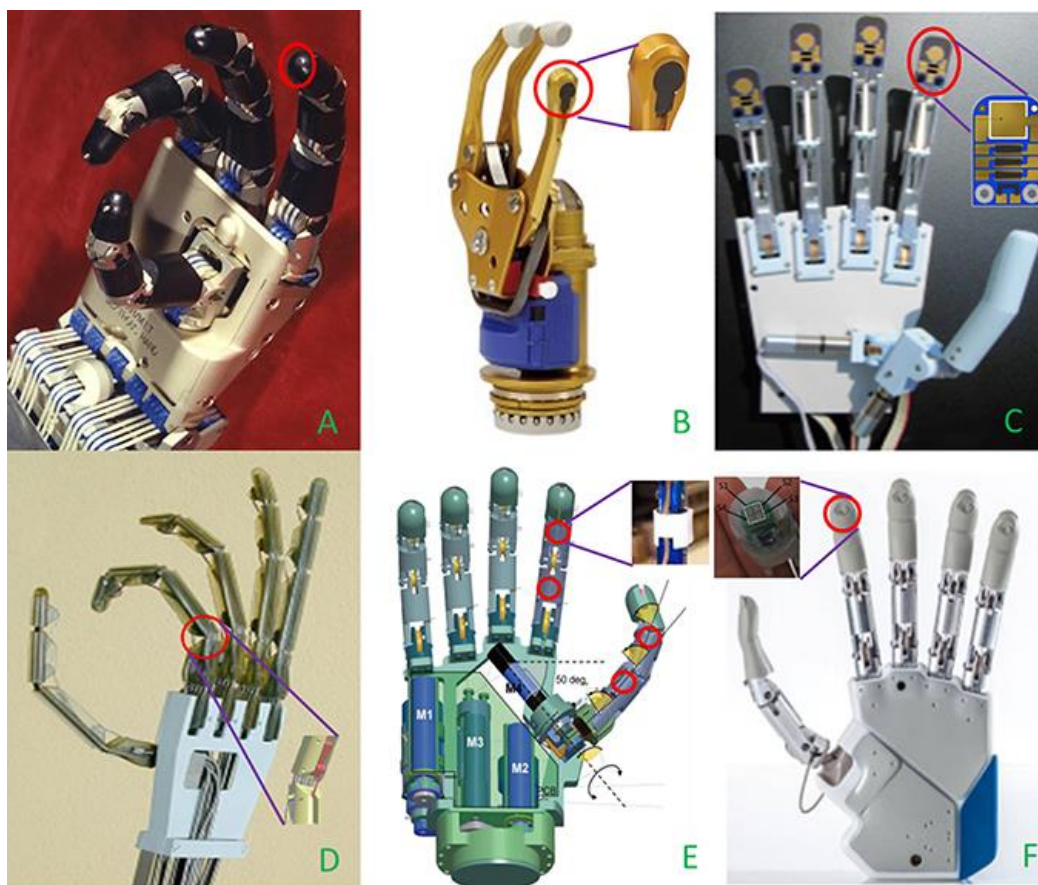


Figure 3.2. Details of the force/tactile sensors (red circles) embedded in the described prosthetic hands (Ciancio, 2016).

In the first years of this century, embedded solutions for force/tactile sensors have been progressively adopted, with particular attention to the problem of slippage phenomena occurring during manipulation and grasp tasks. The piezo-electric materials are particularly appropriate for slippage detection, because of the high sensitivity to micro-vibrations and the low cost (Cotton, 2007). However, their main drawback is that vibrations due to other events, different from slippage, might lead to inappropriate activations of the sensors, and as a consequence, to noise generation. Moreover, their output is temperature dependent, particularly evident in sensors based on polymeric materials [e.g., polyvinylidene fluoride (PVDF)], that are widely exploited as tactile sensors.

Southampton REMEDI Hand, 2001 (Figure 3.2C), relies on two different physical principles in order to gain tactile information from the interaction with the objects (Cotton, 2007): FSR sensors, employed for force estimation, and a piezoelectric layer (lead zirconate titanate, PZT) on the fingertips to detect slippage.

Alternatively, traditional force sensors based on strain gauges can be utilized. Load cells are able to provide accurate force measures: the UBH III hand, 2003 (Figure 3.2D) has been mounted with some load cells located close to each actuated phalanx (Lotti, 2004).

Lately, the research interest in optoelectronic technology is growing. It offers a number of advantages, such as optimal accuracy, good linearity, absence of electromagnetic interference and hysteresis in sensors measure. Typical disadvantages derive from a more complex electronics, from the typically high currents needed for supplying photodiodes, and from the light attenuation deriving from microbending in the walls of the light guide. The idea to use an optical

sensor array to detect slipping was implemented in a commercial hand in 1998 at INAIL prostheses center, but the impact on the cosmetic glove was unacceptable (Tura, 1998). The Smart Hand, 2008 (Figure 3.2E), is a good example of application of optical sensors array. It embedded 4 optoelectronic sensors, 2 in the proximal and intermediate phalanges of the index, and 2 in proximity of the metacarpophalangeal (MCP) and interphalangeal (IP) joints of the thumb (Persichetti, 2007; Cipriani, 2011). The structure of the sensor included an infra-red (IR) photodiode, a phototransistor and a silicone cover.

Finally, tactile sensors can be fabricated by means of MEMS technique, with considerable reduction of sensors bulkiness. (Oddo, 2011a) offers a solution in this sense, embedding in each fingertip a 2×2 matrix of MEMS piezo-resistive sensors: each sensitive element of the matrix included 4 active units, for a total of 16 units in a surface of 0.22 cm^2 , corresponding to 72 units/cm^2 (a quantity close to the density of Merkel Disks in the human fingertip, i.e. 70 units/cm^2). Discrimination of ridged surfaces has been performed by means of such sensors (Oddo, 2011a); moreover, the restoration of ability to judge textures has been achieved via an integrated approach using a neuromorphic process and a sensorized artificial finger that integrated the above mentioned MEMS (Oddo, 2016). A possible prosthesis which might embed such sensors might be the IH2 Azzurra hand (Figure 3.2F).

Other transducing principles have been investigated by researchers, e.g., capacitive, magnetic, quantum tunnel, thermic, acoustic tactile sensors, and fiber optic based sensors (Dahiya, 2009; Francomano, 2013; Saccomandi, 2014). Although being regarded as promising technologies, there are not available prosthesis integrating similar tactile sensors, yet.

On the other hand, looking at the panorama of commercially available prosthetic hands, only the Sensorhand Speed (2002) by Ottobock® (Figure 2E) is provided with a slippage detecting system mounted on the thumb, namely the SUVA Sensor System. It is made of three sensors disposed at angles of 120° and is able to detect slippage by constantly monitoring the position of the gravity center of the object and, consequently adjusting the grasp force level in case of necessity.

More recent models of multifingered commercial hands (e.g. the iLimb by Touch Bionics (2007), the Bebionic by RSL Steeper (2010) and the Michelangelo by Ottobock (2010) are not provided either with force or tactile feedback. Different grasps can be executed thanks to predefined grip patterns and hand intrinsic compliance.

Moreover, the sensors selection must consider the presence of the cosmetic glove and the characteristics of the glove itself, the contact area and the capability to accept direct loads.

3.2.2 Artificial tactile system: specifications

When developing an artificial tactile system, some basic design criteria can be formulated; they can be regarded as quite general, though every robotic/prosthetic system might need some particularization according to its shape, materials and functionalities. The above said criteria have been retrieved from literature (Howe, 1994; Dargahi, 2004; Dahiya, 2009), and are summarized in the following:

- 1) Multi-functionality of sensors, as they should be preferably able to measure not only contact force but other object properties, such as temperature. Further, the capability to detect slippage is crucial. The quantity of such sensors can be varied according to the body site, as well as on the geometrical and material features of this body.

- 2) High sensitivity and acceptable measurement range. Manipulation tasks are commonly performed with forces included in the interval [0.15–0.90] N (LaMotte, 1987). Force measurement up to 10 N is desirable (Dario, 1989).
- 3) Dynamic response. Taxels should deal not only with static events but with dynamic events as well. To this purpose, more than one transduction principle might be employed.
- 4) The response of the taxels should respond as quickly as possible. The use of tactile feedback in an artificial hand control system unavoidably requires this feature. Generally speaking, a 1-ms response time may be sufficient for real time applications.
- 5) As already referred in Section 3.1, tactile information undergoes some levels of pre-processing before being elaborated by the brain. At the same way, adding some pre-processing of the data collected by the tactile sensors may help reduce the complexity of information relayed to the artificial CPU.
- 6) To enhance their answer, covering materials (e.g. plastic packages) can be adopted, mimicking in some way the tactile receptors embodiment in the skin. Great attention has to be paid to this aspect in the prosthetic domain, as the prosthetic hands are always covered with cosmetic gloves. Although the presence of elastic material often introduces some mechanical filtering effects, the increase of the contact area, and consequently of the sensing area, greatly advantages manipulation actions. The covering fabrication might foresee external protuberances like the skin papillary ridges for grip augmentation.
- 7) Taxels structure is supposed to be robust. Moreover, they have to cope with difficult environmental conditions, in terms of humidity

and temperature but also of chemical and electrical disturbance. On the other hand, a certain flexibility is demanded, as taxels should conform to the grasped objects.

- 8) Hysteresis should be very low. Even if the human tactile response is quite hysteric and nonlinear, for sake of ease artificial taxels should exhibit a repeatable, possibly linear behavior.

As already stated at the beginning of this Subsection, the listed requirements are highly application dependent and therefore their definition should not be considered univocal.

3.3 The proposed tactile sensory system

To correctly cope with the tactile sensorization of a prosthetic hand, appropriate sensors must be chosen with the aim of making it able to correctly detect the applied force and the slippage events that may occur during manipulation/grasp tasks. Indeed, a satisfactory closure of the control loop must foresee not only the possibility to measure the forces through the tactile sensors, but also to regulate their level according to the necessity. Thus, the slip information comes to be of vital importance. Given a prosthetic device, and the problem of its tactile sensorization, the first two considerations to do are about:

- individuating the transducing technologies for the forces (and eventually other quantities) measurement;
- selecting the prosthesis points, or areas, where to place the tactile sensors.

3.3.1 Tactile sensitive elements

The first of the points above has been addressed by the individuation of a technology which could satisfy all the requirements listed in the previous Subsection, or at least the major part of them. After a

preliminary evaluation of all the available transducing principles, the piezo-resistive one has been chosen. The employed taxels belong to the FSR family, i.e. FSR 402 by Interlink Electronics. These ones function in the same way as the ones used for the instrumented objects, as they are part of the same series (400 Series), though they have wider sensitive area (14.68 mm diameter). Details about their calibration procedure and the metrological properties have been provided in Chapter 2; in this Subsection, a brief description of their construction will be given. Figure 3.3 depicts an exploded view of the sensor, together with a real image of an FSR 402 model.

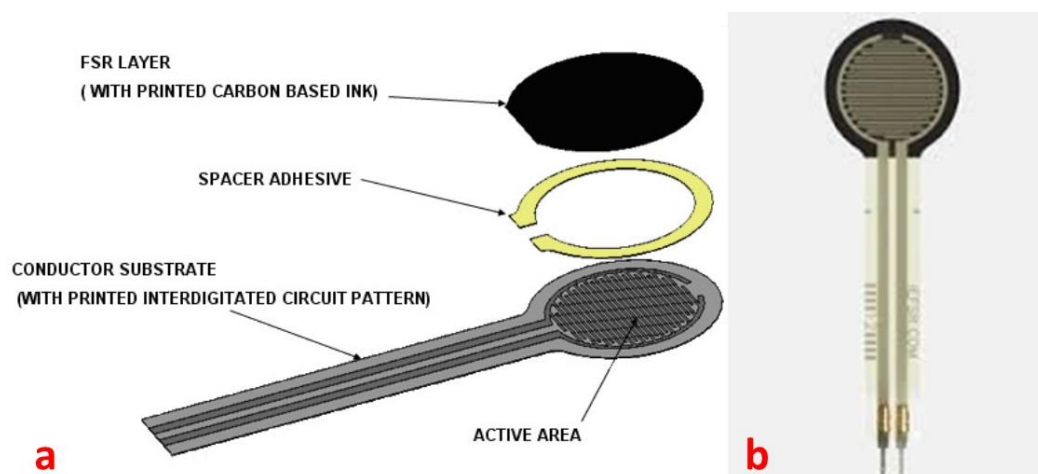


Figure 3.3. Exploded view of the FSR 402 sensor (a); FSR 402 sensor (b).

FSR sensors are formed of two polymeric flexible membranes, which are divided by an air gap. Such a gap is maintained by a spacer adhesive between the two membranes, ranging from 0.03 mm to 0.15 mm. FSR carbon-based ink internally covers one of the membranes, while the other one has two sets of interdigitated fingers that are electrically disconnected: each set is connected to one trace on a tail as shown in Figure 3.3. As a force is applied onto at least one sensor side, the ink-covered surface shorts the two interdigitated fingers of the facing surface. In this way, the electrical resistance between the fingers decreases: the highest the applied force, the lowest the resistance.

The chosen tactile sensors respond to the previously listed specifications, because they:

1. are multi-modal, as they are able to detect forces level and slippage events. The latter functionality will be described in depth within the next Chapter;
2. have a force range [0.2-20] N, besides a satisfactory dynamic range;
3. are able to detect both static and dynamic events; thus, no additional sensing units, often featuring different transducing principles, are needed;
4. respond very quickly, boasting a response time inferior than 3 μ s;
5. produce an output (electrical resistance variation) that can be easily converted into a useful physical quantity (voltage);
6. can be covered or encapsulated with plastic materials such as silicon or polyvinyl chloride (PVC) without loss of performance;
7. have optimum flexibility, although not being very stretchable; they also can bear challenging temperature and humidity conditions, and do not suffer electromagnetic disturbance, nor do they generate it (Table 3.2);
8. show linear output in double logarithmic coordinates and a relatively low hysteresis (+10%). Finally, their response has good repeatability, monotony and stability in the whole force range.

Tables 3.1-3.2 (taken from the [product integration guide](#)) summarize the characteristics of the FSR 402.

Table 3.1. General characteristics of the FSR 402 sensor.

General		
PARAMETER	VALUE	NOTES
Force Sensitivity Range	~0.2 to 20N	Dependent on mechanics
Break Force (Activation Force)	~0.2N min	Dependent on mechanics and FSR build
Part-to-Part Force Repeatability	± 6% of established nominal	With a repeatable actuation system, single lot.
Single Part Force Repeatability	± 2% of initial reading	With a repeatable actuation system
Hysteresis	+ 10% Average	$(R_{F+} - R_{F-})/R_{F+}$
Long Term Drift	< 5% per $\log_{10}(\text{time})$	Tested to 35 days, 1kg load
Force Resolution	Continuous	Depends on measurement electronics
Stand-Off Resistance	> 10M Ω	Unloaded, unbent
Switch Travel	0.05mm	Typical; depends on design
Device Rise Time	<3 microseconds	Measured with drop of steel ball
Maximum Current	1 mA/cm ² of applied force	
EMI / ESD	Generates no EMI; not ESD sensitive	

Specifications are derived from measurements taken at 1000 grams, and are given as (one standard deviation / mean), unless otherwise noted.

Table 3.2. Environmental characteristics of the FSR 402 sensor.

Environmental Performance Specifications		
PARAMETER	TYPICAL R CHANGE	NOTES
Hot Operation	-15%	85°C after 1 hour
Cold Operation	-5%	-40°C after 1 hour soak
Hot Humid Operation	+10%	+85°C, 95% RH, after 1hour
Hot or Cold Storage	-10%	-25°C to +85°C, 120hrs
Hot Humid Storage Temperature	+ 30% of established nominal resistance	+85°C, 95% RH, 240 hours
Thermal Shock	± 2% typical	-25°C to +70°C, 10 Cycles, 15 minute dwell, 5 minute transitions

Note: Specifications are derived from measurements taken at 1000 grams.

3.3.2 *Tactile sensors positioning*

As regards the points to sensorize, they have been chosen according to the observation of the involved prosthesis areas during various grasp trials performed with different objects (such as plastic bottle, plastic cup, highlighter, tennis ball, pen, knife, egg, etc.) and to the literature investigation. In particular, (Kargov, 2004) performs a compared analysis of the grasp forces exerted by the human hand versus the grasp forces exerted by some prosthetic hands; forces have been evaluated by merely attaching a given number of (piezo-resistive) tactile sensors.

Noticing that some of the sensorized areas coincide with the prosthesis (IH2) areas coming into contact with the grasped objects, the selected points to equip with tactile sensors have been:

- each fingertip;
- MCP joints of index, middle, ring and little finger;
- thenar eminence of the palm.

Figure 3.4 illustrates the IH2 hand and the chosen points. Considering the hand and sensors dimensions, a total amount of nine sensors has been considered to be enough. Three of these, respectively on thumb, index and one of the MCP joints, will be used for slippage detection besides force level computation.

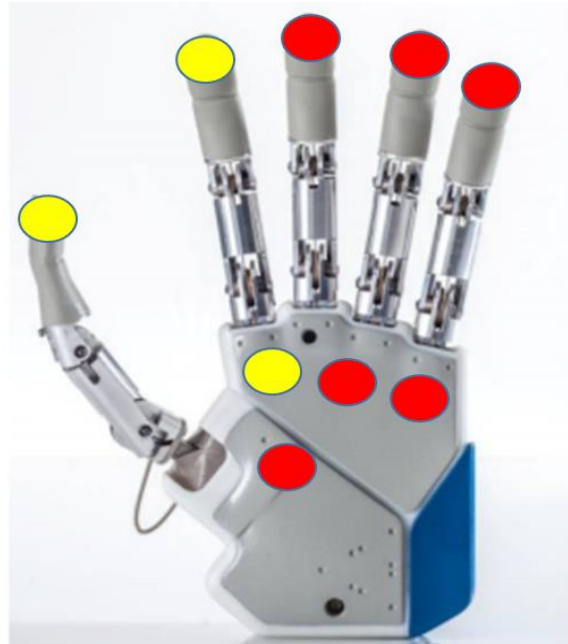


Figure 3.4. Selected sensorized points. The yellow ones are provided with an FSR sensor whose output will be used for both force estimation and slip detection.

The slip sensors have been positioned as indicated in consequence of the fact that thumb and index fingers are always involved in all the grasp types that IH2 hand is able to perform (e.g., bipod and tripod grasp). The integration of a slip sensor on the palm allows the power grasp to be performed in a more reliable way, even if the two slip sensors on thumb and index fingertips could be enough in terms of slip prevention. By means of a novel algorithm, which will be presented in Chapter 4, a single sensitive unite is sufficient for performing both force measurement and slip detection. Indeed, the above said algorithm allows extracting, from a single FSR output, an ON/OFF signal relating to the presence of slip events, besides being converted into a continuous sequence of force values. This peculiarity permits to carry out slip detection and force estimation in parallel, making the prosthesis control faster.

Palmar sensors can be three instead of four (i.e., less than one per every MCP joint) thanks to the large active area of the FSR 402 model.

3.4 Sensory system: integration in the IH2 hand

The FSR sensors had to be integrated in the prosthetic hand in order to be usable as tactile sensor. The IH2, which is a five-fingered anthropomorphic hand with five intrinsic electrical motors, includes basic sensors such as (5) motor encoders, (5) motor current sensors and (10) proximity sensors. Nevertheless, it does not feature any tactile sensor nor any venue for lodging them in a stable and reliable way. Thus, ad hoc new parts have been designed so as to substitute the existing ones; the new parts embedded the FSR sensors within them. CAD software SolidWorks has been adopted for the parts design, which have subsequently been fabricated by means of high resolution 3-D printers. The electronics for the sensors output collection has been designed, through the Eagle CAD software, and printed in the form of PCB.

3.4.1 CAD design: mechanical parts

The IH2 parts that have been redesigned in order to embed the tactile sensors have been the following:

- fingertips;
- palmar cover.

Different fingertip versions have been conceived: in this work, only the last (and definitive) one will be shown. The fingertip has been designed with the size of the FSR 402 sensor; an inner solid (*bone*) structure, on which to mount the sensor, has been covered with a silicon encapsulation obtained through an ad hoc designed mold. In this way, the sensor is totally covered with silicon, which is resistant and rather soft material at the same time, allowing the fingertip to convey the applied force all onto the sensor sensitive area. A hole has been

designed at the base of the bone, permitting the cables soldered to the sensors tabs to run within the structure and to be placed on the back of the fingertip; therefore, no obstruction from cables or other disturbance is present between the anterior face of the fingertip and the grasped object. Figure 3.5 shows some CAD images of the designed fingertip. Each finger has two phalanxes: the proximal phalanx (the closest to the palm) is made of aluminum whereas the distal phalanx (that includes the fingertip) is made of rubber. The designed fingertips have replaced the latter. A calibration procedure has been carried out for the fingertips mounted on the IH2, as described in Subsection 2.3.3.

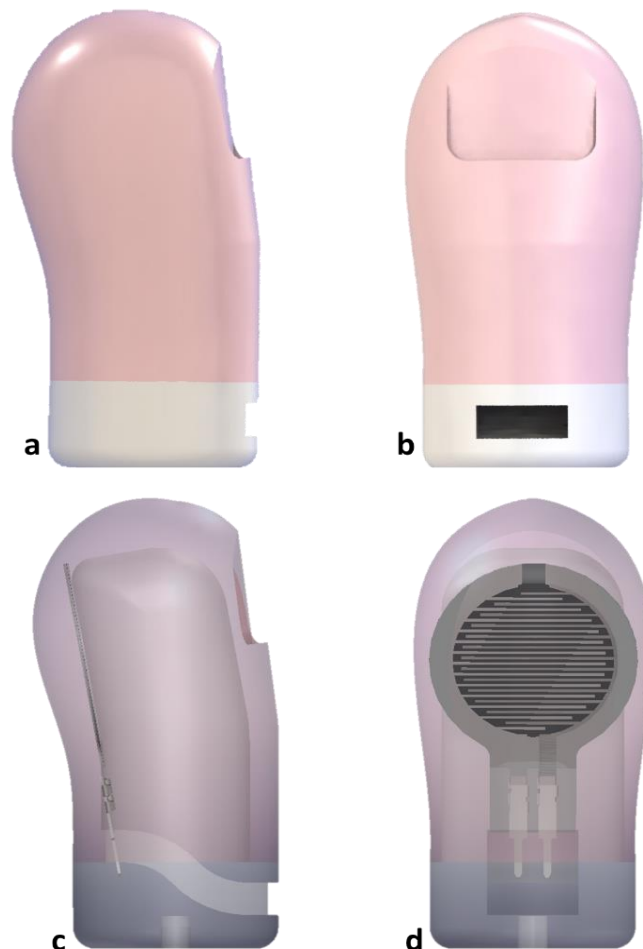


Figure 3.5. CAD images of the fingertip: lateral view (a, c); rear view (b); front view (d). The bone, the sensor and the hole for the cables to be connected to the sensor can be noticed in the transparent view (c, d). Cables are not represented in these figures.

Figure 3.6a shows the hand with all the five sensorized fingertips, while Figure 3.6b shows the hand executing a power grasp with a plastic cup. The silicon encapsulation, as well as the 3-D printing of the bones, has been fabricated at Centro Protesi INAIL, Vigorso di Budrio (BO), Italy.

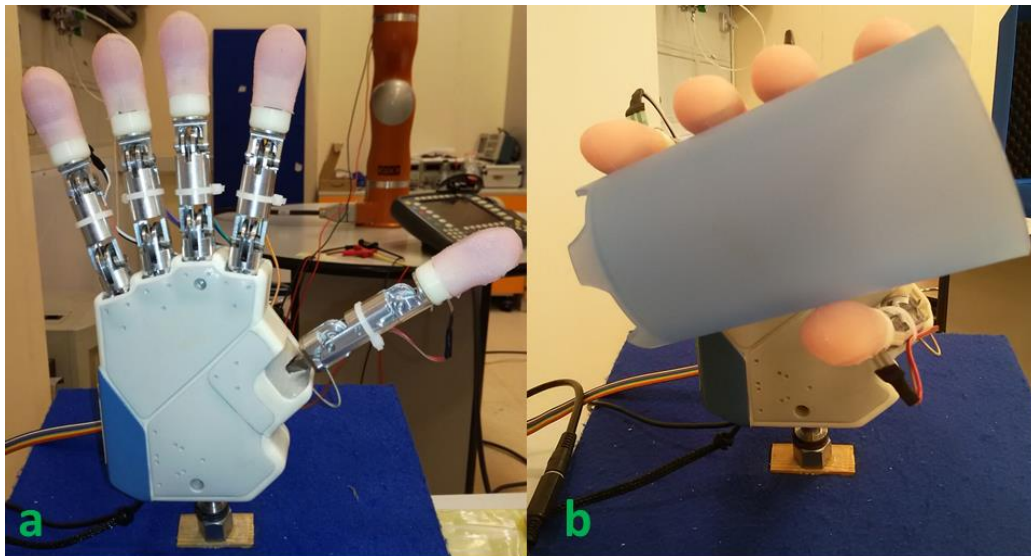


Figure 3.6. The hand with the designed fingertips (a); the hand grasping a plastic cup (b).

According to the chosen sensorized areas, the palm has been purposely designed to host the tactile and slippage sensors. Its surface has been designed with some circular extrusion, one per sensor, which in turn are included in a broader extruded cut. This cut has a particular shape that allows it to extend all the palm sensorized areas; it has been covered with a silicon piece obtained again by means of an ad hoc designed mold. Small holes permit the solder tabs of the FSRs to pass beneath the cover, removing thus the cables encumbrance and giving way to a clear surface on the palm. Figure 3.7 shows the designed palmar cover. A kind of tunnel can be noticed in Figure 3.7b: its function is that of collecting all the sensors cables, driving them outside the palm structure.

Figure 3.8 contains the whole hand with all the new mechanical parts.

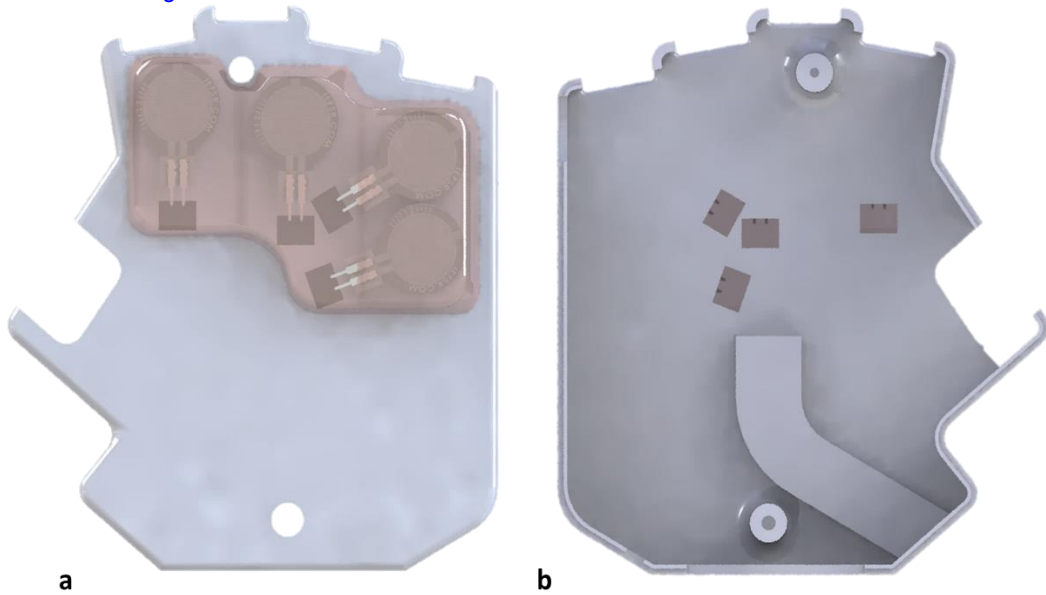


Figure 3.7. CAD images of the new palmar cover. Front view (a); rear view (b).

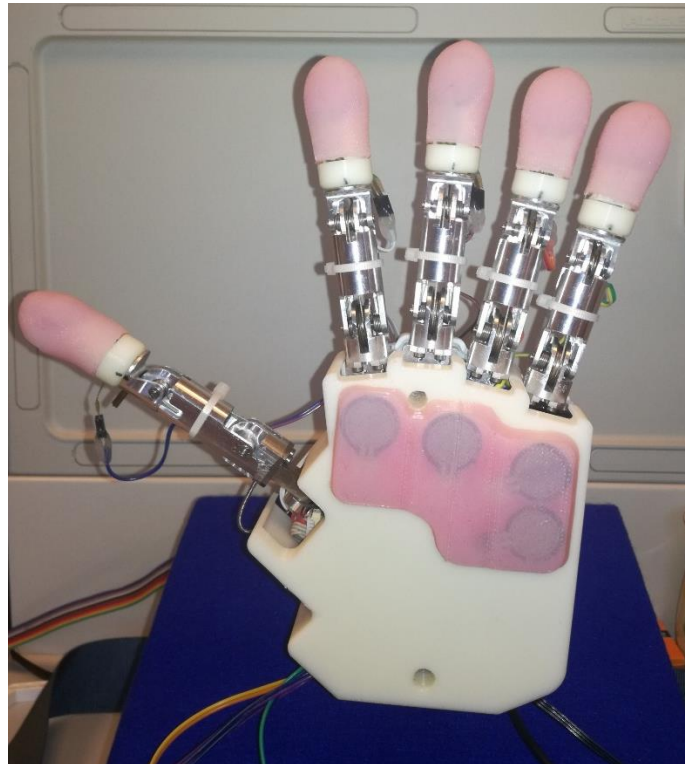


Figure 3.8. IH2 hand with sensorized fingertips and palm.

3.4.2. Sensors data acquisition

The system for the data exchange between the IH2 hand and a computer, including the force and slip sensors output acquisition, is depicted in Figure 3.9. A computer communicates with the IH2 hand,

sending commands through an asynchronous serial protocol (RS-232).

The force signals exerted by the FSR sensors are collected by a dedicated PCB, which features:

- ten force processing stages (Wheatstone Bridge plus amplification) as shown in Figure 2.10. For the moment, given that nine FSRs have been mounted on the prosthetic hand, only nine force stages are employed;
- three slip stages (as already declared, slip detection algorithm will be described in Chapter 4).

All the force and slip information outputted from the PCB are gathered by a NI-DAQ 6210, which close the loops sending the data to the computer.

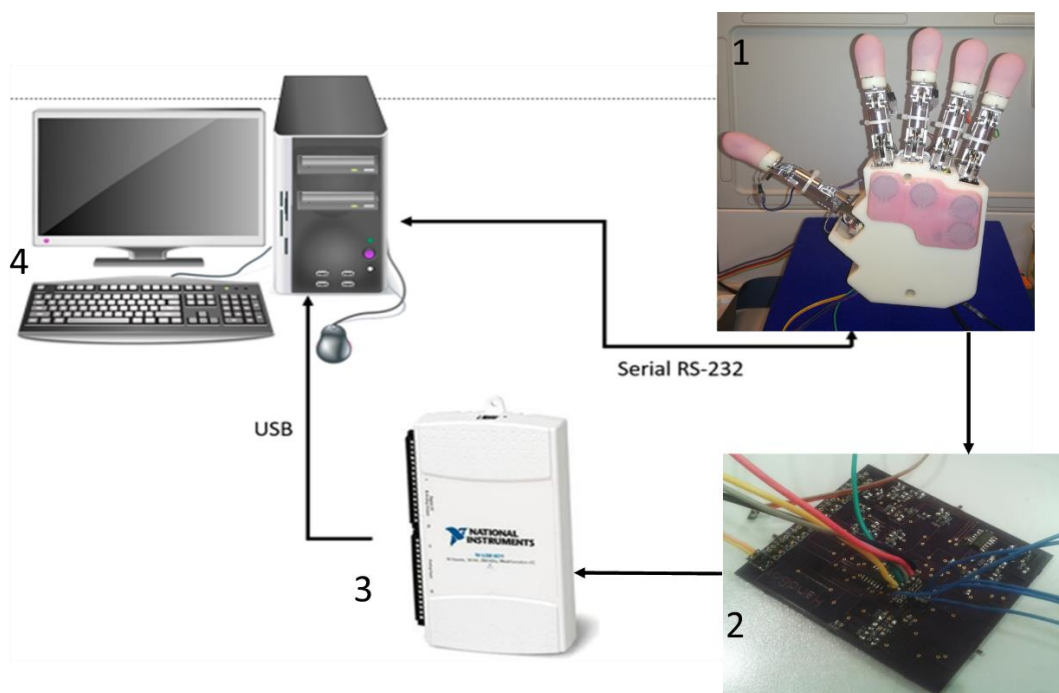


Figure 3.9. Communication chain between the IH2 and the computer. 1) IH2 hand with tactile sensors; 2) PCB for sensory analog pre-processing; 3) NI-DAQ 6210 for data acquisition; 4) PC.

The PCB has been designed and printed with only SMD components, in order to minimize its dimensions, achieving a 7cm x 8cm layout. In

this sense, a package as small as 0508 has been adopted for the SMD components. Given that ten force processing stages have been built on it, plus additional six needed for the three slip stages, four operational amplifiers have been soldered there, as every TL074 disposes of four amplification stages. Figure 3.10 shows the top layer of the PCB. A more compact version of the PCB (5cm x 5cm) has been designed but not printed yet.



Figure 3.10. PCB used for analog pre-processing of force and slip signals (top layer).

The developed sensory system proved to reliably measure the applied forces. Several grasps have been performed by the prosthetic hand with different objects such as the ones listed in Subsection 3.2.2. The designed fingertips and the placement of the sensor within them seem to adequately fit the grasped objects, as the measured force levels appear to be correct. Examples are given in Figure 3.11 and 3.12, relating to a bipod and to a tripod grasp, respectively. The thumb force, whose orientation is always opposed to the other fingers in the adopted

configuration, must compensate not only for the object weight, but also for the forces the opposing fingers apply. As a consequence, the thumb force value is reasonably higher than the others involved in the grasps, following the same logic introduced in Subection 2.4.3 of Chapter 2.

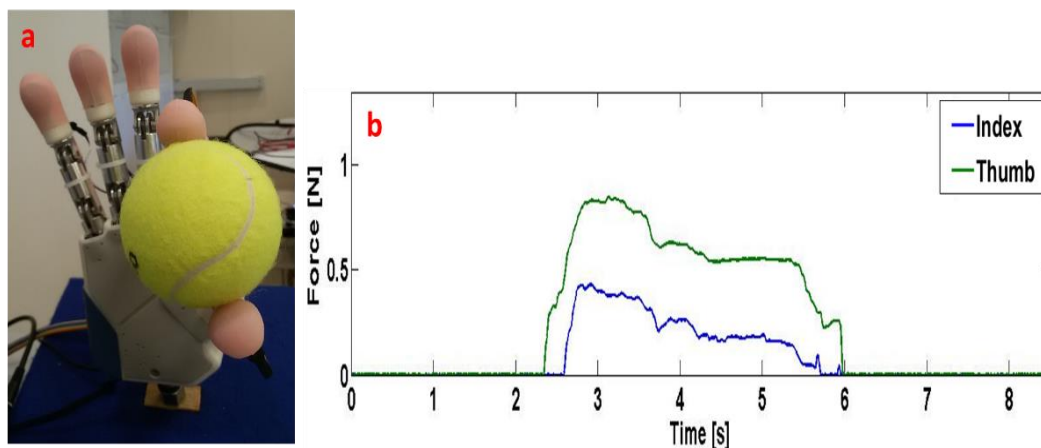


Figure 3.11. A bipod grasp trial performed by the IH2 hand with the new fingertips. IH2 grasping a tennis ball (a); recorded force values (b).

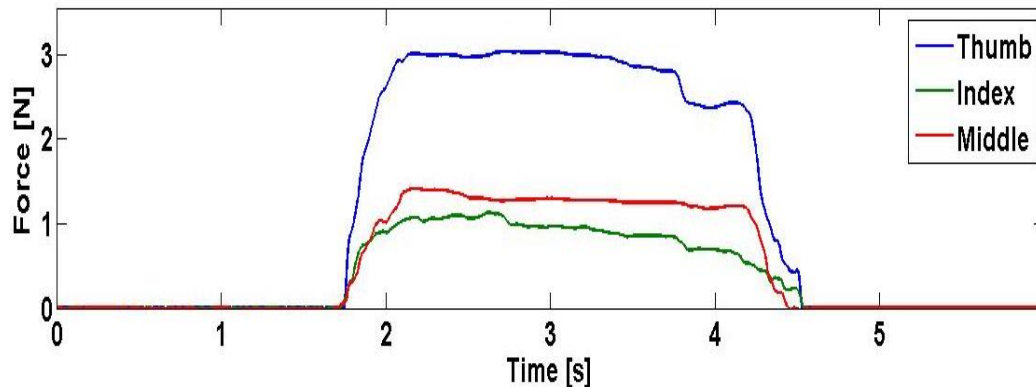


Figure 3.12. Recorded forces of a tripod grasp task performed by the IH2 with a plastic cup (as the one in Figure 3.6b).

The IH2 Hand, sensorized as described in this Chapter, has been used in the final experimentation of the PPR2 Project, funded by INAIL. The experimentation has terminated in the middle of June 2017; results have not been disseminated in scientific literature yet, and are thus not divulgeable through the present document.

3.5 Optimal sensors positioning

In this Section, a theoretical method for positioning the units of an array of tactile sensors is briefly presented. Its complete description is contained in Patent application #1. The method aims at obtaining a hyper spatial acuity during dynamic touch activities. Let us assume that the tactile array is stimulated at constant speed v by means of a periodic ridged surface (*grating*) characterized by a given pace Δp , and that $\Delta X_{i,j} > 0$ is the distance between the i^{th} and j^{th} sensor units of the tactile array.

Under such conditions, the frequency $f > 0$ of the output signal will be equal to $\frac{v}{\Delta p}$ for all sensor, as already observed. Specifically, the sensor output $u_i(t)$, which will be periodic as well, is supposed to have the following form:

$$u_i(t) = g_i(2\pi f t + \varphi_i) \quad (3.1)$$

where g_i is a generic function, t is the time and φ_i is the phase. The last quantity, for each sensor output, can be expressed as a function of $\Delta X_{i,j}$ and Δp . Mathematically, one has:

$$\Delta\varphi_{i,j} = \varphi_i - \varphi_j = -2\pi f \Delta t_{i,j} = -2\pi \frac{v}{\Delta p} \frac{\Delta X_{i,j}}{v} = -2\pi \frac{\Delta X_{i,j}}{\Delta p} \quad (3.2)$$

where $\Delta t_{i,j}$ is the time required to a chosen point of the grating for moving from the i^{th} to the j^{th} sensor units, choosing as a positive position reference frame the one having the versor going from the j^{th} to the i^{th} sensor unit. Hence, $\varphi_i > \varphi_j$ for $i < j$ if the grating moves from the j^{th} to the i^{th} sensor unit (positive velocity, resulting in $\Delta p > 0$, for the chosen convention), and that $\varphi_i < \varphi_j$ for $i < j$ if the grating moves from the i^{th} to the j^{th} sensor unit (negative velocity, resulting in $\Delta p < 0$, for the chosen convention).

If the phase differences between two sensing units could be measured, Equation 3.2 can be written as follows:

$$\Delta p = -2\pi \frac{\Delta X_{i,j}}{\Delta \varphi_{i,j}} \quad (3.3)$$

It must be noted that Equations (3.3) cannot be solved in general conditions with two sensors only. In fact, phase φ_i can be only estimated in terms of modulo 2π measurements $\check{\varphi}_i$, i.e.:

$$\check{\varphi}_i = \varphi_i |_{2\pi} \in [0, 2\pi) \quad (3.4)$$

which is the remainder of the division by 2π . As a consequence:

$$\widetilde{\Delta \varphi_{i,j}} = \varphi_i |_{2\pi} - \varphi_j |_{2\pi} \in (-2\pi, 2\pi). \quad (3.5)$$

Thus, at least three sensing units are required, as depicted in Figure 3.13 (where four units, named S1...S4, are shown. Assuming a positive velocity of the grating, and solving for $i, j = 1 \dots 3$ the system given by joining Equations (3.3) and (3.5) together, it results in:

$$\begin{aligned} \varphi_1 &= \check{\varphi}_1 + k2\pi \\ \varphi_2 &= \check{\varphi}_2 + h2\pi \\ \varphi_3 &= \check{\varphi}_3 + m2\pi \end{aligned} \quad (3.6)$$

with $k, h, m \in \mathbb{Z}$.

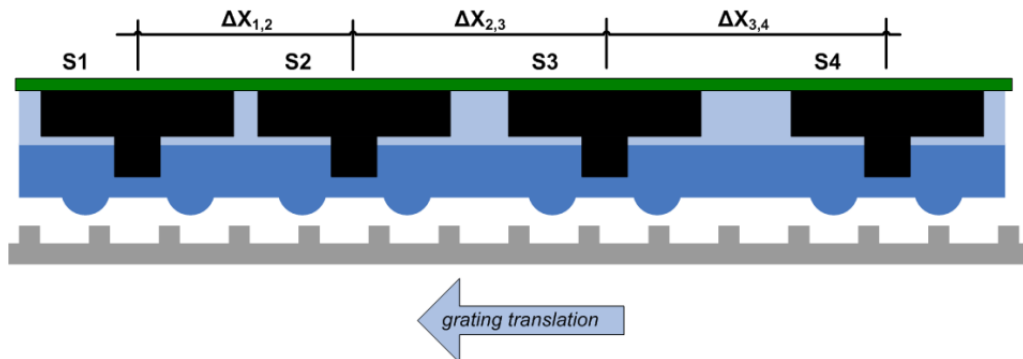


Figure 3.13. Positioning of sensors in line with non-constant distances one to the other.

Thus:

$$\begin{cases} \bar{\varphi}_1 - \bar{\varphi}_3 + (k - m)2\pi = 2\pi \frac{\Delta X_{1,3}}{\Delta p} \\ \bar{\varphi}_1 - \bar{\varphi}_2 + (k - h)2\pi = 2\pi \frac{\Delta X_{1,2}}{\Delta p} \\ \bar{\varphi}_2 - \bar{\varphi}_3 + (h - m)2\pi = 2\pi \frac{\Delta X_{2,3}}{\Delta p} \end{cases} \quad (3.7)$$

The parameter h can be neglected without loss of generality, as it simply operates a translation of the time reference frame. Besides, one can easily note that $\Delta X_{1,3} = \Delta X_{1,2} + \Delta X_{2,3}$; it allows discarding of the first row of (3.7), being a linear combination of the other two. This way, Equation (3.7) becomes:

$$\begin{cases} \bar{\varphi}_1 - \bar{\varphi}_2 + k2\pi = 2\pi \frac{\Delta X_{1,2}}{\Delta p} \\ \bar{\varphi}_2 - \bar{\varphi}_3 - m2\pi = 2\pi \frac{\Delta X_{2,3}}{\Delta p} \end{cases} \quad (3.8)$$

in which $\bar{\varphi}_i$ are measures, k and m are parameters, $\Delta X_{i,j}$ is known by the sensor design and Δp is the quantity to be measured, i.e. the spatial period of the grating. Finally, (3.9) can be expressed as:

$$\begin{cases} \Delta p = \Delta p_{1,2}(k) = 2\pi \frac{\Delta X_{1,2}}{\bar{\varphi}_1 - \bar{\varphi}_2 + k2\pi} \\ \Delta p = \Delta p_{2,3}(m) = 2\pi \frac{\Delta X_{2,3}}{\bar{\varphi}_2 - \bar{\varphi}_3 - m2\pi} \\ \bar{\varphi}_1 + k2\pi > \bar{\varphi}_2 > \bar{\varphi}_3 + m2\pi \\ \Delta p > 0 \\ k, m \in \mathbb{Z} \\ v = f\Delta p > 0 \end{cases} \quad (3.9)$$

At this point, it is possible to demonstrate that if $\frac{\Delta X_{1,2}}{\Delta X_{2,3}} \in \{\mathbb{R} - \mathbb{Q}\}$ (i.e., such ratio is irrational), Equation (3.10) has a unique solution which is the actual Δp used for the stimulation, even removing the limiting conditions $\Delta p > 0$ and $v = f\Delta p > 0$.

Numerical examples are provided in Figure 3.14 and Figure 3.15. Solutions of Equation 3.9, parametrized with respect to k , are

represented by red dots, while the blue cross is the recognized Δp , i.e. the first allowed solution depending on the introduced a priori knowledge, and the green line is the actual Δp . From the plots, one can observe that when the $\Delta X_{1,2} = \Delta X_{2,3} = \Delta X$, infinite solutions subsist, even if the recognized Δp coincides with the actual Δp . To increase the spatial resolution of the tactile sensor with respect to ΔX , the optimum sensors positioning should foresee different distances between each couple of units. The best theoretical way is to allocate them at distances which are related by irrational ratios.

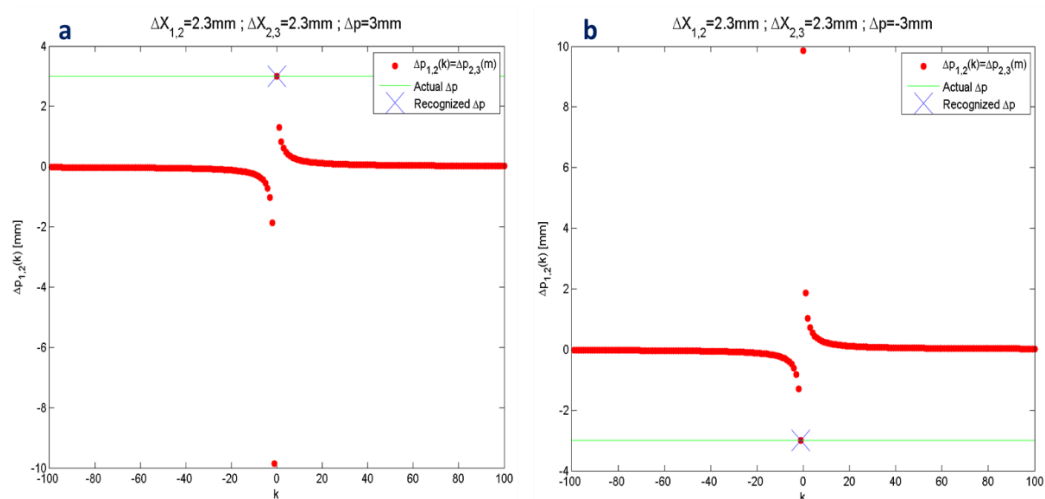


Figure 3.14. Sign(Δp) a priori known. $\Delta X_{1,2} = \Delta X_{2,3} = \Delta X = 2.3 < |\Delta p = 3|$. $\Delta p = 3$ mm (a); $\Delta p = -3$ mm (b). All quantities are expressed in mm.

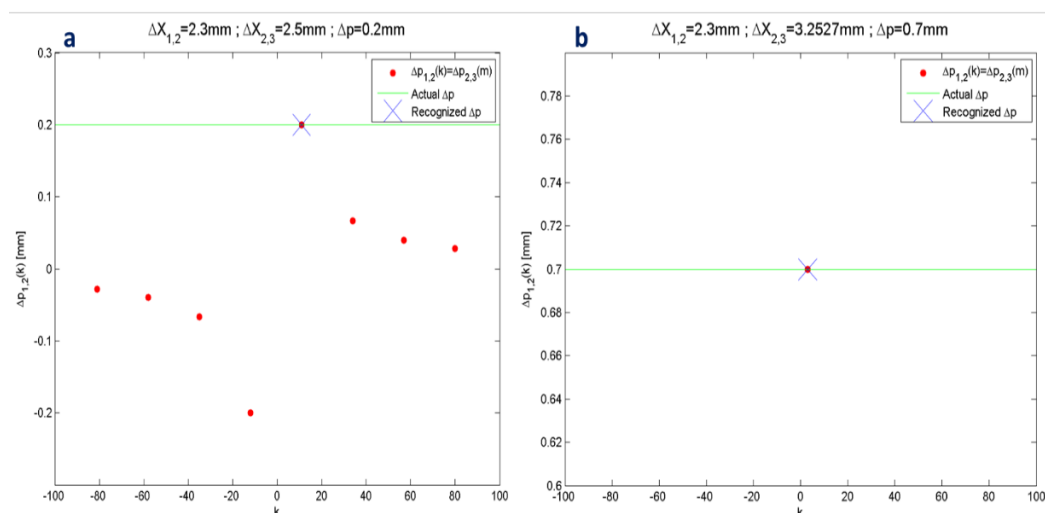


Figure 3.15. Sign(Δp) a priori known. $\Delta X_{1,2} = 2.3$, $\Delta X_{2,3} = 2.5$, $\Delta p = 0.2$ (a); $\Delta X_{1,2} = 2.3$, $\Delta X_{2,3} = 2.3\sqrt{2}$, $\Delta p = 0.7$ (b). All quantities are expressed in mm.

The shown results do not take into account the presence of noise in the experimental data. In spite of this, a rigorous analysis cannot neglect experimental errors affecting the measurements. In particular, considering Equation (3.8) and Equation (3.9), the phase measurements $\Delta\varphi_i$ can be affected by measurement errors in Δp and/or ΔX_{ij} . For this reason, an additive noise has been simulated in order to affect the quantities involved in the computation of sensor output phases. The noise has been modelled as gaussian, therefore with a zero mean normal probability distribution, and with a constant frequency spectrum (hence, white). Figure 3.16 shows an example effect of the noise that was added to the actual Δp (ADP) in the simulated [0.05 - 2.5] mm range. In every simulation, this range has been explored in steps of 0.01 mm, therefore accounting for 246 ADP values. Besides, 500 iterations have been performed for every ADP, generating this way $N=246 \times 500=123000$ iterations for each simulation.

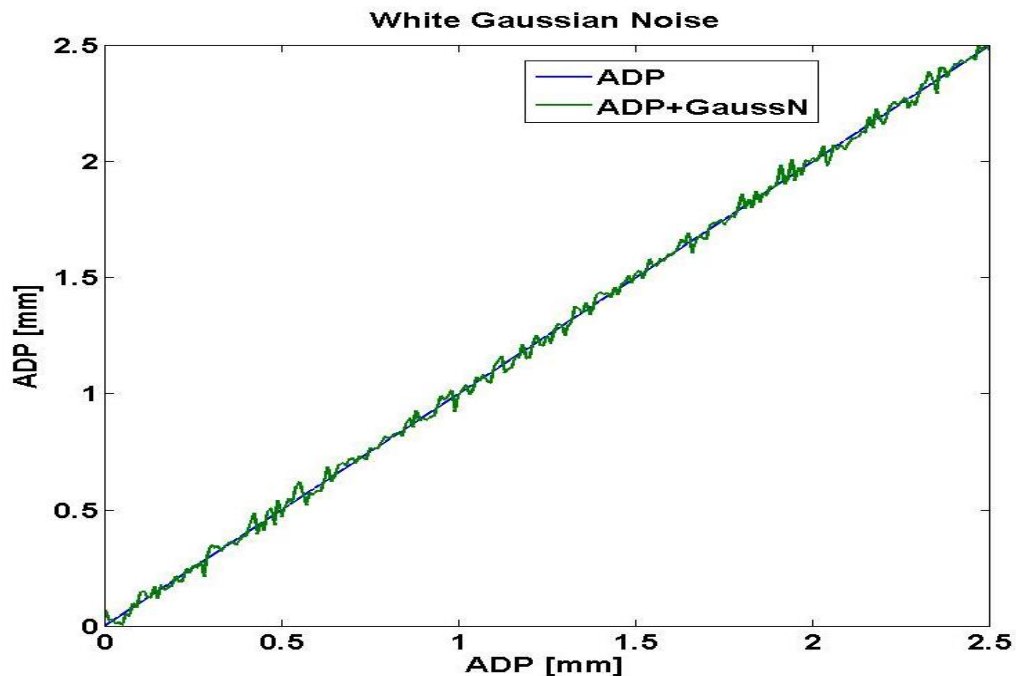


Figure 3.16. Values of the simulated ADP (blue ramp) ranging from 0.05 mm to 2.5 mm with steps of 0.01 mm, and of ADP with additive white gaussian noise (green plot).

The *Montecarlo* method has been employed for performing the simulations: random noise values were automatically extracted from the Gaussian distribution at each iteration and added to the quantities to be perturbed. The chosen signal to noise (S/N) ratio has been 35 dB. Figure 3.17 illustrates the ADPs are plotted versus the error modulus, computed by dividing each error by the maximum error value found during a given simulation. The error is simply the difference between the recognized Δp and the actual Δp .

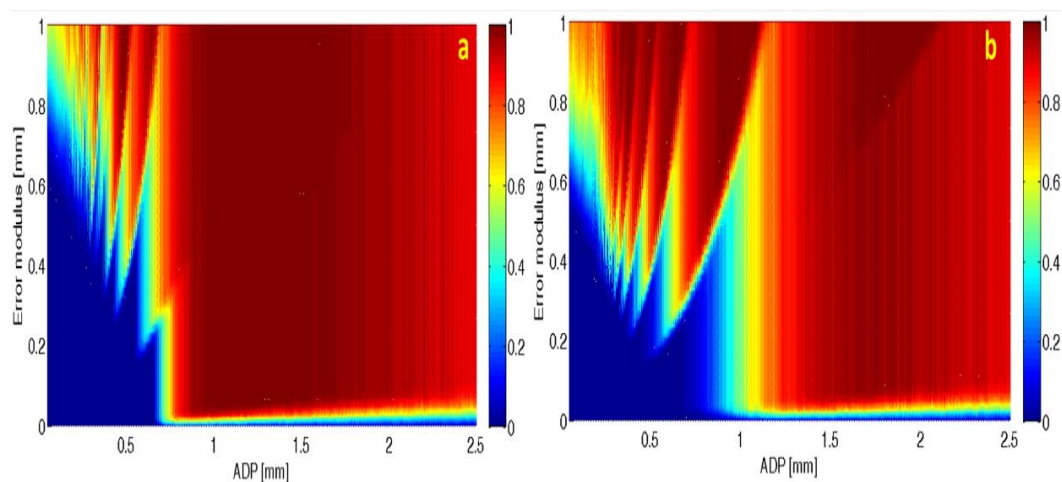


Figure 3.17. Error modulus versus the ADP values. $\Delta X_{1,2} = 2.3$, $\Delta X_{2,3} = 2.3\sqrt{2}$ (a); $\Delta X_{1,2} = 2.3$, $\Delta X_{2,3} = 2.5$ (b). All quantities are expressed in mm.

Higher quantities of errors can be noticed when the ratio between the two distances is rational. Significant errors are evident up to 1.1 mm for ADP, while when the ratio is irrational, the error decays much more before ADP=1 mm. These results, as well as similar ones not reported in this document for sake of brevity, suggest to look into an experimental validation of the presented method for optimum positioning of the sensitive units in a tactile array.

3.6 Conclusions

In this Chapter, the development of a tactile sensory system for the IH2 prosthetic hand has been shown. General criteria for the design of an

artificial tactile sensory system have been discussed, and then the choice of the sensors to be used for the prosthesis sensorization has been presented according to such criteria. Some of the sensors characteristics have already been illustrated in Chapter 2, as well as the schematic for the sensor output conditioning and the static calibration procedure.

CAD parts have been designed ex novo for the IH2 hand, as the original ones does not embed tactile sensors of any kind. The mechanical parts that have been redesigned have been the fingertips and the hand palmar cover, allowing now the stable placement of tactile sensors within them. All the new mechanical parts have been interfaced with silicon encapsulations/covers which convey the applied force onto the sensitive area of the sensors themselves and protect them from scratching or damaging in general.

Ad hoc electronics has been conceived for the data elaboration; both force and slippage signals have been processed by a dedicated PCB which has been purposely printed. The PCB is composed of ten force stages and three slip stages. Then, the PCB outputs are collected by a NI-DAQ 6210 and sent to a computer.

Moreover, a theoretical method for the optimum positioning of the sensitive units in a tactile array has been presented. Such a method allows a tactile sensor array to achieve hyper spatial acuity when stimulated with a periodic ridged surface at constant velocity. Experimental validation has not been provided yet, although the method performance appears promising with both uncorrupted and noise-corrupted data.

In the present Chapter, the first step towards the utilization of a tactile sensory system on a hand prosthesis has been made. The IH2 hand, sensorized as described in this Chapter, has been worn by an amputee

subject in an experimentation aiming at the restoration of tactile feedback thanks to neural stimulation. The aim of the experimentation has been to put the amputee in condition to *sense* the grasped objects like the prosthesis is his own natural hand. Due to legal restrictions, all the collected data during the experimentation cannot be published yet in this document.

The following step is described in the next Chapter, where the slip detection algorithm is presented.

Tesi di dottorato in Bioingegneria e bioscienze, di Rocco Romeo,
discussa presso l'Università Campus Bio-Medico di Roma in data 16/10/2017.
La disseminazione e la riproduzione di questo documento sono consentite per scopi di didattica e ricerca,
a condizione che ne venga citata la fonte.

Chapter 4 Slippage detection algorithm

As already pointed out in the previous Chapter, tactile sensing is fundamental for enhancing the performance of an artificial manipulator. This is true for example referring to robotic hands, even more for prosthetic hands. Though, the current number of applications making use of tactile information is quite limited (Kappassov, 2015).

In human sense of touch, of crucial importance is the ability to properly detect the slippage phenomena that may occur during manipulation and grasp. As already described, the human skin is provided, among the other things, with specialized mechanoreceptors (FA I and SA I (Herrera, 2007)) which are able to send the brain signals generated by slip events. In order to mimic this physiological feature, artificial tactile sensing must pay special attention to the question of the slip detection. Robotic hands should be able to control slip events in a dexterous manner, avoiding the damage of the object as well as grasp instability. Commonly, while the robot performs an action unforeseen events might occur, hindering the success of the action itself. This situation results particularly problematic when the action involves the manipulation of an object; the availability of control strategies relying on tactile data could greatly improve the robot ability when facing such a situation. In this contest, a reliable slip detection algorithm would be of great help.

In this Chapter, a new method for detecting slippage is proposed (Patent application #2); it makes use of just one input signal (e.g., the normal force) measured through a resistive sensor, leading to an ON/OFF slip information. Simple operations such as digital or analog filtering, rectification and envelope of the input signal, are cascaded in order to generate the ON/OFF signal, which can easily be integrated in a closed-loop control algorithm. Validation procedures will be illustrated for a

variety of resistive sensors; the potential of the method will be confirmed by also reporting the results of an online application in the control of a prosthetic hand.

Part of the content of this Chapter can be found in (Romeo, 2017b) and in (Barone, 2016), concerning the contributions given by the author of the present thesis to such works.

4.1 Slip detection: from classical approaches to the proposed one

The literature proposes plenty of tactile sensors and procedures for slippage detection; despite of it, to reproduce onto an artificial system all the characteristics of the complex human tactile sensing system, with its four different types of mechanoreceptors, remains hard. In tactile sensing applications, one of the main issues resides in the difficult integration of static (force/pressure measurement) and dynamic (slip detection) information. Moreover, it must be pointed out that slip sensors employed in other fields such as automotive (e.g. in anti-lock braking systems-ABS) and generally in industrial robotics are commonly not suitable for prosthetics (Nicholls, 1999). Therefore, attention of researchers has moved towards additional strategies over the years, as witnessed by an increasing number of publications about this issue (Francomano, 2013).

4.1.1 Slip detection in prosthetics: state of the art

Being that artificial tactile sensors remain still far from reproducing natural mechanoreceptors capabilities (Chappell, 2011), it is rare to find a hand prosthesis with a tactile sensory system, and even rarer to include in such a system a dedicated information which is relevant to the slippage. As a consequence, prosthetic devices do not allow the wearer

to reliably control slip events; nonetheless, considerable effort has been produced since the last years of 1980s in order to integrate slip information in the prosthesis control system (Francomano, 2013).

The main approach, the most relevant until the end of last century by far, relies on the calculation of the static friction coefficient starting from normal and tangential forces measurement (Mingrino, 1994; De Maria, 2012). In this way, a multi-axial force sensor is required in order to measure forces along at least another axis apart from the normal one; alternatively, tangential forces have to be estimated, and the algorithms to do such an operation are often complex. Examples include Kalman filters (Wettels, 2009), as well as transformation into the frequency domain in order to extract useful slip information (Engeberg, 2013). Other methods take into account the variations relative to the position of the center of force distribution (Holweg, 1996) or to the center of pressure (Gunji, 2007), but it is quite common the use of DFT, PSD and FFT (Fernandez, 2014), resulting into a not negligible augmentation of the computational burden.

A tri-axial force sensor featuring a CMC (Carbon Micro-Coil) for slippage detection has been fabricated in (Kawamura, 2012). A widespread solution for obtaining a satisfactory tactile sensory system is to combine more sensing units, i.e., one for static information and one for dynamic one. Such solutions embed for instance, into a unique device, force sensors together with piezo-electric (such as PVDF or PZT) sensors for slip management (Yamada, 1994; Choi, 2005; Cotton, 2007). In other cases, the two different sensing units are kept separately (Rodriguez-Cheu, 2008). Moreover, the employment of accelerometers as slippage sensors has been demonstrated (Howe, 1989); to this end, they have been employed on instrumented objects for human and robot

grasp analysis (Romeo, 2015), and on robotic grippers as well (Abhinav, 2009).

In (Teshigawara, 2010), a slippage sensor based on conductive rubber has been proposed, which was able to detect slippage phenomena through the application of the Continuous Wavelet Transform to its output (electrical tension). However, the aforementioned sensor was not able to measure forces. Further methods exploit the derivative function of the normal component of the estimated force (Pasluosta, 2012), or else, the vibrations in a fluid sealed into the core of a biomimetic sensor (Fishel, 2012; Su, 2015). The latter is available on the market (BioTac by SynTouch); it is able, among other things, to provide fluid pressure measurement and a band-pass filtered signal of such pressure, in the range [10-1040] Hz, which should give indications about tangential forces, therefore about slip. Its cost is still rather high.

4.1.2 Slip detection: proposed approach

All the reported works demonstrate sensors and/or techniques for the detection of slippage, including sometimes forces estimation on one or more axes as well. However, it cannot be found in literature an example of tactile sensor that is able to measure forces as high as desired and to detect slippage events relying on just one axis information. In this paper, a new method for detection of slippage events is proposed; it makes use of just one input signal (e.g., the normal force) measured through a piezo-resistive sensor, leading to an ON/OFF slip information. Simple operations such as digital filtering, rectification and envelope of the input signal, are cascaded in order to generate the ON/OFF signal. The method has been preliminarily validated in (Barone, 2016), where, thanks to an online implementation, a robotic hand endowed with tactile mono-axial force sensors has been able to

successfully hold objects of various shapes and dimensions, avoiding slippage events automatically induced. Indeed, it is well known the difficulty of measuring slippage events starting only from normal force amplitude (Van Ho, 2014); by applying the proposed method to the voltage output of a simple, low cost mono-axial sensor (i.e., normal axis), it is possible to obtain information about slippage along with the force information itself. Furthermore, the method application on the output of resistive tri-axial force sensors will be shown, extending its application to multi-axial sensors. Indeed, the method can be easily applied on every type of resistive sensors, regardless the number of force axes: one axis is enough, though more can be considered whenever available.

Ad hoc experimental setups have been created for the different resistive sensors typologies employed, with the aim of validating the method from an as general as possible perspective. Slippage condition has been induced automatically, by sliding the surface in contact with the sensors or vice versa.

In the following subsections, both software and hardware implementations will be presented. The former has been developed in the Matlab environment, while for the latter an ad hoc PCB has been created.

4.2 Slip detection procedure

The method (Patent application #2) for slip detection described in this work has been applied to various resistive sensors. In particular, a resistive sensor can be modeled as a varying electrical resistance; the variation of the resistance, which is inversely proportional to the applied force, is easily translatable into a voltage by means of opportune analog electronics. The so obtained voltage has to be converted into force

through a mathematical law which allows the passage from electrical tension to mechanical tension. In this paper, the electrical voltage has served as input for the proposed algorithm. Though, using the estimated force leads to equivalent results, as its trend and variations are the same. A description of the employed resistive sensors, with respect to the peculiar technologies, will be given in the next Subsection.

The method consists of three main blocks, which are put in cascade. Single axis information is enough for estimating applied force and for detecting slip events. This is possible thanks to the idea that the force signal (i.e., the voltage), which is characterized by high amplitude and low frequencies, carries a higher frequency content when the sensor is slid over a surface, or vice-versa. Such content can be extracted by means of adequate filtering operations. At this point, a low amplitude, high frequency signal is generated; the presence of dense fluctuations indicates that the relative movement is happening between the object and the sensor. The low frequency due to application of load are filtered out from the voltage signal, privileging the faster variations produced by slip. The filtering operation is followed by a rectification of the signal, which is in turn followed by an enveloping phase. An ON/OFF signal relative to the onset of a slippage event is then generated. The algorithm blocks are described in detail below; a block scheme of the whole algorithm is depicted in Figure 4.1.

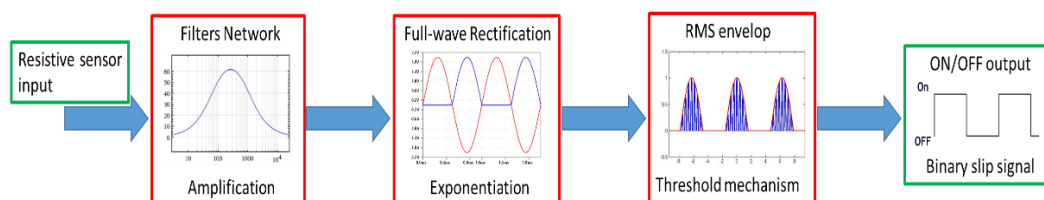


Figure 4.1. Overview of the slip detection algorithm represented by blocks.

4.2.1 Block 1 – Filter network

The filtering operations are responsible for the high frequencies extraction from the force signal. Thus, it is crucial to properly dimension the filter parameters in order to obtain the highest performance. A band-pass configuration has been chosen for controlling the whole bandwidth, though a high-pass filter could have also been adopted. Indeed, the first thing to do is the low frequencies removal: this can be done by fixing an adequate low cut-off frequency f_{col} . Then, the high cut-off frequency f_{coh} must be set; the frequencies choice, delimitating the meaningful bandwidth, depends on the resistive sensor technology and structure. Details about this aspect will be provided later.

More specifically, IIR *causal* filters have been designed. IIR type filters have the advantage of needing a minor computational burden than the FIR type, while the causality is fundamental for a real-time implementation. Indeed, non-causal filters feature a zero-phase response, which is highly desirable for avoiding distortion and any kind of delay in the filter output. Such conditions are not feasible for real filters, as a delay is always present between input and output: i.e., such filter are nonzero-phase (or causal). A 4th-order Butterworth filter has been implemented, with a gain G_b equal to 100. Its transfer function $H_b(z)$ and the filtered output signal $Y(z)$, expressed in the z-domain, are given by:

$$H_b(z) = G_b \frac{\sum_{n=0}^N b_n z^{-n}}{\sum_{n=0}^M a_n z^{-n}}, \quad (4.1)$$

$$Y(z) = H_b(z) \cdot X(z), \quad (4.2)$$

where $N=M$, n is the filter order and $X(z)$ is the input resistive signal. Two additional digital 4th-order filters, i.e., elliptic filters, have been

cascaded to the Butterworth one. Their transfer functions $H_{e1}(z)$ and $H_{e2}(z)$ have the same form as in (1). The stop-band configuration has been chosen for them, as the intention was to clear every content outside the Butterworth filter range; details about the bandwidth limits, i.e. the cut-off frequencies choice, will be provided later. Gain G_{e1} and G_{e2} have been set to 1, while the pass-band ripple (peak to peak) and the stop-band attenuation have been set to 0.01 dB and 40 dB respectively. The reason for these choices resides in the necessity of achieving a flat response in the pass-band region, and a quick roll-off transition to the stop-band region. The response of the Butterworth filter is well known for its slower roll-off than other types of filters, e.g. elliptic ones. The latter can thus be of great help in achieving good attenuation of the frequencies close to the Butterworth band limits. In Figure 4.2, a general example of filtered signal is illustrated, together with the original unfiltered resistive signal (FSR sensor).

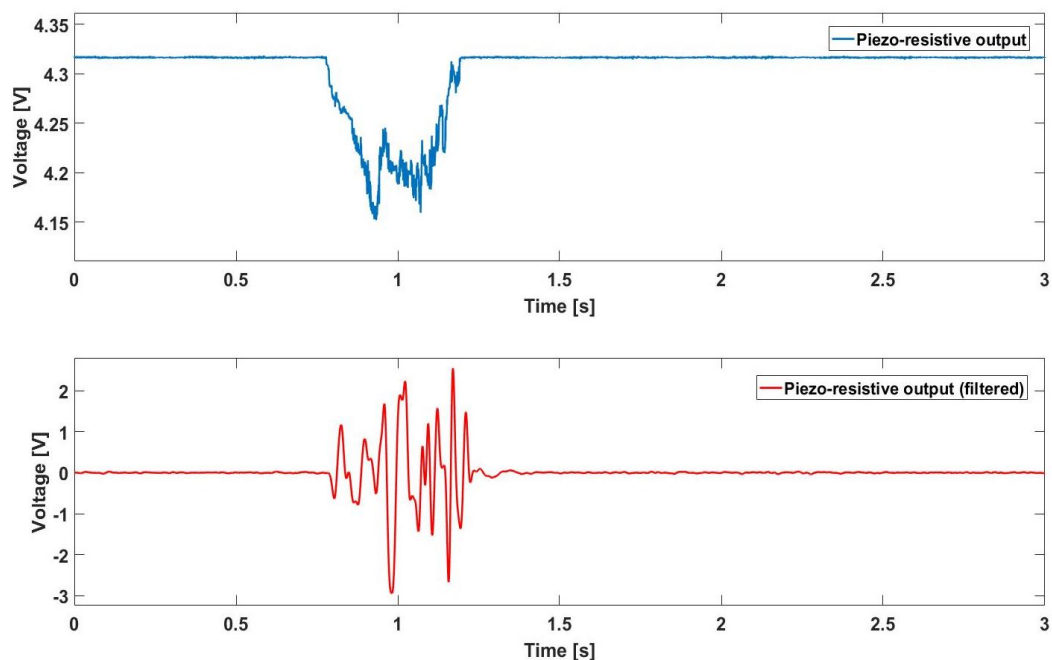


Figure 4.2. A resistive force sensor output (top) with the corresponding filtered signal (bottom). The resistive signal has been obtained by pressing and rubbing an FSR sensor onto an unknown roughness surface.

Clearly, the choice of high order filters, higher than three, is due to the necessity of achieving fast roll-off. In this way, frequency components outside the range of interest might be simpler to discard.

4.2.2 Block 2 – Rectification and exponentiation

The filtering stage provides a high frequency signal, yet characterized by a bipolar nature. The rectification can improve the capability of the signal to overcome a given threshold; Figure 4.3 exemplifies this concept. By converting the polarity of the negative spikes, the time window within which the signal can be ON (i.e., above threshold) can be longer than in the case of a bipolar signal. Thus, a full-wave rectification comes to be desirable. Anyway, at least a half-wave rectification, consisting in erasing one of the two polarities spikes, has to be executed; it is needed for allowing an easier accomplishment of the next operation (i.e., envelope). Nonetheless, the raising of the signal amplitude to the second or the third power helps to privilege the slip signal content with respect to the peaks due to contact and release phases. The latter can sometimes be present although the stop-band filters have a great impact on the signal. The filtered and rectified signal has been raised to the third power, and the whole process is described by the following mathematical function $H_{f+r}(z)$:

$$H_{f+r}(z) = |H_f|^3 = \sqrt[3]{H_f(z) \cdot H_f^*(z^*)}, \quad (4.3)$$

in which

$$H_f(z) = H_b(z) \cdot H_{e1}(z) \cdot H_{e2}(z), \quad (4.4)$$

i.e., $H_f(z)$ represents the transfer function of the overall filter network, comprised of the three filters described in Subsection 4.2.1. The filtered signal $Y(z)$, now rectified as well, becomes

$$Y_{f+r}(z) = |H_f|^3 \cdot X(z)^3 = \sqrt[3]{H_f(z) \cdot H_f^*(z^*) \cdot X(z)^3} \quad (4.5)$$

which can be expressed more compactly as follows:

$$Y_{f+r}(z) = |H_f|^3 \cdot X(z)^3 = \sqrt[3]{X(z)^2 \cdot H_f(z) \cdot H_f^*(z^*)} \quad (4.6)$$

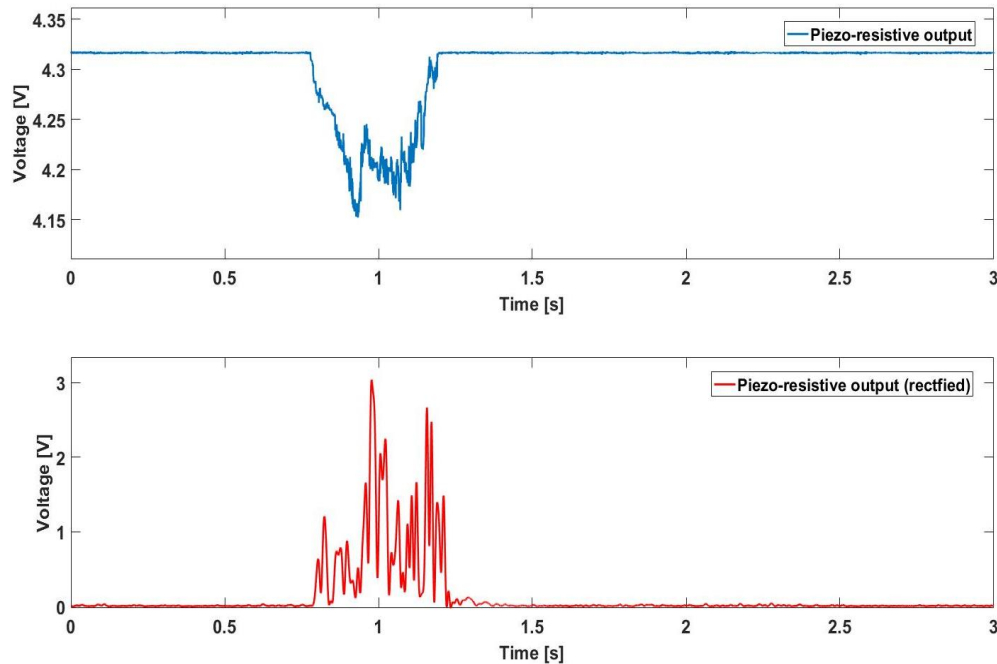


Figure 4.3. The signal of Figure 4.2 (top) with the corresponding filtered and fully rectified signal (bottom).

4.2.3. Block 3 – Envelope

Finally, the RMS of the signal is calculated, yielding its envelope. The RMS value ENV_{rms} is obtained through the following formula:

$$ENV_{rms} = \sqrt{\frac{1}{W} \sum_{r=w_1}^{w_2} x_r^2}, \quad (4.7)$$

where $W=W_2-W_1$, corresponding to the temporal width of the selected window, and x_r is a single sample included within W . It is interesting to notice that the rectified signal $Y_{r+f}(z)$ has been divided into a number of

windows with an equal width h ; every window W_i almost totally overlaps the adjacent one W_{i+1} , being computed as follows:

$$W_i = [Y_{r+f}(i), Y_{r+f}(i + 1) \dots Y_{r+f}(i + h)]$$
$$W_{i+1} = [Y_{r+f}(i + 1), Y_{r+f}(i + 2) \dots Y_{r+f}(i + h + 1)], \quad (4.8)$$

that is, the overlap is shifted by one sample from a window to the next. The envelope acts like a low pass filter; that is, it generates a continuous curve starting from the peaks of the rectified signal. Figure 4.4 gives an example of enveloped signal. At this point, the ON/OFF slip signal can be obtained with a threshold mechanism. More details about the time window chosen and the threshold mechanism will be provided in the following.

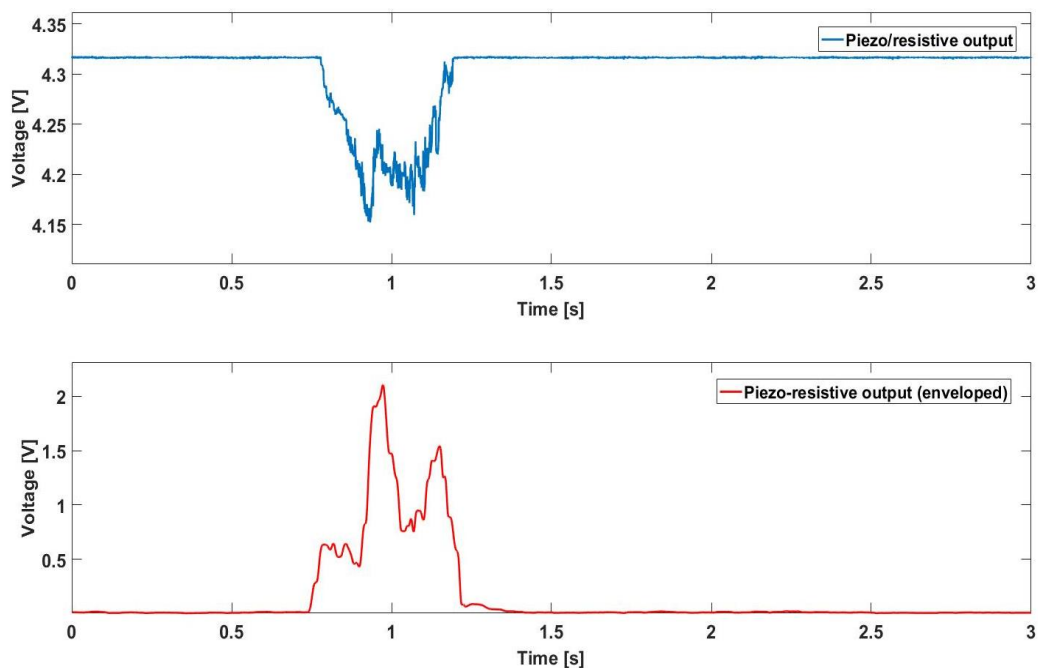


Figure 4.4. The same resistive signal (top) as in Figure 4.2 and Figure 4.3 with the corresponding filtered, fully rectified and enveloped signal (bottom).

4.3 Experimental setup

4.3.1 Sensors: brief description

As already stated, different typologies of resistive sensors have been employed for the validation of the proposed slip detection method. In particular, the tested technologies have been:

- microelectromechanical (MEMS) sensors;
- FSR sensors;
- strain gauge sensors

The first two typologies belong to the piezo-resistive category: although being resistive, they differ from the third typology in the way the electrical resistance varies as a consequence of the applied force. As far as regards resistive sensors, in fact, the mathematical definition of the electrical resistance R is given by:

$$R = \rho \frac{L}{A}; \quad (4.9)$$

now, by imposing a stress on a resistive material characterized by a resistivity ρ , a section A and a length L as depicted in Figure 4.5, the electrical resistance variation is written in the following manner:

$$dR = \frac{\rho}{A} dL + \frac{L}{A} d\rho - \frac{\rho L}{A^2} dA$$
$$\frac{dR}{R} = \frac{dL}{L} + \frac{d\rho}{\rho} - \frac{dA}{A} \quad (4.10)$$

Concerning piezo-resistive sensors, indeed, the main contribution to the resistance variation due to an applied stress is yielded by the resistivity term (i.e., $\frac{d\rho}{\rho}$), whereas in traditional strain gauge sensors the resistance variation is mainly characterized by the dimension terms $\frac{dL}{L}$ and $\frac{dA}{A}$.

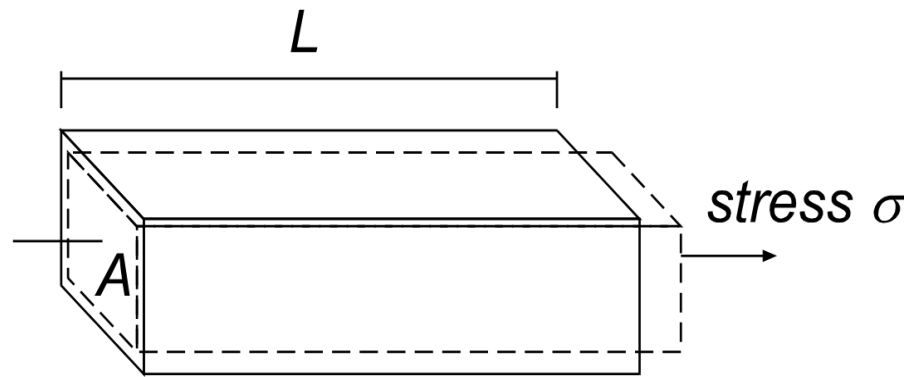


Figure 4.5. Resistive material undergoing a longitudinal stress.

The MEMS sensors have been fabricated at Scuola Superiore Sant'Anna, Pisa (Italy), and are composed of a 2×2 array of piezo-resistive tactile sensitive units. Each unit has 4 channels, thus resulting in a total amount of 16 channels in an area of 22.3 mm^2 , i.e. 72 units/cm^2 (Oddo, 2009a). From all the 16 channels, forces on all the three direction could be reconstructed though a calibration matrix. The tactile array has been integrated into a biomimetic fingertip, which in turn was integrated in the distal phalanx of a robotic finger. The outer packaging layer of the fingertip, which is made of synthetic compliant material (DragonSkin), had a surface with fingerprints (Figure 4.6a) mimicking the human fingerpad.

The FSR sensors were the same used for the sensorization of the IH2 hand (Chapter 3).

For what regards the strain gauge sensors, the [model 20E12A4](#) by JR3, Inc. (Figure 4.6c) has been employed. This is a six-axis force sensor as it allows measuring the force components on the three axes and the corresponding torques. Its shape is cylindrical, with a base diameter of 51 mm and a thickness of were 31.8 mm, weighting 135 g. Maximum measurable force reaches 80 N on the gravity direction, while it is equal to 40 N on the other two; such a sensor has a digital resolution of 0.01 N on the gravity direction, and of 0.005 on the other ones.

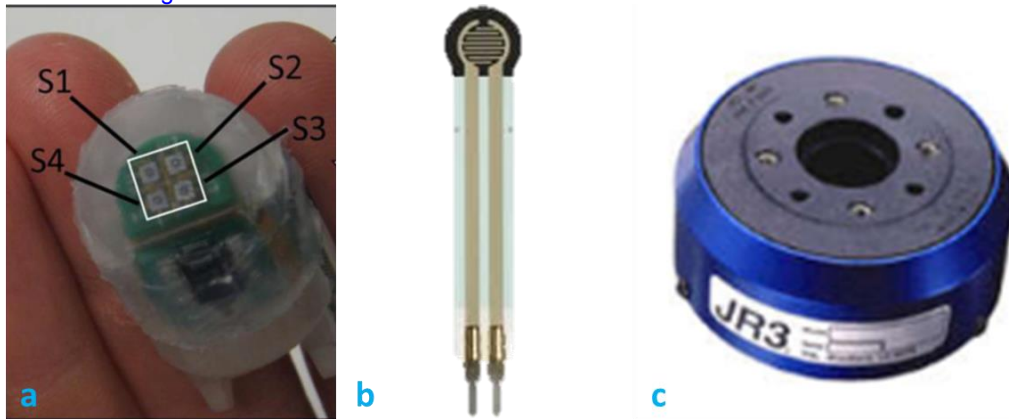


Figure 4.6. MEMS sensors (a); FSR sensors (b); strain gauge sensors (c).

4.3.2 Experimental protocol and set-ups

The experimental set-up used for testing the algorithm on the MEMS sensors consisted of two main subsystems, as shown in Figure 4.7: the sensorized robotic finger and a mechatronic platform under horizontal position/velocity control, which was a simplified version of a 2-DoF platform (Oddo, 2011b). Changeable gratings were housed in a carrier of the platform, so as to test different tactile stimuli: the Δp values have been 400 μm , 440 μm and 480 μm . Thirty trials have been executed, i.e. ten per each tactile stimulus. Each trial was configured in the following way: the finger was flexed and the fingertip brought into contact with the tactile stimulus (phases 1 and 2 of Figure 4.7a). A double-ramp sliding motion was then applied to the grating along the positive y-axis (phase 3a of Figure 4.7a) via the platform under position/velocity control: a 10-mm ramp for 1500 ms ($v_1 = 6.7$ mm/s) was followed by a 10-mm one in 1000 ms ($v_2 = 10.0$ mm/s). This protocol is named *passive touch* since the robotic finger is still during the stimulus-sliding motion (Oddo, 2011a). It represents slippage condition in a more accurate way than moving the finger with respect to the surface (*active touch*), given that when an object slides during a grasp, it is this one's surface which actually moves (i.e., the surface into contact with the finger).

On the other hand, the experimental set-up used for testing the method with the FSR sensors consisted of an FSR sensor placed on a plastic distal phalanx of the IH2 hand, which has purposely been removed from the robotic hand. They have been covered with a silicon cap (Figure 4.7b), simulating the prosthetic cover of a common prosthetic hand. The so obtained fingertip has been interfaced to a 7 DoF robot (namely KUKA-LWR 4+) by means of a thin, cylindrical plastic segment. The robot moved the fingertip itself upon the surface, releasing it after a sliding movement of 2 cm. Thus, the phases shown in Figure 4.7a are the same for the FSR set-up as well, with the exception of 3a which is this time active, not passive. Three trials per each tested surface have been performed with the FSR sensors. The latter have been the same surfaces as shown in Chapter 2 concerning the instrumented objects. Of the three trials per surface, one has been executed with a velocity equal to 2 cm/s, one with a velocity of 4 cm/s, and the last one with 8 cm/s.

Finally, the JR3 sensors have been moved through a linear actuator (velocity: 4 cm/s) on the same surfaces used for the FSR sensors, with the double purpose of confirming the possibility of implementing the method on tangential forces (beyond the normal one), and to obtain encouraging results on a resistive force sensor typology which was partially different from the piezo-resistive one. Only one trial per surface has been done.

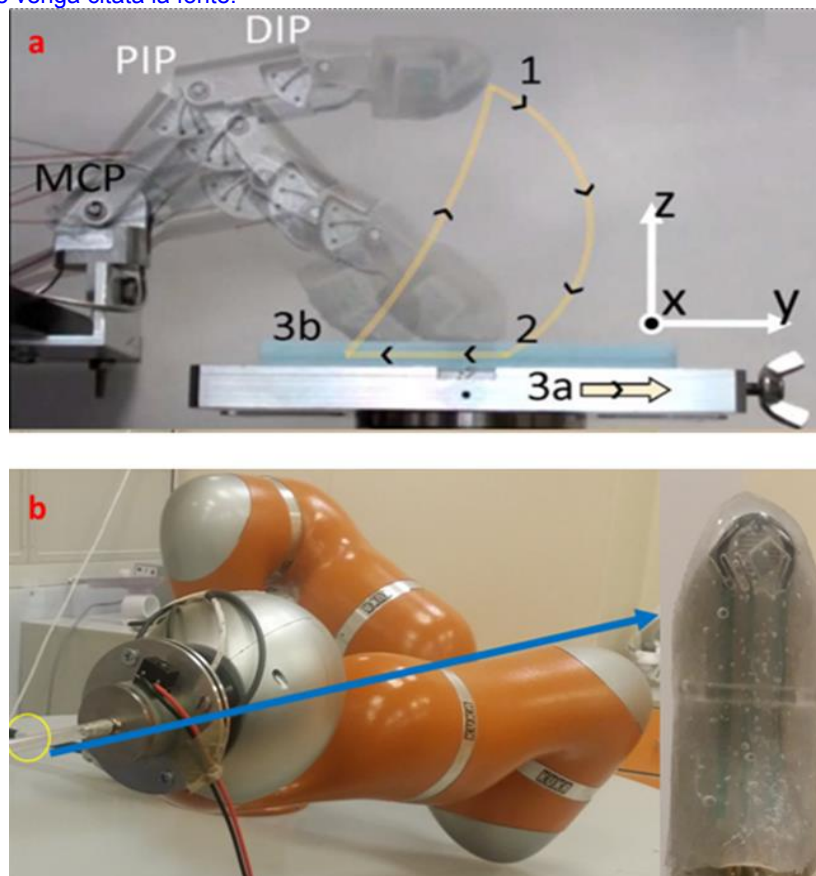


Figure 4.7. Automated set-ups for MEMS sensors (a) and FSR sensors (b). © [2011] IEEE (a).

4.4 Experimental validation and results

The first validation of the slip detection algorithm has been made on the MEMS piezo-resistive sensors. The rougher tactile stimuli, with $\Delta\mu$ values comprised in the [400-480] μm interval, have been selected as the first surfaces to validate the method on. Subsequently, validation tests have been performed with FSR sensors on the finer surfaces described in Chapter 2, whose roughness was at maximum 3.2 μm ; finally, a proof of concept of the method application to the tangential forces has been got thanks to use of the JR3 sensors.

In all the cases, the sensors raw voltage output has been taken as input for the algorithm, according to the block scheme illustrated in Figure 4.1. Obviously, it is possible to convert such output into a force value

by using either appropriate transformations matrices (JR3 and MEMS), or a given mathematical model (FSR); nonetheless, the voltage signal contains all the information, in terms of frequency content, necessary for performing slip algorithm. This comes to be highly convenient when the slip algorithm has to run in real time, e.g. when it is included in a robotic hand control system. Indeed, force estimation from the piezo-resistive voltage output and slip detection can be performed as parallel operations, rather than subsequently.

4.4.1 MEMS sensors

The method for slip detection presented in this work has been applied to all of the 16 available channels of the MEMS sensors, for every trial. The ON/OFF signals have been grouped taking into account the channels physical orientation. More in particular, 4 groups including 4 channels, have been created: the transversal orientation, both *proximal* and *distal*, and the longitudinal orientation, both *ulnar* and *radial*. Figure 5 represents the allocation of the sensing units on the bio-mimetic fingertip, while Table 4.1 groups them with respect to their orientation. The 4 groups have been identified as follows:

- TP (Transversal Proximal)
- TD (Transversal Distal)
- LU (Longitudinal Ulnar)
- LR (Longitudinal Radial)

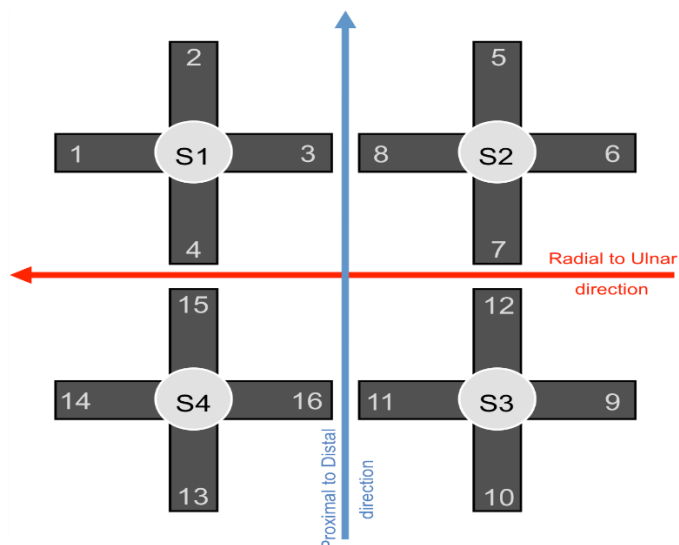


Figure 4.8. Positioning of the 16 tactile units on the fingertip (Romeo, 2017b).

Table 4.1. Groups of channels to which the AND calculation has been applied (Romeo, 2017b).

Channels	Name	Acronym
14, 16, 11, 9	Transversal Proximal	TP
1, 3, 8, 6	Transversal Distal	TD
5, 7, 12, 10	Longitudinal Radial	LR
2, 4, 15, 13	Longitudinal Ulnar	LU

In this way, the ON/OFF signal obtained from every channel has been put into an AND mechanism, resulting in four ON/OFF signals. The latter have been in turn put into an OR mechanism for the determination of the final ON/OFF signal. The basic concept is the following:

1. the presence of slip phenomena has been investigated on every possible direction, both transversal and longitudinal;

2. the AND mechanism allows avoiding/reducing the detection of false positives, which mainly occur during the contact and release phases;
3. the OR mechanism among the four AND signals allows detecting the slippage as it is detected on at least one of the directions.

As regards the ON/OFF computation, it is important to highlight the width of the temporal window employed. The computational operations described in Section 4.2, including the ON/OFF, have been accomplished setting the time window width to 40 ms. This value resulted from a tread-off between the necessity of achieving computational times below the physiological times needed to respond to slip events (i.e., >70 ms (Johansson, 1984; Macefield, 1996)) and the correct detection of the slip events themselves, minimizing the detection of false positives. Figure 4.9 illustrates an output from one of the tactile units, and the result of the algorithm together with the ON/OFF signal calculated with different time windows. Evidently, as the window becomes smaller, false positives probability to be detected augments. The enveloped signal is considered to be ON if its average value within the time window overcomes an empirically established threshold for the whole duration of the window itself. The threshold can be adjusted according to the employed resistive technology; it may vary from a kind of sensor to the other (e.g., FSR, strain gauges etc.). In this case, it has been set to 0.5 V. Moreover, a time window of 40 ms corresponds to a 15 samples window, given that the sampling frequency F_s was equal to 380 Hz.

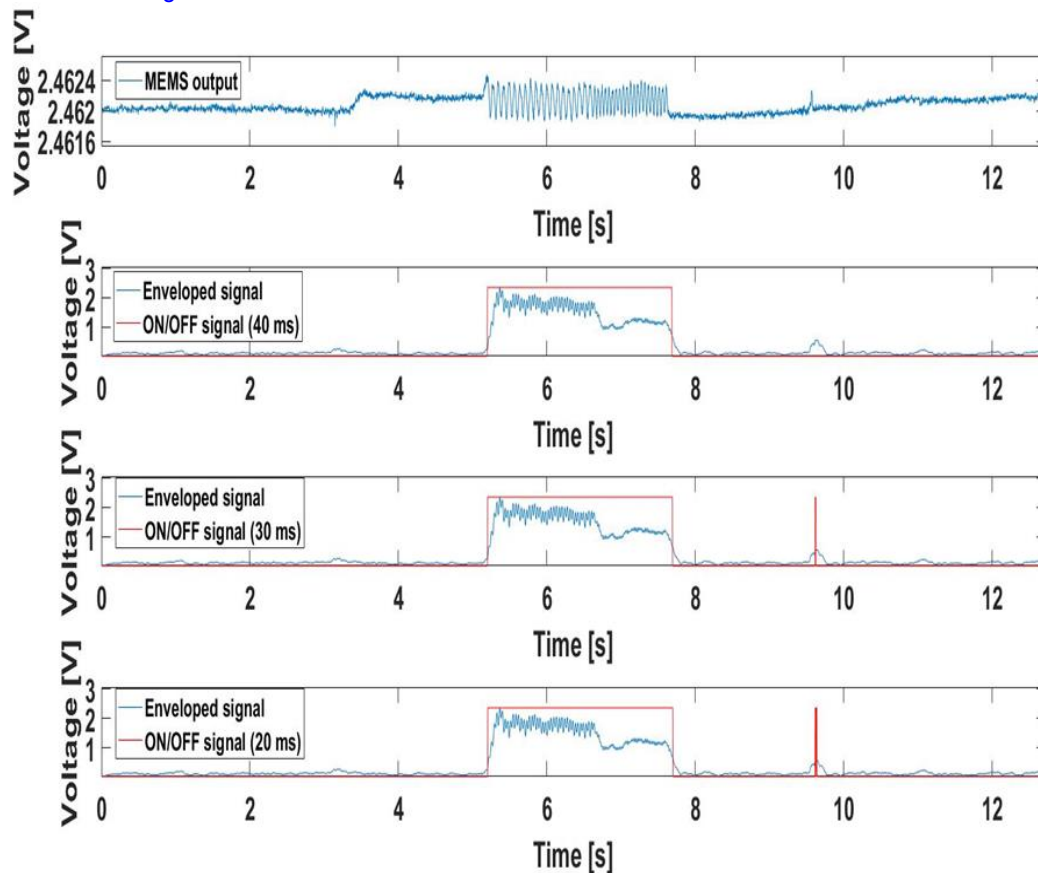


Figure 4.9. Voltage output from a tactile unit and the result of the algorithm application. The enveloped signal has been computed using a 40 ms time window, whereas the ON/OFF signal is calculated with varying time windows. It is clearly noticeable that the narrower is the window, the higher is the possibility to detect false positives (Romeo, 2017b).

The filter network has been dimensioned in order to privilege the bandwidth B_w [10-50] Hz, where 10 Hz is f_{col} and 50 Hz is f_{coh} . The polymeric encapsulation of the sensors acts as a low-pass filter for high frequencies generated during a relative movement; plus, considering the relation between the Δp of the tactile stimuli and the velocities used during its exploration (Equation 2.4), the fundamental frequency range was [14-25] Hz. As a consequence, to set the f_{coh} double than the highest fundamental frequency can be satisfactory. On the other hand, the cut-off frequencies of the two elliptical filters have been chosen so as to place their stop-bands next to B_w , in the regions [1-11] Hz (*low filter*)

and [45-199] Hz (*high filter*); clearly, the high limit of the high filter has been set to around half F_s (Shannon-Nyquist Theorem). A minimum overlap of the low filter bandwidth with the meaningful one can be noticed: it allows a more proper cut-off of the frequencies in the region 7-9 Hz. This is due to the fact that the implemented filters are real filters; thus, the filter will effectively start attenuating with a shift of 1-2 Hz, as depicted in Figure 4.10. The same way, a small margin has been left between the low limit of the high filter and f_{coh} . Furthermore, it is worth noticing the approximately linear phase in the stop-band region of the filter. This is the best achievable result in terms of signal distortion avoidance with IIR causal filters (like the ones employed in this work), whose phase distortion is usually highly nonlinear.

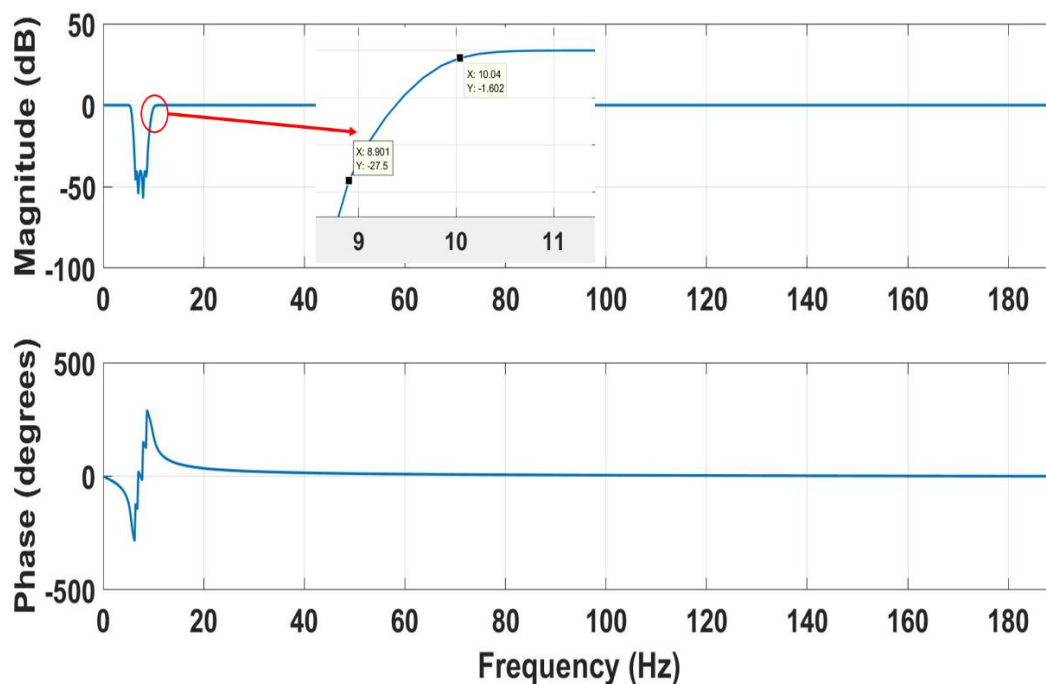


Figure 4.10. The transfer function H_{e1} and a detail of the high limit of its band.

As already stated, thirty trials have been performed: first, it is crucial to evaluate the delay D between the start of the platform movement with respect to the bio-mimetic finger, and the OFF to ON transition of the slip signal. The time instant t_{st} at which the platform starts to move has been computed as follows:

$$t_{st} = \left\{ t_1 \in T \mid \frac{dx_{pl}(t)}{dt} \neq 0 \right\}, \quad (4.11)$$

i.e., the first time instant t_1 at which the platform position value x_{pl} is different from the previous one, it is considered as the start of the relative movement between the platform and the robotic finger during the trial time interval T . In this way, a rigorous measurement is done, with movements inferior than $5 \mu\text{m}$ considered as the start of the aforementioned movement. Figure 4.11 explains this concept.

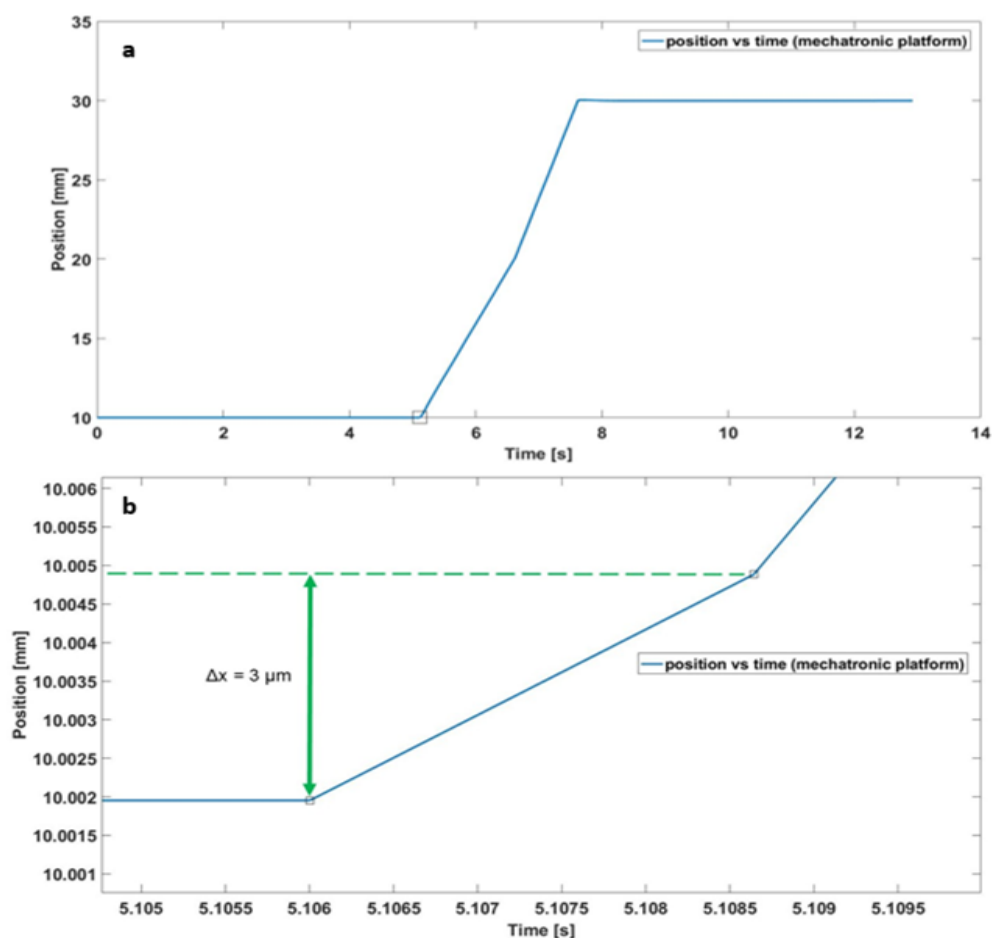


Figure 4.11. Movement of the mechatronic platform during a trial: (a) whole trial. From 0 s to around 5 s, the platform stands still, then starts moving, accelerates (from 6.7 mm/s to 10 mm/s) as the slope varies and finally stops around 7.5 s; (b) detail of the black square in (a). The movement is considered to be commenced as a $3 \mu\text{m}$ displacement has occurred (Romeo, 2017b).

Such a rigorous condition gives the algorithm a challenge for the prompt detection of slippage. As already referred in Subsection 4.4.1, the time window for the algorithm execution has been regulated accounting the physiological response times as well. The same applies for the delay D : it must be lower than 70 ms, possibly not greater than 50 ms as D does not include the efferent response, but only the afferent one. That is, detecting the slippage must be followed by an opportune reaction (either of the robot or the human) in terms of force adjustment. Table 4.2 summarizes the mean values mD_i for all the trials carried out for the three Δp s.

Table 4.2. This table contains the mean delays mD_i of every trial, obtained upon all the 16 channels for every Δp (Romeo, 2017b).

Trial	mD ($\Delta p=400\mu\text{m}$) (ms)	mD ($\Delta p=440\mu\text{m}$) (ms)	mD ($\Delta p=480\mu\text{m}$) (ms)
1	43.37	66.66	73.48
2	33.19	55.44	44.01
3	33.19	42.57	55.98
4	39.60	37.29	40.92
5	34.32	36.30	47.96
6	33.19	39.27	50.16
7	35.83	34.98	43.56
8	37.33	33.99	39.16
9	30.55	36.30	44.88
10	39.60	34.98	48.84

All the values in Table 4.2 have been calculated as follows:

$$mD_{i,\Delta p_j} = \frac{\sum_{k=1}^{16} ch_k}{16}, \quad (4.12)$$

where i is the trial number, Δp_j is the corresponding Δp and k is the channel number. Such values resulted to be acceptable (<50 ms) in the majority of the cases. These data can be further synthesized by observing the mean values $mD\Delta p$ for every Δp , i.e. the sum of the $mD_{i,\Delta p_j}$ in every column of Table 4.2 divided by the number of trials performed per every Δp (10), which resulted respectively to be:

- $mD400=36.02$ ms,
- $mD440=41.78$ ms,
- $mD480=48.90$ ms.

Such results do confirm the validity of the slip detection algorithm presented here, in terms of promptness. The $mD\Delta p$ value seems to increase proportionally to the stimulus spacing Δp , though no causal relation between such two quantities has been identified.

Another crucial feature that should characterize an algorithm for the prevention of slip events regards the correct detection of the true positive, i.e., the slip events themselves, together with avoidance of false positives. While grasping an object, the latter might principally occur during the contact and/or release phases. In Figure 4.12, some examples of the algorithm performance are shown, extracted from one of the trials relating to the $440 \mu\text{m}$ stimulus. A channel from each of the four groups mentioned previously is displayed in the panel (a) and (b); panel (c) shows the result of the AND mechanism for all of the four groups, whereas panel (d) depicts the final ON/OFF slip signal yielded by the OR mechanism involving the four AND signals. In every plot, a black asterisk designates the start of the mechatronic platform movement (start of slip), calculated according to (1), that is, t_{st} .

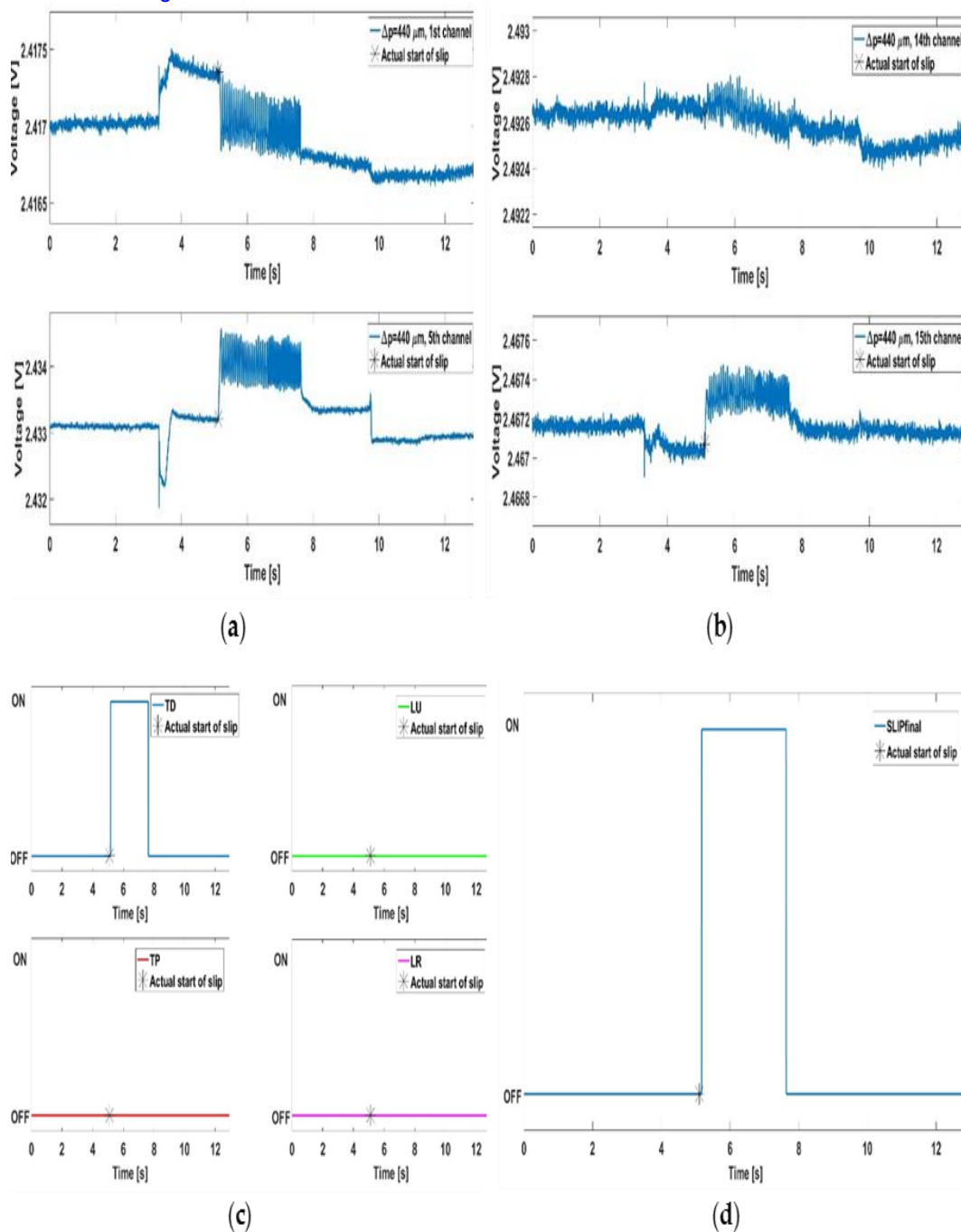


Figure 4.12. Algorithm performance plots. Panels (a) and (b) show the MEMS sensors output from some of the channels, one for each of the four groups reported in Table 4.1; panel (c) contains the AND mechanism results for every group; panel (d) represents the final slip signal (OR of all the ANDs) (Romeo, 2017b).

Panel (c) highlights how three of the four ANDs result in an OFF signal for the entire duration of the trial. This is due to the non-ideal contact conditions some of the channels come to, as the panel (b) shows

(channel 14). It is quite complicated to achieve an ideal contact condition on all the sixteen channels, as one or more of them do not properly touch the stimulus surface while the platform moves. This is reasonable from a biological point of view: the human finger involves its components differently from a manipulation task to the other, and the same task may be performed using different tactile areas of the fingers. Nevertheless, even if it cannot be expected to have all of the 16 channels in a good contact condition, the robustness of the algorithm always allowed detecting the true positive as it is sufficient to achieve the ON at least on one of the four ANDs. In fact, Panel (d) illustrates the ON signal, which covers the whole duration of the slip event. No false positives are detected. The same considerations can be extended to Figure 4.13, which relates to a trial carried out onto the 480 μm stimulus.

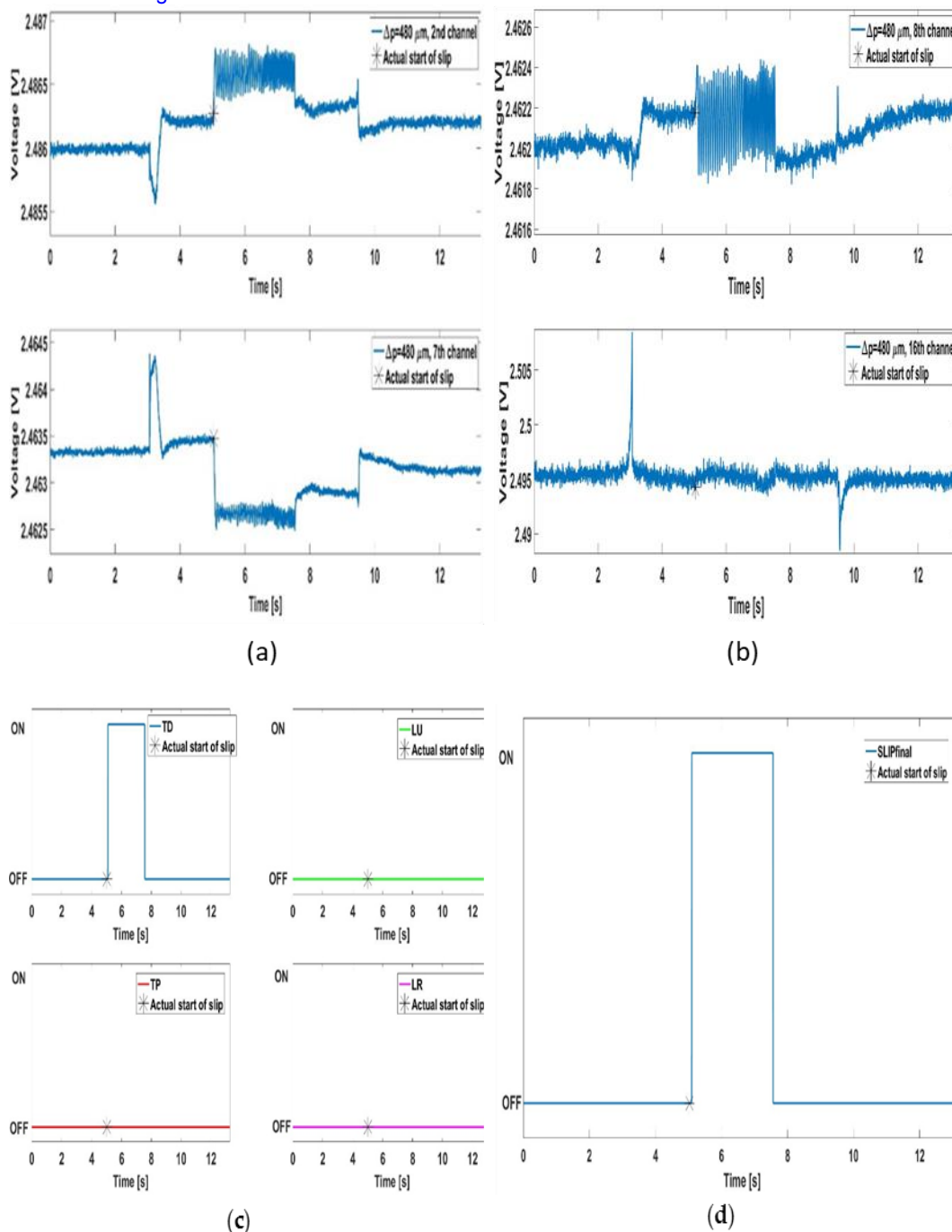


Figure 4.13. Algorithm performance plots. Panels (a) and (b) show the MEMS sensors output from some of the channels, one for each of the four groups reported in Table 4.1; panel (c) contains the AND mechanism results for every group; panel (d) represents the final slip signal (OR of all the ANDs) (Romeo, 2017b).

It can be noticed how the MEMS signals taken from different channels than in Figure 4.12 have different shape as well. This is due to the various contact conditions that every tactile array unit faces, as already

referred. Most notably, channel 16 is characterized by huge peaks in correspondence of the contact instant and release instants, with no useful content during the slip event.

Although the *a priori* known difficulties of involving all the sixteen channels in the algorithm, its overall success rate in identifying slippage events has been equal to 100%, as it correctly recognized the slippage event in all the 30 trials. False positives were rarely detected by the algorithm; for evaluating their detection, the time lapse t_{fp} when false positives can occur has been considered, which is the trial time T (i.e. 6.5 s) decreased by the actual slippage event duration (i.e. 2.5 s). Figure 4.14 graphically exemplifies it. The mean percentage of false positives, computed with respect to t_{fp} , resulted to be: 1.01% ($\Delta p=400 \mu\text{m}$), 0.11% ($\Delta p=440 \mu\text{m}$), and 0.88% ($\Delta p=480 \mu\text{m}$).

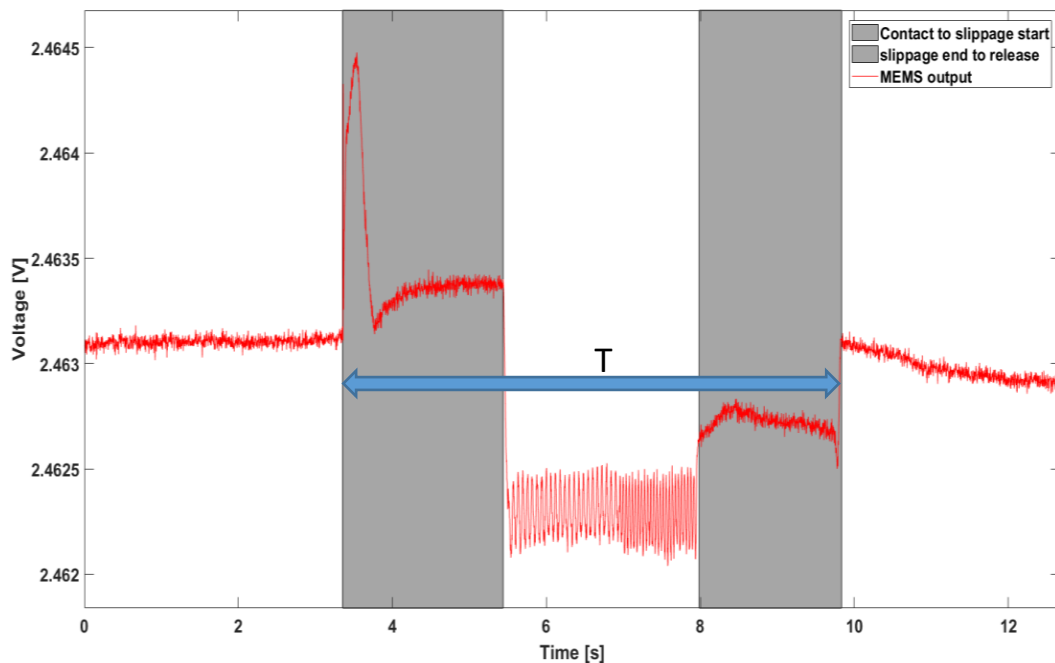


Figure 4.14. Trial T subdivision for false positives computation. The durations of both grey areas (2 s each) are summed (achieving t_{fp}); the result is used to normalize the duration of false positives.

4.4.2 FSR sensors

As concerns the FSR sensors, which are mono-axial and do provide only the normal force component, the algorithm has been implemented through a hardware solution. A dedicated PCB has been printed in order to receive the FSRs input and to perform the operations of the various algorithm blocks, with the only exception of the ON/OFF signal generation; the latter has been done through a Matlab *mathscript* embedded into a LabVIEW code. A different filter network has been obtained according to the following modifications:

- 3rd order high-pass analog filter;
- half-wave rectification (no exponentiation);

The choice of high cutting frequencies, e.g. above 500 Hz, allows to more effectively elide false positives due to contact and/or release of the sensor during the interaction with the object. Notwithstanding, by cutting off all the frequencies below 10 Hz, which are the dominant ones in the force signal, it is still possible to get a generalized filtering block for each type of resistive sensor. As an example, let us consider the signals in Figure 4.2-4.4; the piezo-resistive signal is the output from an FSR sensor, while the filters have been dimensioned as described in the previous Subsection.

The choice of a 1st to a higher order filter allows to eliminate, or at least greatly reduce, the components at a lower frequency due to the contact and release events of the sensor. For this purpose, a proper filter network might be created. Figure 4.15 shows the schematic design of the dedicated PCB, whose electrical components were all SMD technology; the aforementioned network is composed of 3rd order high-pass filter, which in turn consists of two sub-blocks: a 1st order filter, and 2nd order one in the *Sallen-Key* topology, both high-pass type. The

so obtained signal is characterized by high frequencies, and its amplitude is dictated by the electrical components chosen for the dimensioning of the filter network.

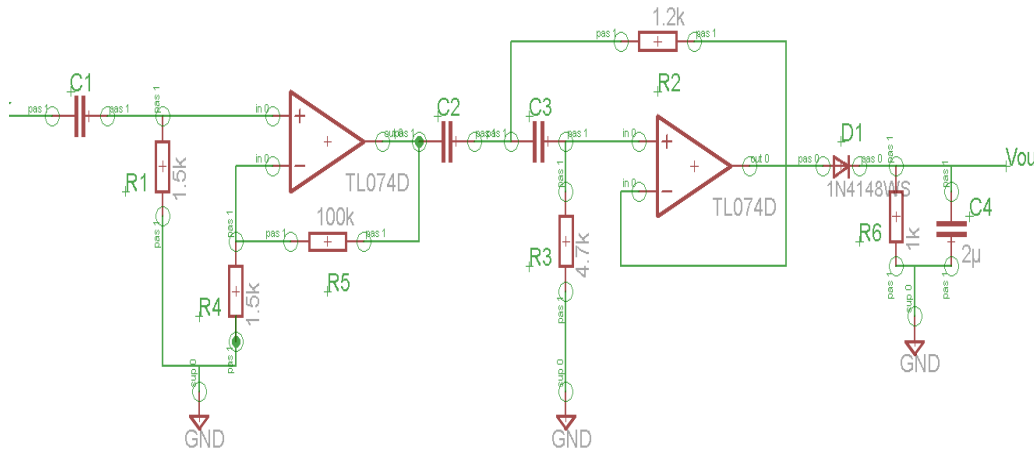


Figure 4.15. PCB schematic.

The transfer function of the 1st and 2nd order filters, respectively $H_1(s)$ and $H_2(s)$, can be expressed by the following formulas:

$$H_1(s) = \frac{s}{s+2\mu f_{c1}} \quad (4.13)$$

$$H_2(s) = \frac{s^2}{s^2+2\zeta(2\mu f_{c2})s+(2\mu f_{c2})^2} \quad (4.14)$$

whereas the overall filter network transfer function is:

$$H_3(s) = H_1(s) \cdot H_2(s) = \frac{s}{s+2\mu f_{c1}} \cdot \frac{s^2}{s^2+2\zeta(2\mu f_{c2})s+(2\mu f_{c2})^2} \quad (4.15)$$

where G is the network gain, f_{c1} and f_{c2} are respectively the cut-off frequencies of the 1st and 3rd order filters and ζ is the damping factor. More in detail, for the adopted filter network configuration, also being $C_1=C_2=C_3=0.01\mu\text{F}$, these quantities are given by:

$$G = 1 + \frac{R_5}{R_4} = 66.7 \quad (4.16)$$

$$f_{c1} = \frac{1}{2\pi R_1 C_1} = 1.06\text{kHz} \quad (4.17)$$

$$f_{c2} = \frac{1}{2\pi\sqrt{R_2 R_3 C_2 C_3}} = 0.67\text{kHz} \quad (4.18)$$

$$\zeta = \sqrt{\frac{R_2}{R_3}} = 0.5 \quad (4.19)$$

Evidently, the gain G of the whole network can be entirely controlled by the regulation of R_4 and R_5 ; there is no need for modification of other parameters such as cut-off frequencies or damping factor. Being a 1st order filter (20 dB attenuation) cascaded to a 2nd order filter (40 dB attenuation), the total roll-off is equal to 60 dB. Figure 4.16 shows the Bode Diagram with the transfer function variation for different values of R_4 : as expected, the magnitude augments as the resistance value diminishes. The figure represents the gain-bandwidth product GBW as well, which for the chosen amplifier (TL074 by Texas Instruments, Inc.) was equal to 3 MHz. To guarantee a proper functionality of the amplifier, it is necessary to maintain the transfer function value inferior to the GBW at every working frequency. The value of all the passive electrical components mounted on the PCB have been selected taking this consideration into account, with the idea of obtaining a gain G at least equal to 30 dB, and the two cut-off frequencies around 0.7 kHz and 1 kHz. The FSR response, even if the sensor is covered with the prosthetic silicon cap, indeed appears higher than the MEMS one, leading to the necessity of broader bandwidth and higher cut-off frequencies.

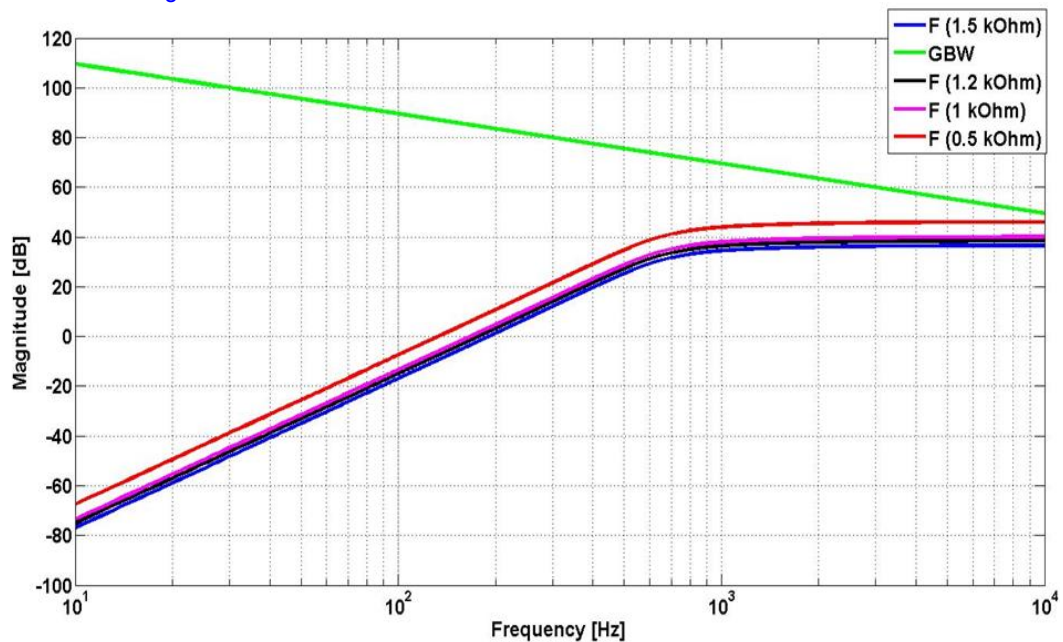


Figure 4.16. Bode Diagram of $H3(s)$ for different $R4$ values.

Immediately after the filtering stage, a rectification stage is built; in this case, it has been a half-wave rectification, consisting of a diode (1N4148) in series to the said filter network and a resistor (R_6) between the diode and the ground. Full-wave rectification is possible by realizing a diodes bridge in place of the single diode used in this work. The signal is thus rectified, and made unipolar. The addition of a capacitor in parallel to R_6 gives way to a low-pass filter, which produces an envelope of the high frequency rectified signal. Finally, the ON/OFF slip signal is yielded by means of the above said *mathscript*. The time window for the ON/OFF calculation has been again chosen as large as 40 ms; though, this time it was composed of 80 samples, as the sampling frequency was equal to 2000 Hz.

Figure 4.17 shows the result of the algorithm application on the roughest available surface, i.e. $3.2 \mu\text{m}$, at a speed of 4 cm/s. Figure 4.18 shows the same but on the smallest roughness available surface, i.e. $0.2 \mu\text{m}$. In both cases, the ON/OFF signal covers all the duration of the induced slippage, without presence of any false positive.

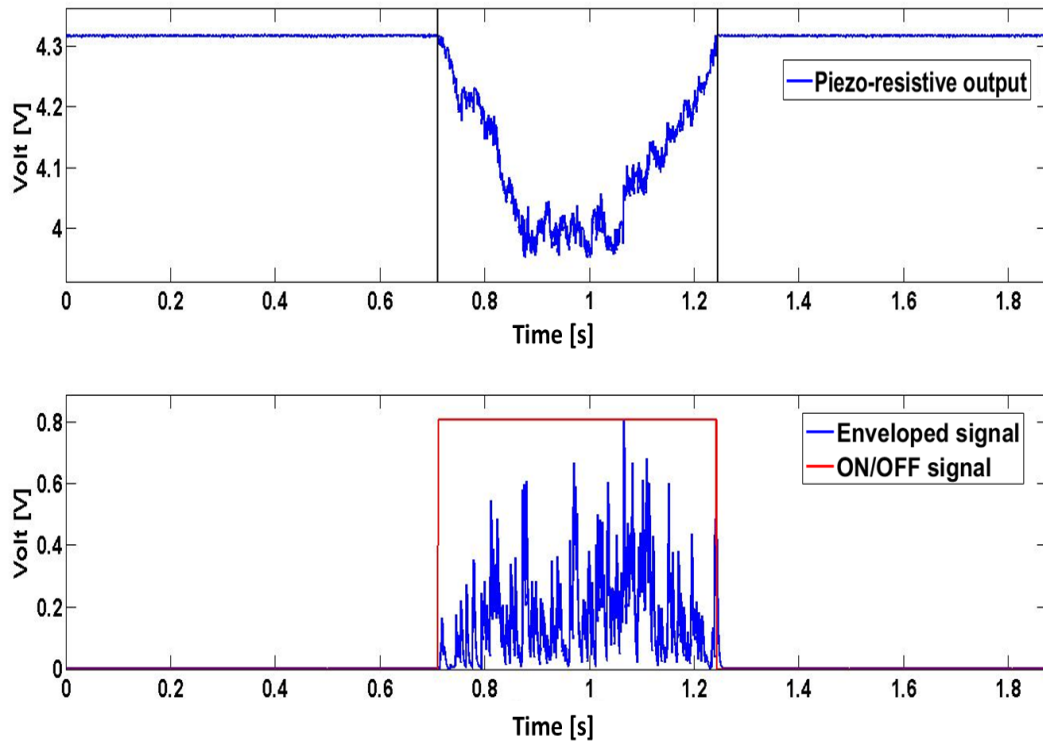


Figure 4.17. FSR raw voltage signal (top) and algorithm output (bottom). Test surface: 3.2 μm roughness.

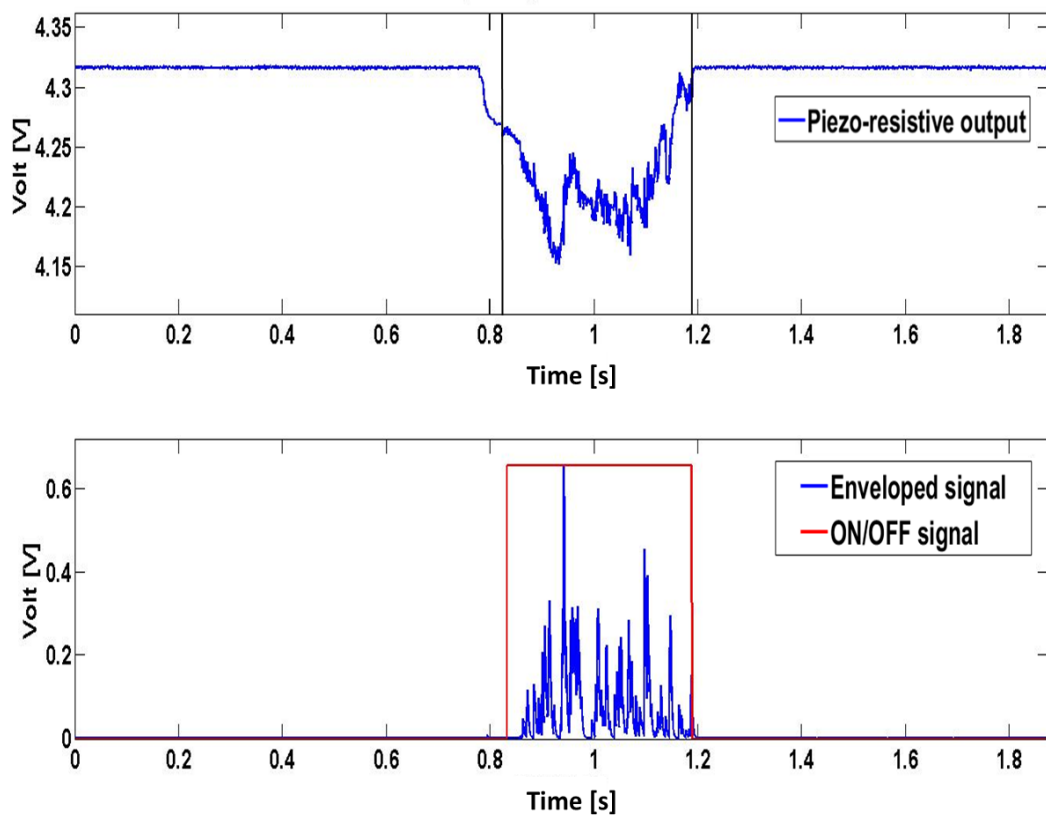


Figure 4.18. FSR raw voltage signal (top) and algorithm output (bottom). Test surface: 0.2 μm roughness.

Figure 4.19 illustrates instead a trial executed at a velocity of 2 cm/s, this time on the 0.8 μm roughness surface. Clearly, the smaller is the velocity, the harder is to detect slip. Nonetheless, slip event has been correctly recognized in this case as well; the ON/OFF signal is not continuous but, once the slip event has been recognized with an acceptable delay, this is no longer an issue. In this trial, the voltage level appears to change at the contact phase, differently from the previous trials. Small signal peaks can be observed during contact and release phases, though they are properly excluded by the ON/OFF threshold mechanism.

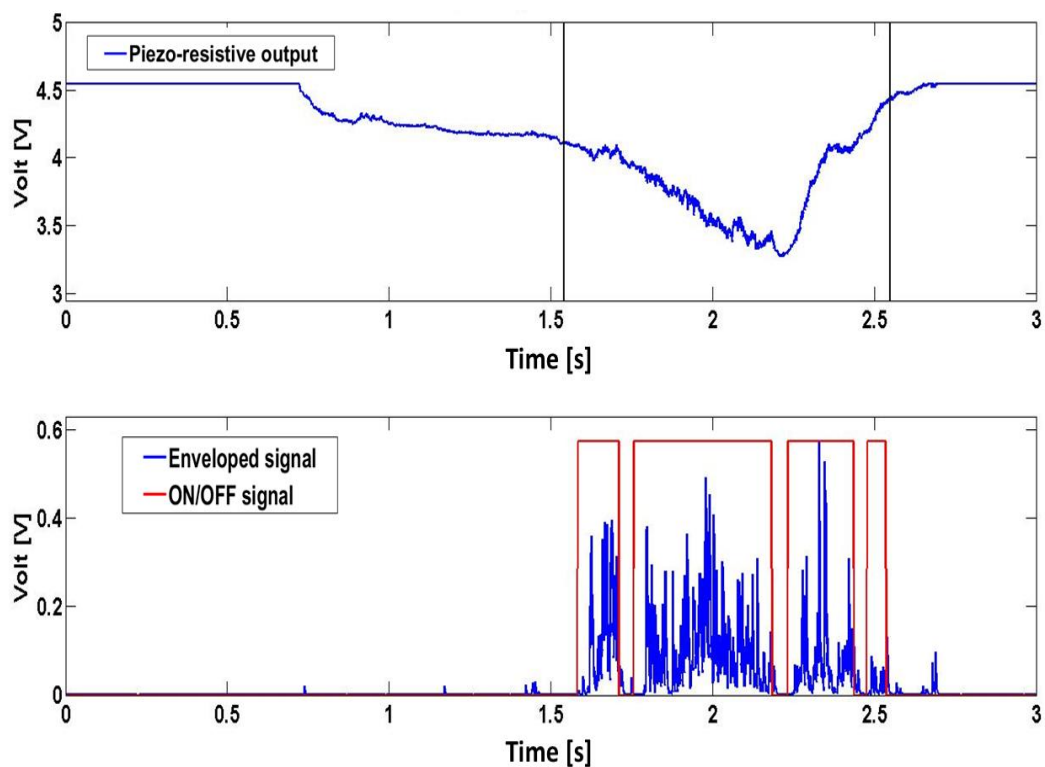


Figure 4.19. FSR raw voltage signal (top) and algorithm output (bottom). Test surface: 0.8 μm roughness. Velocity: 2 cm/s.

Again, the window width plays a crucial role in the false positives exclusion. A too small window can more easily detect peaks generated during non-slip phases, as already discussed in Subsection 4.4.1. Figure 4.20 exemplifies the same concept applied to the hardware

implementation of the algorithm, with a different typology of sensors than MEMS (i.e., FSR). The test velocity was 4 cm/s.

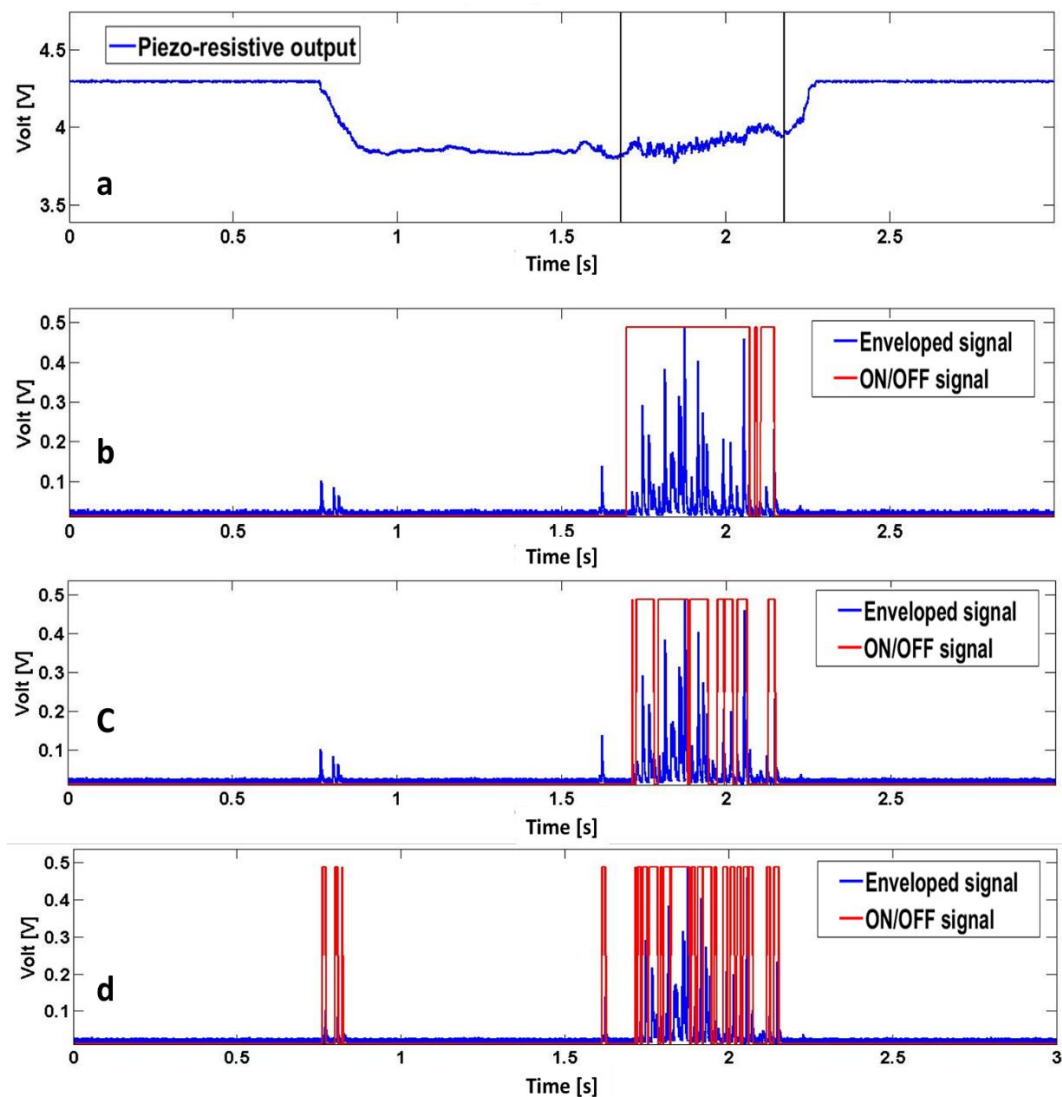


Figure 4.20. FSR output (a); ON/OFF signal computed with a time window as large as: 40 ms (b); 20 ms (c); 10 ms (d).

There is no theoretical limit for the window width: it can be chosen as narrow (or large) as desired. A time window of 1 ms, or even smaller, is also possible, depending on the sampling frequency (e.g., $F_s=2$ kHz implies the smallest window to be 0.5 ms): though, false positives will be inevitably comprised in the ON/OFF signal. The final window width has been chosen following the criteria described in Subsection 4.4.1. Finally, the medium delays for the three trials executed on every surface

are reported: 35.44 ms (surface roughness: 0.2 μm), 31.89 ms (surface roughness: 0.8 μm) and 25.71 ms (surface roughness: 3.2 μm).

Such delays are lower than the ones found for the MEMS sensors with the software method implementation, indicating an improvement of the performances achieved through the hardware implementation.

4.4.3 Strain gauge sensors

The presence of slip phenomena on the tri-axial output of the strain gauge sensors (JR3) has been analyzed by means of the software method implementation. The algorithm has been applied in the same way as in Subsection 4.1.1 regarding the MEMS sensors. The main goal was to gather insight from the method application on tangential forces, apart from the normal one. Besides, a different resistive technology had to be tested in order to extend the validity of the slip detection method presented in this work. In the following, the result of the two tangential forces analysis during a 4 cm/s trial on a surface with roughness 0.8 μm will be provided (Figures 4.21-4.22).

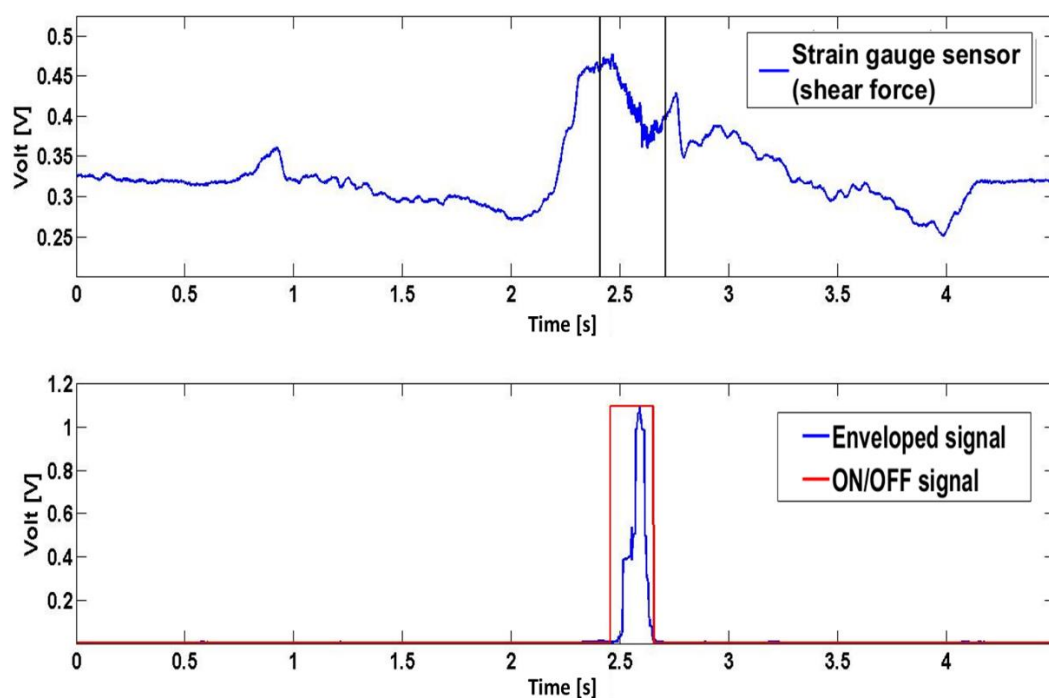


Figure 4.21. Tangential force (top) and algorithm application (bottom).

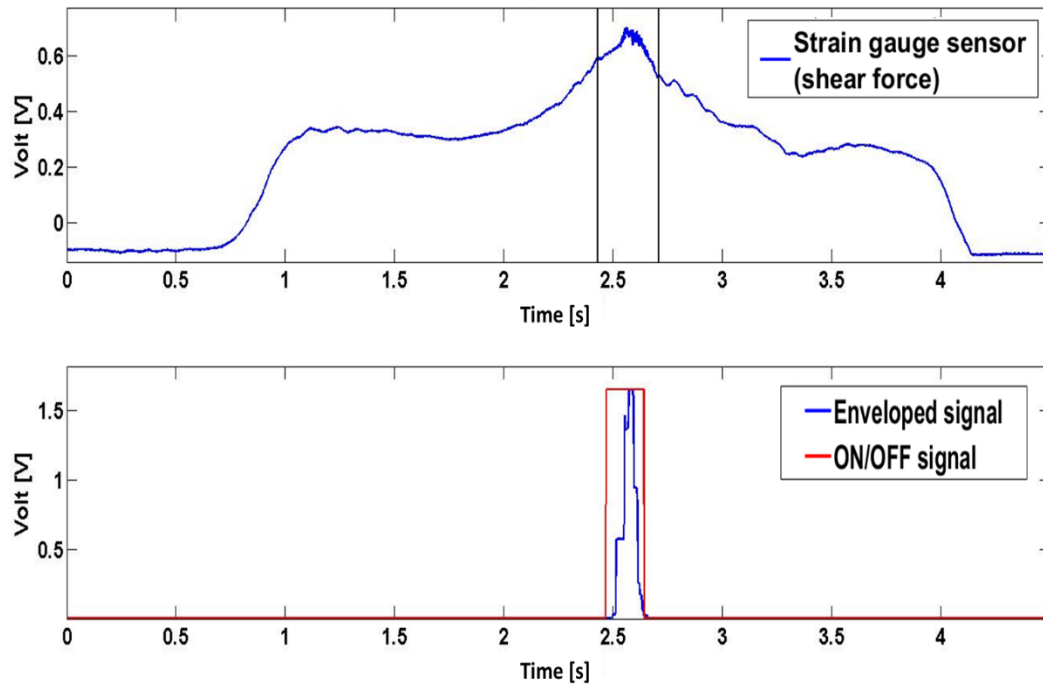


Figure 4.22. Tangential force (top) and algorithm application (bottom).

The delays for the two trials resulted to be respectively 51.25 ms and 39.18 ms. Results are good, as the delays were quite low and no false positives have been detected, although the major instability and fluctuations of the voltages related to the tangential forces. Such results foster the idea to perform more trials on the tangential forces with multi-axial force sensors, in order to confirm them and to augment the robustness of the slip detection method.

4.4.4 Online application

The algorithm for slip detection described in this Chapter is performable online. The feasibility of embedding the algorithm into a real-time prosthetic control system has been demonstrated in (Barone, 2016). Such a publication has presented the results of a hierarchical control structured as follows:

- It is distributed on two levels: a high level based on learning, for trajectory planning and finger coordination, and a low-level for force and position control;

- The low level is made of a parallel force/position control endowed with slippage prevention capability.

The information managed at the second level allows the loop closure, creating the possibility to adjust force levels according to the online slip detection and to the measured force levels themselves. In particular, one FSR sensor has been positioned on the fingertip of thumb, index and middle fingers of IH2 prosthetic hand, and its output has been used for the twofold purpose of measuring the normal force component and detecting slippage. Therefore, FSR voltage signal has been properly processed to extract the normal force component as well as information about slippage events. The former has been extracted thanks to the calibration procedure described in Chapter 2, while the latter has been the ON/OFF slip signal as illustrated in this Chapter.

The hardware implementation (Subsection 4.4.2) has been employed for the online implementation. The experimental set-up for the validation of the two-level control is depicted in Figure 4.23. Slippage has been automatically induced by means of a seven degrees of freedom robotic arm (KUKALWR 4+), whose end effector has been a thin, cylindrical probe. Slip experiments have been executed by actuating the probe for 1 cm at two different speeds (i.e. 2 cm/s and 4 cm/s), in order to assess control stability and robustness at increasing velocities. Experiments without considering the slip information (i.e., relying on the sole force/position control) have been carried out only at 4 cm/s, which has been the most challenging tested condition.

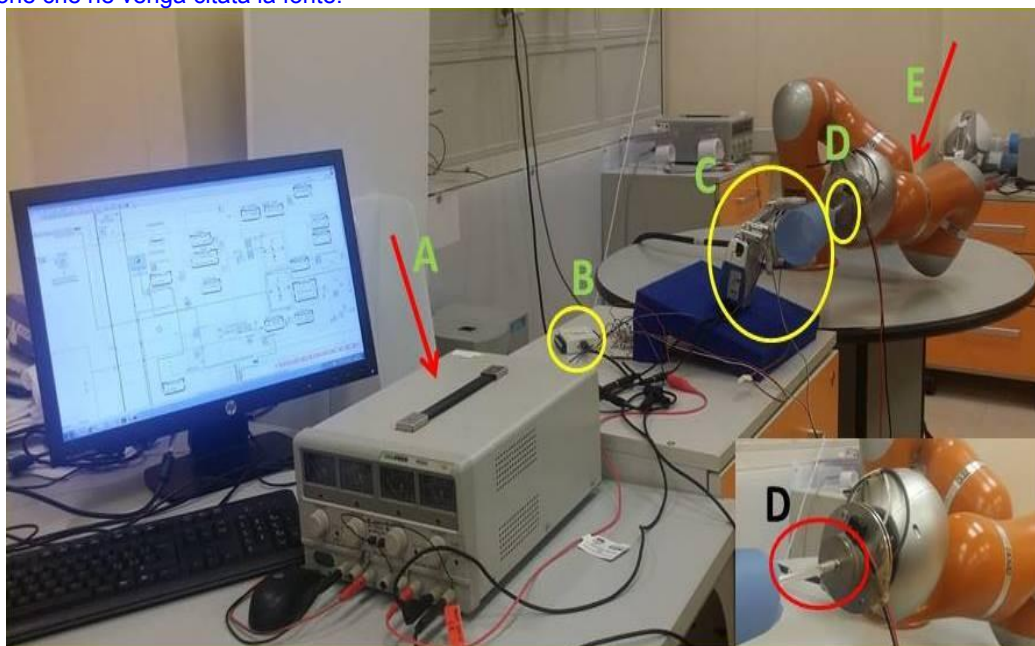


Figure 4.23. Experimental set-up (Barone, 2016). DC power supply for electronics, sensors and prosthetic hand (A); NI-DAQ device (B) for data acquisition; prosthetic hand grasping a cup (C); end effector inducing slippage (D); KUKA-LWR 4+ robotic arm (E).

Three widely used objects during activities of daily living (ADLs) have been selected for performing two kinds of grasp: bipod and tripod (Figure 4.24). The former has been performed with an egg and a highlighter, the latter with the same egg and with a cylindrical plastic cup. The masses of the objects were around: 60 g (egg), 50 g (cup) and 10 g (highlighter). The purpose of the experimental tests has been to investigate the stability of the grasp when an external perturbation is applied in the two cases of presence or absence of slip detection, and to verify system robustness with respect to the type of perturbation. In all cases, six repetitions have been performed, resulting in a total of 72 trials. All the data have been acquired at a sampling frequency of 2 kHz by a NI DAQ (NI-6009) device, and the slip signal has been recorded even when not employed for the control. The three sensorized fingertips have been covered with prosthetic silicon caps.

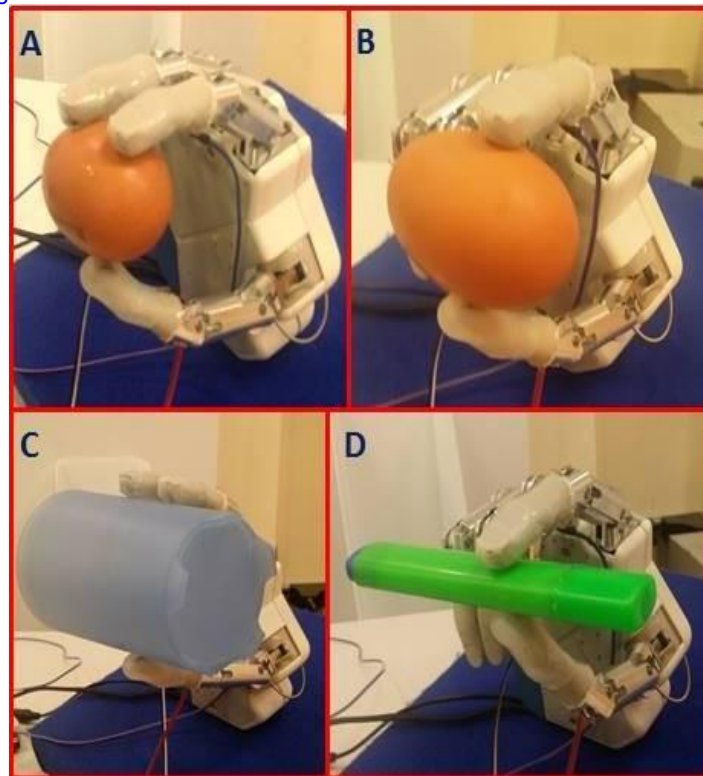


Figure 4.24. Grasps performed by the IH2 hand during the experiments (Barone, 2016): tri-digital with egg (A) and cup (C), bi-digital with egg (B) and highlighter (D).

Figures 4.25 and 4.26 show the measured forces compared with the desired force for both conditions of slippage control ON and OFF. When slippage control is OFF, the grasped object is perturbed by two identical perturbations of 1 cm at the maximum speed possible (4 cm/s) so as to demonstrate that the object falls, or at least is unstably grasped. When the slippage control is active, one perturbation of 1 cm at different velocities (2 cm/s and 4 cm/s) is produced; as expected, the system is able to immediately detect slippage. The activation command for the robotic arm was given as soon as the forces reached a steady state; hence, it can be observed that perturbations were not applied at the same time instants in all the trials. In Figure 4.25 it is shown a trial of the tripod grasp of the plastic cup with the slip prevention algorithm disabled and perturbation set to 4 cm/s. After the forces reached the steady state, a first disturbance is applied and the controller avoids the

cup fall thanks exclusively to the parallel force/position control. The grasp is maintained but it is no longer stable. In fact, as the subsequent perturbation occurs, index and thumb fingertips lose their contact with the object and the precision grasp fails. The middle fingertip accidentally continues touching the object because the object remains unstably grasped.

Figures 4.25b show a further trial of the tripod grasp of the cup, but this time the slippage prevention algorithm is active and the perturbation set to 2 cm/s. As the slip event due to perturbation is detected, the grip is strengthened and the grasp becomes stable. From force graph it can be noticed that index finger, on which the slippage prevention algorithm is computed, mostly contributes to grasp stability; its applied force evidently arises and, as a reaction, also thumb increases its force value while middle finger does not modify its action.

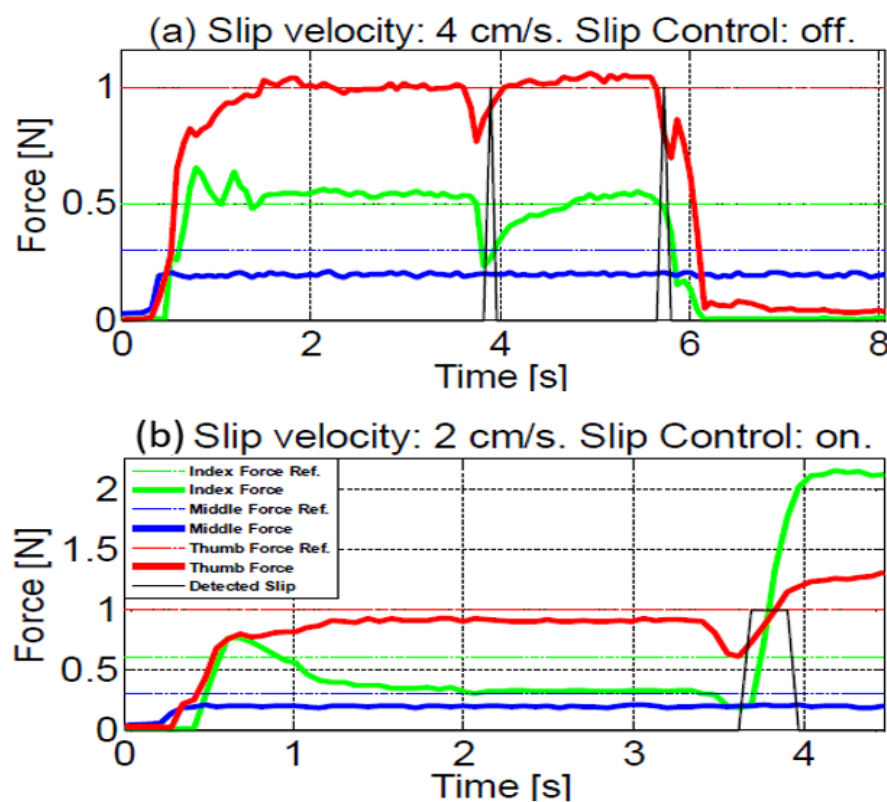


Figure 4.25. Experimental results with the plastic cup (Barone, 2016). Slippage control: OFF (a); slippage control: ON (b).

In Figure 4.26 the bipod grasp task of the highlighter is reported. In this case, when the control of the slippage is inactive the force references are well kept after the first as well as the second perturbation, but there is no incisive increase in the grasp forces. Rather, forces diminution can be observed in the force trend, confirming that the object is not grasped in a stable manner as a consequence of the perturbations. Figure 4.26b illustrates the reaction of the controller to a disturbance as fast as 4 cm/s, in order to show its capability of reacting also to the maximum velocity of the robotic arm. More seconds are needed to reach the steady state. In this trial the slip event is followed by a quick, high response of the index finger force and also the thumb increases its force in reaction. After the adjustment due to slippage, a grasp stability of the object is clearly reached.

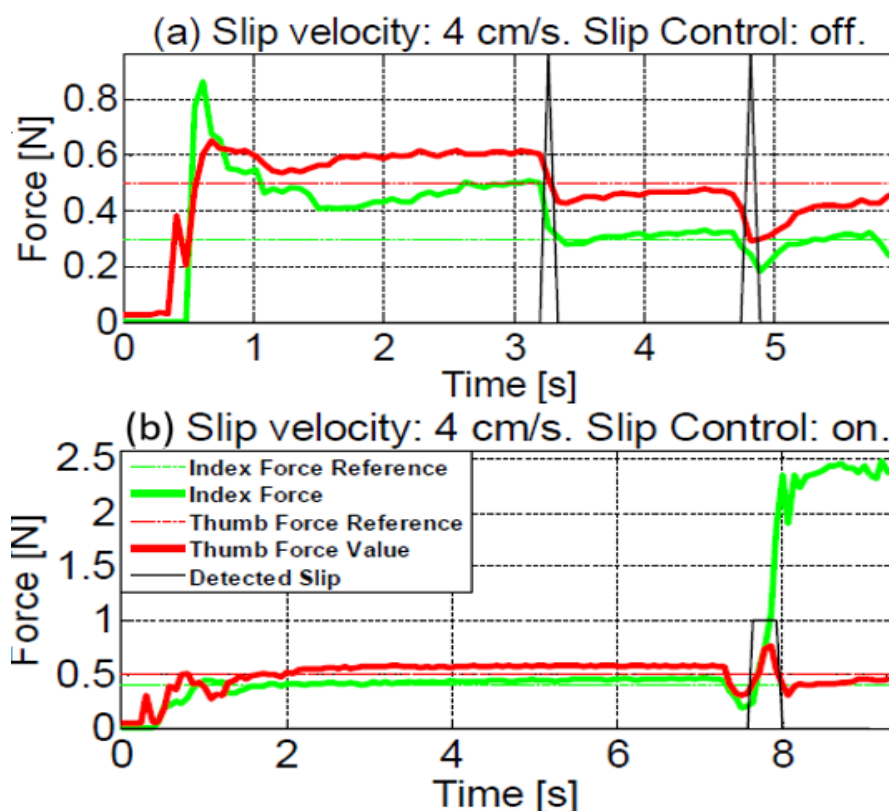


Figure 4.26. Experimental results with the highlighter (Barone, 2016).
Slippage control: OFF (a); slippage control: ON (b).

Table 4.3 summarizes the overall performances of the control architecture for all the 72 trials. As a confirmation of the results depicted in Figures 4.25-4.26, it can be seen that when the slippage control is OFF, the failure percentage often comes to be high. Oppositely, the enabled slippage control allows the prosthesis to stably hold the object in every perturbation condition with rare exceptions.

Table 4.3. Grasp failure percentages (Barone, 2016).

Object	Mass [g]	Trial	Failure percentage (No Slip Control, 4 cm/s)	Failure percentage (Slip Control, 2 cm/s)	Failure percentage (Slip Control, 4 cm/s)
Plastic cup	50	6	83%	0%	16.67%
Highlighter	10	6	16%	0%	0%
Egg Tri-digital	60	6	33%	0%	0%
Egg Bi-digital	60	6	50%	0%	0%

4.5 Conclusions

In this Chapter, a novel method for detection of slippage events has been proposed; said method has been presented through a detailed description of its sub-blocks, which include simple operations such as digital filtering, rectification and envelope of the input signal. Such sub-blocks are cascaded in order to generate the ON/OFF signal. The method has been validated on different typologies of resistive sensors, i.e. piezo-resistive (MEMS and FSR sensors) and strain gauges; ad hoc automated set-ups have been conceived for this purpose. The employed sensors have been both mono-axial, providing only the normal

component of the applied force, and three-axial, providing the tangential forces as well as the normal one.

Both hardware and software implementation of the proposed method have been realized. The first one relies on digital operations performed in a Matlab scenario, such as digital IIR causal filters that commonly feature non-linear phase and thus a nonzero delay between the original signal and the filtered one. The second is based on a PCB on which all the algorithm operations are performed (with some modifications), expect the ON/OFF signal. The latter is generated by means of a Matlab *mathscript* embedded in a LabVIEW code. Validation tests on MEMS sensors and strain gauge sensors (JR3) have been executed by means of the software implementation, while for the FSR sensors it has been used the hardware solution.

The main advantage of the algorithm is that it makes use of just one input signal (e.g., the normal force) measured through a resistive sensor, leading to an ON/OFF slip information. It is not necessary to employ the force value to apply the method on: the raw output voltage (relating to the force) can be used, retrieving the force value and generating the ON/OFF signal as parallel operations rather than consecutive. Besides, the ON/OFF signal can be integrated into online prosthesis control systems. To demonstrate this, the hardware implementation has been included into a hierarchical control of a prosthetic hand (IH2); both validation tests on all the employed sensors, as well as the results of the online prosthetic control featuring the slip information, do highly encourage the use of the developed algorithm as a valuable solution for the prosthetic domain, and more in general, for the robotic one.

The slip algorithm, indeed, has been integrated into the real-time control of the IH2 hand during the experimentation on human amputee.

Tesi di dottorato in Bioingegneria e bioscienze, di Rocco Romeo,
discussa presso l'Università Campus Bio-Medico di Roma in data 16/10/2017.
La disseminazione e la riproduzione di questo documento sono consentite per scopi di didattica e ricerca,
a condizione che ne venga citata la fonte.

Chapter 5 Conclusions and future works

This Chapter contains the final discussion of the thesis results and the presentation of conclusion and future works.

The first part of this Chapter has the purpose to summarize the contents detailed in the previous chapters, while the second part wants to provide an idea on the future researches related to the work developed in this thesis.

5.1 Work overview

Given its capabilities, its sophisticated kinematics and dynamics, the human hand can be considered as the most complex organ of the human body after the brain. A crucial feature of the human hand (and more in generally, of the human body) is the sense of touch, which allows assessing object properties, e.g., size, shape texture, temperature, etc. The dexterity of hand manipulation is a distinctive feature of human beings that current humanoid robots can barely replicate. Nonetheless, natural hands can be regarded as a benchmark for the design of future artificial hands. The study of the human hand features is the starting point for the design and control of anthropomorphic robotic hands. To this end, force analysis during grasping is a fundamental issue to face while studying human grasping strategies, as well as robotic grasping capabilities. The development, of a set of three instrumented objects for evaluating the applied force during grasping has been illustrated. The objects embedded sensors for force measurement and an accelerometer for acceleration as well as orientation estimation. A printed electronic board has been wedged inside the objects, hosting the accelerometer and the connectors for interfacing with the force sensors; the board

served for collecting the outputs signals from the all the sensors, and was powered by an external power supply.

In order to guarantee an appropriate usage during experimental phases, the sensors embedded in all the instrumented objects have been calibrated; a static calibration has been done to retrieve the best fit curves of the force sensors, while the accelerometer has been calibrated so as to quantify its axis sensitivities and offsets. Such values are indispensable for using the accelerometer as an inclinometer, besides its traditional function of acceleration sensor.

After the calibration procedures, the reliability of the instrumented objects has been evaluated on the human hand tripod grasp object, and extended to the other two. Performed experiments have regarded: (i) comparison of the force sensors measurements with a ground truth (forces measured by a robotic hand); (ii) investigation of the accelerometer ability to detect slippage for different roughness values; (iii) assessment of grasp trials performed by a human subject with the object. Force measured by the robotic hand sensors have been 3.3584N (± 0.1404), whereas the corresponding force mean value recorded by FSRs was 3.3495N (± 0.1523), indicating a high precision in the force measurement. Furthermore, the accelerometer resulted to always detect the induced slippage events, boasting a 100% success rate both in automated tests and in the experimental campaign conducted with human healthy subjects at Centro Protesi INAIL, Vigorso di Budrio (BO), Italy.

The obtained results, both from preliminary evaluation and from the experimental session with human subjects, encourage to utilize the designed objects as evaluating tools for grasp capabilities in humans as well as in robotic hands. E.g., forces level obtained through a statistical

analysis on a high number of subjects might allow achieving a sort of reference for the implementation of hand prosthesis control systems.

Subsequently, the development of a tactile sensory system for the IH2 prosthetic hand has been shown. General criteria for the design of an artificial tactile sensory system have been discussed, and then the choice of the sensors to be used for the prosthesis sensorization has been presented according to such criteria.

CAD parts have been designed ex novo for the IH2 hand, as the original ones does not embed tactile sensors of any kind. The mechanical parts that have been redesigned have been the fingertips and the hand palmar cover, allowing now the stable placement of tactile sensors within them. All the new mechanical parts have been interfaced with silicon encapsulations/covers which convey the applied force onto the sensitive area of the sensors themselves and protect them from scratching or damaging in general.

Ad hoc electronics has been conceived for the data elaboration; both force and slippage signals have been processed by a dedicated PCB which has been purposely printed. The PCB served for processing both force and slip information.

Moreover, a theoretical method for the optimum positioning of the sensitive units in a tactile array has been presented. Such a method allows a tactile sensor array to achieve hyper spatial acuity when stimulated with a periodic ridged surface at constant velocity. Experimental validation has not been provided yet, although the method performance appears promising both with uncorrupted and noise-corrupted data.

The first step towards the utilization of a tactile sensory system on a hand prosthesis has been made, in a scenario where, also thanks to

neural stimulation, an amputee wearer is able to *sense* the grasped objects like the prosthesis is his own natural hand.

For this purpose, a novel method for detection of slippage events has been proposed; said method has been presented through a detailed description of its sub-blocks, which include simple operations such as digital filtering, rectification and envelope of the input signal. Such sub-blocks are cascaded in order to generate the ON/OFF signal. The method has been validated on different typologies of resistive sensors, i.e. piezo-resistive (MEMS and FSR sensors) and strain gauges; ad hoc automated set-ups have been conceived for this purpose. The employed sensors have been both mono-axial, providing only the normal component of the applied force, and three-axial, providing the tangential forces as well as the normal one.

Both hardware and software implementation of the proposed method have been realized. The first one relies on digital operations performed via software, such as digital IIR causal filters that commonly feature non-linear phase and a thus a nonzero delay between the original signal and the filtered one. The second is based on a PCB on which all the algorithm operations are performed (with some modifications), except the ON/OFF signal generation. The latter is again generated via software. Validation tests on MEMS sensors and strain gauge sensors (JR3) have been executed by means of the software implementation, while for the FSR sensors it has been used the hardware solution. Relative movement inferior than 5 μm between the sensor and the contact surface have resulted to be detectable through the developed algorithm, with true positives detected in 100% of the cases, with minimum average delays lower than 50 ms.

The main advantage of the algorithm is that it makes use of just one input signal (e.g., the normal force) measured through a resistive sensor, leading to an ON/OFF slip information. It is not necessary to employ the force value to apply the method on: the raw output voltage (relating to the force) can be used, retrieving the force value and generating the ON/OFF signal as parallel operations rather than consecutive. Besides, the ON/OFF signal can be integrated into online prosthesis control systems. To demonstrate this, the hardware implementation has been included into a hierarchical control of a prosthetic hand (IH2); different objects have been grasped by the prosthetic hand, being subsequently disturbed and induced to slip by a seven DOF robot. The algorithm has allowed the prosthetic hand to maintain a stable grasp in all cases, failing only in 1/48 (2.08%) trials with enabled slip control. Both validation tests on all the employed sensors, as well as the results of the online prosthetic control featuring the slip information, do highly encourage the use of the developed algorithm as a valuable solution for the prosthetic domain, and more in general, for the robotic one.

5.2 Future works

Next steps will regard the following activities:

- utilization of the developed instrumented objects for further experimental sessions of biomechanical analysis, involving a larger number of subjects (both healthy and amputee). The inclusion in the experiments of robotic hands such as iLimb, Bebionic, Michelangelo and IH2 has also been considered, as well as the development of new instrumented objects;
- analysis of the data collected in the experimentation on the amputee subject, focusing on the performance of the tactile sensory system developed for the IH2 Hand. Sensorization of

other prosthetic hands, such as the ones above mentioned, has been considered. Future experimentations will foresee the employment of wireless technologies to operate a considerable reduction of the encumbrance due to cables, as well as to supplementary devices required for the experiments;

- further, the experimental validation of the presented method for the optimum positioning of sensitive units in a tactile array will be performed by means of a purposely conceived set-up, which will foresee the use of several sensors typologies (such as piezo-resistive, optical etc.);
- use of additional sensors, with different technologies, to test the presented slippage detection method on, with the aim of extending its validity beyond the resistive domain;

The obtained results suggest the idea to use the instrumented objects in wide experimental sessions. In fact, forces level obtained through a statistical analysis on a high number of subjects, together with kinematic data gathered thanks to colored markers, might broaden the understanding of the human grasp strategies. Moreover, the combined analysis of grasp kinematics and force information also allows evaluating robot grasping capabilities, providing useful insights into the development of grasping algorithms; e.g., such information can be assumed as a sort of reference for the implementation of hand prosthesis control systems.

Finally, the development of new instrumented objects with different shapes and dimensions for studying other grasp tasks than bipod and tripod ones is under evaluation.

An experimentation on human amputee subject has recently terminated, leading to a three months implant on an amputee subject

of bi-directional invasive neural interfaces to the (PNS). The sensorization of further available prosthetic hands is being considered as well, in order to spread this possibility to different prosthetic devices and to repeat similar experimentations on human subjects.

Although the slippage detection method proposed herein has been rigorously validated, experimental tests have concerned resistive sensors only; a reasonable step is to extend the validation tests on different technologies, such as capacitive, optical et., augmenting the already good generality of the method.

Tesi di dottorato in Bioingegneria e bioscienze, di Rocco Romeo,
discussa presso l'Università Campus Bio-Medico di Roma in data 16/10/2017.
La disseminazione e la riproduzione di questo documento sono consentite per scopi di didattica e ricerca,
a condizione che ne venga citata la fonte.

Bibliography

(Abhinav, 2009) Abhinav, V., and S. Vivekanandan. "Real-time intelligent gripping system for dexterous Manipulation of Industrial Robots." *Proceedings of the World Congress on Engineering*. Vol. 2. 2009.

(Adnan, 2013) Adnan, Nazrul H., et al. "Accurate and Effective Method to Smoothen Grasping Force Signal of GloveMAP using Gaussian Filter." (2013).

(Agur, 1999) Agur, Anne MR, and Ming J. Lee. "Grant's Atlas of anatomy 10th ed." (1999).

(Allen, 1990) Allen, Peter K., et al. "A system for programming and controlling a multisensor robotic hand." *IEEE Transactions on Systems, Man, and Cybernetics* 20.6 (1990): 1450-1456.

(Athenstaedt, 1982) Athenstaedt, Herbert, et al. "Epidermis of human skin: pyroelectric and piezoelectric sensor layer." *Science* 216.4549 (1982): 1018-1020.

(Barone, 2016) Barone, Roberto, et al. "Multilevel control of an anthropomorphic prosthetic hand for grasp and slip prevention." *Advances in Mechanical Engineering* 8.9 (2016).

(Baud-Bovy, 2001) Baud-Bovy, Gabriel, and John F. Soechting. "Two virtual fingers in the control of the tripod grasp." *Journal of Neurophysiology* 86.2 (2001): 604-615.

(Biddiss, 2007) Biddiss, Elaine, et al. "Consumer design priorities for upper limb prosthetics." *Disability and Rehabilitation: Assistive Technology* 2.6 (2007): 346-357.

(Borton, 2014) Borton, David, et al. "Corticospinal neuroprostheses to restore locomotion after spinal cord injury." *Neuroscience research* 78 (2014): 21-29.

(Brindley, 1968) Brindley, Giles S., and W. S. Lewin. "The sensations produced by electrical stimulation of the visual cortex." *The Journal of physiology* 196.2 (1968): 479.

(Brugger, 2011) Brugger, Dominik, et al. "Real-time adaptive microstimulation increases reliability of electrically evoked cortical potentials." *IEEE Transactions on Biomedical Engineering* 58.5 (2011): 1483-1491.

(Bullock, 2011) Bullock, Ian M., and Aaron M. Dollar. "Classifying human manipulation behavior." *Rehabilitation Robotics (ICORR), 2011 IEEE International Conference on*. IEEE, 2011.

(Burstedt, 1999) Burstedt, Magnus KO, et al. "Control of grasp stability in humans under different frictional conditions during multidigit manipulation." *Journal of neurophysiology* 82.5 (1999): 2393-2405.

(Campolo, 2006) Campolo, D., et al. "A novel procedure for in-field calibration of sourceless inertial/magnetic orientation tracking wearable devices." *Biomedical Robotics and Biomechatronics, 2006. BioRob 2006. The First IEEE/RAS-EMBS International Conference on*. IEEE, 2006.

(Ciancio, 2016) Ciancio, Anna Lisa, et al. "Control of prosthetic hands via the peripheral nervous system." *Frontiers in neuroscience* 10 (2016).

(Chappell, 2011) Chappell, P. H. "Making sense of artificial hands." *Journal of medical engineering & technology* 35.1 (2011): 1-18.

(Choi, 2005) Choi, Byungjune, et al. "Development of fingertip tactile sensor for detecting normal force and slip." *International Conference on Control, Automation and Systems*. 2005.

(Cipriani, 2011) Cipriani, Christian, et al. "The SmartHand transradial prosthesis." *Journal of neuroengineering and rehabilitation* 8.1 (2011): 29.

(Cloutier, 2013) Cloutier, Aimee, and James Yang. "Design, control, and sensory feedback of externally powered hand prostheses: a literature review." *Critical Reviews™ in Biomedical Engineering* 41.2 (2013).

(Cordella, 2012) Cordella, F., et al. "A bio-inspired grasp optimization algorithm for an anthropomorphic robotic hand." *International Journal on Interactive Design and Manufacturing* 6.2 (2012): 113-122.

(Cotton, 2007) Cotton, Darryl PJ, et al. "A novel thick-film piezoelectric slip sensor for a prosthetic hand." *IEEE sensors journal* 7.5 (2007): 752-761.

(Cutkosky, 1989) Cutkosky, Mark R. "On grasp choice, grasp models, and the design of hands for manufacturing tasks." *IEEE Transactions on robotics and automation* 5.3 (1989): 269-279.

(Dahiya, 2009) Dahiya, Ravinder S., et al. "Tactile sensing—from humans to humanoids." *IEEE Transactions on Robotics* 26.1 (2009): 1-20.

(Dahiya, 2013) Dahiya, Ravinder S., and Maurizio Valle. "Tactile sensing technologies." *Robotic Tactile Sensing*. Springer Netherlands, 2013. 79-136.

(Dargahi, 2004) Dargahi, J., and S. Najarian. "Human tactile perception as a standard for artificial tactile sensing—a review." *The International Journal of Medical Robotics and Computer Assisted Surgery* 1.1 (2004): 23-35.

(Dario, 1989) Dario, Paolo. "Tactile sensing for robots: Present and future." *The robotics review I*. MIT Press, 1989.

(De Maria, 2012) De Maria, Giuseppe, et al. "Tactile sensor for human-like manipulation." *Biomedical Robotics and Biomechanics (BioRob), 2012 4th IEEE RAS & EMBS International Conference on*. IEEE, 2012.

(De Rossi, 1986) De Rossi, D., C. Domenici, and P. Pastacaldi. "Piezoelectric properties of dry human skin." *IEEE transactions on electrical insulation* 3 (1986): 511-517.

(Dhillon, 2005) Dhillon, Gurpreet Singh, and Kenneth W. Horch. "Direct neural sensory feedback and control of a prosthetic arm." *IEEE transactions on neural systems and rehabilitation engineering* 13.4 (2005): 468-472.

(Engeberg, 2013) Engeberg, Erik D., and Sanford G. Meek. "Adaptive sliding mode control for prosthetic hands to simultaneously prevent slip and minimize deformation of grasped objects." *IEEE/ASME Transactions on Mechatronics* 18.1 (2013): 376-385.

(Fernandez, 2014) Fernandez, Raul, et al. "Micro-vibration-based slip detection in tactile force sensors." *Sensors* 14.1 (2014): 709-730.

(Figliola, 2015) Figliola, Richard S., and Donald Beasley. *Theory and design for mechanical measurements*. John Wiley & Sons, 2015.

(Fishel, 2012) Fishel, Jeremy A., and Gerald E. Loeb. "Sensing tactile microvibrations with the BioTac—Comparison with human sensitivity." *Biomedical Robotics and Biomechanics (BioRob), 2012 4th IEEE RAS & EMBS International Conference on*. IEEE, 2012.

(Flanagan, 1993) Flanagan, J. Randall, and Alan M. Wing. "Modulation of grip force with load force during point-to-point arm movements." *Experimental Brain Research* 95.1 (1993): 131-143.

(Flanagan, 1999) Flanagan, J. Randall, et al. "Control of fingertip forces in multidigit manipulation." *Journal of neurophysiology* 81.4 (1999): 1706-1717.

(Francomano, 2013) Francomano, Maria Teresa, et al. "Artificial sense of slip—A review." *IEEE Sensors Journal* 13.7 (2013): 2489-2498.

(Fuentes, 2009) Fuentes, Romulo, et al. "Spinal cord stimulation restores locomotion in animal models of Parkinson's disease." *Science* 323.5921 (2009): 1578-1582.

(Gad, 2013) Gad, Parag, et al. "Development of a multi-electrode array for spinal cord epidural stimulation to facilitate stepping and standing after a complete spinal cord injury in adult rats." *Journal of neuroengineering and rehabilitation* 10.1 (2013): 2.

(Galvani, 1797) Galvani, L. "Memorie sulla elettricit animale". Bologna Per le stampe del Sassi 7 (1797):363–418.

(Graziano, 2002) Graziano, M. S. A., and M. M. Botvinick. "Common Mechanisms in Perception and Action: Attention and Performance." (2002).

(Greenwald, 2016) Greenwald, Elliot, et al. "Implantable neurotechnologies: bidirectional neural interfaces—applications and VLSI circuit implementations." *Medical & biological engineering & computing* 54.1 (2016): 1-17.

(Gunji, 2007) Gunji, Daisuke, et al. "Grasping force control of multi-fingered robot hand based on slip detection using tactile sensor." *Journal of the Robotics Society of Japan* 25.6 (2007): 970-978.

(Guyton, 1961) Guyton, Arthur C. "Textbook of medical physiology." *Academic Medicine* 36.5 (1961): 556.

(Harkema, 2011) Harkema, Susan, et al. "Effect of epidural stimulation of the lumbosacral spinal cord on voluntary movement, standing, and assisted stepping after motor complete paraplegia: a case study." *The Lancet* 377.9781 (2011): 1938-1947.

(Hendrich, 2010) Hendrich, Norman, et al. "Multi-sensor based segmentation of human manipulation tasks." *Multisensor Fusion and Integration for Intelligent Systems (MFI), 2010 IEEE Conference on*. IEEE, 2010.

(Herrera, 2007) Herrera, Rosana Matuk. "A bio-inspired method for incipient slip detection." *Australasian Joint Conference on Artificial Intelligence*. Springer Berlin Heidelberg, 2007.

(Hodgkin, 1952) Hodgkin, Alan L., and Andrew F. Huxley. "A quantitative description of membrane current and its application to conduction and excitation in nerve." *The Journal of physiology* 117.4 (1952): 500.

(Howe, 1989) Howe, Robert D., and Mark R. Cutkosky. "Sensing skin acceleration for slip and texture perception." *Robotics and Automation, 1989. Proceedings., 1989 IEEE International Conference on*. IEEE, 1989.

(Howe, 1993) Howe, Robert D. "Tactile sensing and control of robotic manipulation." *Advanced Robotics* 8.3 (1993): 245-261.

(Howleg, 1996) Holweg, E. G. M., et al. "Slip detection by tactile sensors: Algorithms and experimental results." *Robotics and Automation, 1996. Proceedings., 1996 IEEE International Conference on*. Vol. 4. IEEE, 1996.

(Jones, 2006) Jones, Lynette A., and Susan J. Lederman. *Human hand function*. Oxford University Press, 2006.

(Johansson, 1979) Johansson, Roland S., and Å. B. Vallbo. "Tactile sensibility in the human hand: relative and absolute densities of four types of mechanoreceptive units in glabrous skin." *The Journal of physiology* 286.1 (1979): 283-300.

(Johansson, 1984) Johansson, R. S., and G. Westling. "Roles of glabrous skin receptors and sensorimotor memory in automatic control of precision grip when lifting rougher or more slippery objects." *Experimental brain research* 56.3 (1984): 550-564.

(Johansson, 1994) Johansson, Roland S., and Kelly J. Cole. "Grasp stability during manipulative actions." *Canadian journal of physiology and pharmacology* 72.5 (1994): 511-524.

(Kappasov, 2015) Kapassov, Zhanat, et al. "Tactile sensing in dexterous robot hands—Review." *Robotics and Autonomous Systems* 74 (2015): 195-220.

(Kargov, 2004) Kargov, Artem, et al. "A comparison of the grip force distribution in natural hands and in prosthetic hands." *Disability and Rehabilitation* 26.12 (2004): 705-711.

(Kawamura, 2013) Kawamura, Takuya, et al. "Measurement of slip, force and deformation using hybrid tactile sensor system for robot hand gripping an object." *International Journal of Advanced Robotic Systems* 10.1 (2013): 83.

(Kawasaki, 2002) Kawasaki, Haruhisa, et al. "Dexterous anthropomorphic robot hand with distributed tactile sensor: Gifu hand II." *IEEE/ASME transactions on mechatronics* 7.3 (2002): 296-303.

(Keller, 2000) Keller, T., et al. "A system for measuring finger forces during grasping." *Proceedings of International Functional Electrical Stimulation Society (IFESS 2000) Conference, Aalborg, Denmark. 2000.*

(Klatzky, 2003) Klatzky, Roberta L., and Susan J. Lederman. "Touch." *Handbook of psychology* (2003).

(Koiva, 2011) Koiva, Risto, Robert Haschke, and Helge Ritter. "Development of an intelligent object for grasp and manipulation research." *Advanced Robotics (ICAR), 2011 15th International Conference on. IEEE, 2011.*

(LaMotte, 1987) LaMotte, Robert H., and Mandayam A. Srinivasan. "Tactile discrimination of shape: responses of slowly adapting mechanoreceptor afferents to a step stroked across the monkey fingerpad." *Journal of Neuroscience* 7.6 (1987): 1655-1671.

(Lee, 1999) Lee, Yong Kwun, and Isao Shimoyama. "A skeletal framework artificial hand actuated by pneumatic artificial muscles." *Robotics and Automation, 1999. Proceedings. 1999 IEEE International Conference on. Vol. 2. IEEE, 1999.*

(Liberson, 1961) Liberson, W. T., et al. "Functional electrotherapy: stimulation of the peroneal nerve synchronized with the swing phase of the gait of hemiplegic patients." *Archives of physical medicine and rehabilitation* 42 (1961): 101-105.

(Liu, 2008) Liu, Hong, et al. "Multisensory five-finger dexterous hand: The DLR/HIT Hand II." *Intelligent Robots and Systems, 2008. IROS 2008. IEEE/RSJ International Conference on. IEEE, 2008.*

(Loomis, 1986) Loomis, Jack M., and Susan J. Lederman. "Tactual perception." *Handbook of perception and human performances 2* (1986): 2.

(Lotti, 2004) Lotti, F., et al. "Ubh 3: A biologically inspired robotic hand." *IEEE Int. Conf. on Intelligent Manipulation and Grasping*. 2004.

(Macefield, 1996) Macefield, Vaughan G., and Ronald S. Johansson. "Control of grip force during restraint of an object held between finger and thumb: responses of muscle and joint afferents from the digits." *Experimental brain research* 108.1 (1996): 172-184.

(Maeno, 1998) Maeno, Takashi, et al. "Relationship between the structure of human finger tissue and the location of tactile receptors." *JSME International Journal Series C Mechanical Systems, Machine Elements and Manufacturing* 41.1 (1998): 94-100.

(Martell, 2007) Martell, J., and Giuseppina Gini. "Robotic hands: Design review and proposal of new design process." *Image* 180 (2007): 9270.

(Masuda, 1976) Masuda, Ryosuke, Kensuke Hasegawa, and Kazuyoshi Osako. "Slip sensor of industrial robot and its application." *Electrical Engineering in Japan* 96.5 (1976): 129-136.

(Matsuo, 2008) Matsuo, Kazuya, et al. "A decision method for the placement of mechanical tactile elements for grasp type recognition." *Sensors, 2008 IEEE*. IEEE, 2008.

(Memberg, 1995) Memberg, William D., and Patrick E. Crago. "A grasp force and position sensor for the quantitative evaluation of neuroprosthetic hand grasp systems." *IEEE Transactions on rehabilitation engineering* 3.2 (1995): 175-181.

(Memberg, 1997) Memberg, William D., and Patrick E. Crago. "Instrumented objects for quantitative evaluation of hand grasp." *Journal of rehabilitation research and development* 34.1 (1997): 82.

(Mingrino, 1994) Mingrino, A., et al. "Slippage control in hand prostheses by sensing grasping forces and sliding motion." *Intelligent Robots and Systems' 94. 'Advanced Robotic Systems and the Real World', IROS'94. Proceedings of the IEEE/RSJ/GI International Conference on*. Vol. 3. IEEE, 1994.

(Mouri, 2002) Mouri, Tetsuya, et al. "Anthropomorphic robot hand: Gifu hand III." *Proc. Int. Conf. ICCAS*. 2002.

(Nicholls, 1999) Nicholls, H., and M. Lee. "Tactile sensing for mechatronics-a state of the art survey." *Mechatronics* 9 (1999): 1-32.

(Nag, 2016) Nag, Sudip, and Nitish V. Thakor. "Implantable neurotechnologies: electrical stimulation and applications." *Medical & biological engineering & computing* 54.1 (2016): 63-76.

(Ninu, 2014) Ninu, Andrei, et al. "Closed-loop control of grasping with a myoelectric hand prosthesis: Which are the relevant feedback variables for force control?." *IEEE transactions on neural systems and rehabilitation engineering* 22.5 (2014): 1041-1052.

NLLIC (National Limb Loss Information Center) (2007). *Fact Sheet: Limb Loss in the United States*. Knoxville, TN: Amputee Coalition of America.

(Oddo, 2009) Oddo, Calogero M., et al. "A biomimetic MEMS-based tactile sensor array with fingerprints integrated in a robotic fingertip for artificial roughness encoding." *Robotics and Biomimetics (ROBIO), 2009 IEEE International Conference on*. IEEE, 2009.

(Oddo, 2011a) Oddo, Calogero M., et al. "Roughness encoding for discrimination of surfaces in artificial active-touch." *IEEE Transactions on Robotics* 27.3 (2011): 522-533.

(Oddo, 2011b) Oddo, Calogero Maria, et al. "A mechatronic platform for human touch studies." *Mechatronics* 21.3 (2011): 604-613.

(Oddo, 2016) Oddo, Calogero Maria, et al. "Intraneural stimulation elicits discrimination of textural features by artificial fingertip in intact and amputee humans." *Elife* 5 (2016): e09148.

(Palanker, 2005) Palanker, Daniel, et al. "Design of a high-resolution optoelectronic retinal prosthesis." *Journal of neural engineering* 2.1 (2005): S105.

(Pasluosta, 2012) Pasluosta, Cristian F., and Alan WL Chiu. "Evaluation of a neural network-based control strategy for a cost-effective externally-powered prosthesis." *Assistive Technology* 24.3 (2012): 196-208.

(Persichetti, 2007) Persichetti, A., et al. "Optoelectronic-based flexible contact sensor for prosthetic hand application." *Rehabilitation Robotics, 2007. ICORR 2007. IEEE 10th International Conference on*. IEEE, 2007.

(Polasek, 2009) Polasek, Katharine H., et al. "Stimulation stability and selectivity of chronically implanted multicontact nerve cuff electrodes in the human upper extremity." *IEEE Transactions on Neural Systems and Rehabilitation Engineering* 17.5 (2009): 428-437.

(Pons, 1999) Pons, J. L., et al. "Multifingered dextrous robotics hand design and control: a review." *Robotica* 17.06 (1999): 661-674.

(Radwin, 1992) Radwin, Robert G., et al. "External finger forces in submaximal five-finger static pinch prehension." *Ergonomics* 35.3 (1992): 275-288.

(Raspopovic, 2014) Raspopovic, Stanisa, et al. "Restoring natural sensory feedback in real-time bidirectional hand prostheses." *Science translational medicine* 6.222 (2014).

(Roa, 2012) Roa, Maximo A., et al. "Experimental evaluation of human grasps using a sensorized object." *Biomedical Robotics and Biomechanics (BioRob), 2012. 4th IEEE RAS & EMBS International Conference on*. IEEE, 2012.

(Rodriguez-Cheu, 2006) Rodriguez-Cheu, Luis E., and Alícia Casals. "Sensing and control of a prosthetic hand with myoelectric feedback." *Biomedical Robotics and Biomechanics, 2006. BioRob 2006. The First IEEE/RAS-EMBS International Conference on*. IEEE, 2006.

(Rodriguez-Cheu, 2008) Rodriguez-Cheu, L. E., et al. "Result of a perceptual feedback of the grasping forces to prosthetic hand users." *Biomedical Robotics and Biomechanics, 2008. BioRob 2008. 2nd IEEE RAS & EMBS International Conference on*. IEEE, 2008.

(Romeo, 2015) Romeo, Rocco A., et al. "Development and preliminary testing of an instrumented object for force analysis during grasping." *Engineering in Medicine and Biology Society, 2015. 37th Annual International Conference of the IEEE*. IEEE, 2015.

(Romeo, 2017a) Romeo, Rocco A., et al. "An instrumented object for studying human grasping." *Rehabilitation Robotics, 2017. 15th International Conference on*. IEEE, 2017.

(Romeo, 2017b) Romeo, Rocco A., et al. "Slippage detection with piezoresistive tactile sensors". *Sensors* (2017).

(Rossini, 2010) Rossini, Paolo M., et al. "Double nerve intraneural interface implant on a human amputee for robotic hand control." *Clinical neurophysiology* 121.5 (2010): 777-783.

(Schwarz, 1955) Schwarz, Robert J. "The anatomy and mechanics of the human hand." *Artificial limbs* 22 (1955).

(Serio, 2014) Serio, Alessandro, et al. "The patched intrinsic tactile object: A tool to investigate human grasps." *Intelligent Robots and Systems (IROS 2014), 2014 IEEE/RSJ International Conference on*. IEEE, 2014.

(Saccomandi, 2014) Saccomandi, Paola, et al. "Microfabricated tactile sensors for biomedical applications: a review." *Biosensors* 4.4 (2014): 422-448.

(Sayenko, 2014) Sayenko, Dmitry G., et al. "Neuromodulation of evoked muscle potentials induced by epidural spinal-cord stimulation in paralyzed individuals." *Journal of neurophysiology* 111.5 (2014): 1088-1099.

(Schiefer, 2013) Schiefer, Matthew A., et al. "Selective activation of the human tibial and common peroneal nerves with a flat interface nerve electrode." *Journal of neural engineering* 10.5 (2013).

(Su, 2015) Su, Zhe, et al. "Force estimation and slip detection/classification for grip control using a biomimetic tactile sensor." *Humanoid Robots (Humanoids), 2015 IEEE-RAS 15th International Conference on*. IEEE, 2015.

(Tan, 2014) Tan, Daniel W., et al. "A neural interface provides long-term stable natural touch perception." *Science translational medicine* 6.257 (2014).

(Teshigawara, 2010) Teshigawara, Seiichi, et al. "High sensitivity initial slip sensor for dexterous grasp." *Robotics and Automation (ICRA), 2010 IEEE International Conference on*. IEEE, 2010.

(Tremblay, 1992) Tremblay, M. R., et al. "*Utilizing sensed incipient slip signals for grasp force control.*" STANFORD UNIV CA CENTER FOR DESIGN RESEARCH, 1992.

(Tremblay, 1993) Tremblay, Marc R., and Mark R. Cutkosky. "Estimating friction using incipient slip sensing during a manipulation task." *Robotics and Automation, 1993. Proceedings., 1993 IEEE International Conference on.* IEEE, 1993.

(Tura, 1998) Tura, Andrea, et al. "Experimental development of a sensory control system for an upper limb myoelectric prosthesis with cosmetic covering." *Journal of Rehabilitation Research and Development* 35.1 (1998): 14.

(Tyler, 2003) Tyler, Dustin J., and Dominique M. Durand. "Chronic response of the rat sciatic nerve to the flat interface nerve electrode." *Annals of biomedical engineering* 31.6 (2003): 633-642.

(Van Ho, 2013) Ho, Anh-Van, and Shinichi Hirai. *Mechanics of Localized Slippage in Tactile Sensing: And Application to Soft Sensing Systems.* Vol. 99. Springer, 2013.

(Wettels, 2009) Wettels, Nicholas, et al. "Grip control using biomimetic tactile sensing systems." *IEEE/ASME Transactions On Mechatronics* 14.6 (2009): 718-723.

(Wenger, 2014) Wenger, Nikolaus, et al. "Closed-loop neuromodulation of spinal sensorimotor circuits controls refined locomotion after complete spinal cord injury." *Science translational medicine* 6.255 (2014).

(Wesley, 1871) Wesley, John. *The Desideratum: or, electricity made plain and useful.* Baillière, Tindall, and Cox, 1871.

(Yamada, 1994) Yamada, Yoji, and Mark R. Cutkosky. "Tactile sensor with 3-axis force and vibration sensing functions and its application to detect rotational slip." *Robotics and Automation, 1994. Proceedings., 1994 IEEE International Conference on.* IEEE, 1994.

Tesi di dottorato in Bioingegneria e bioscienze, di Rocco Romeo,
discussa presso l'Università Campus Bio-Medico di Roma in data 16/10/2017.
La disseminazione e la riproduzione di questo documento sono consentite per scopi di didattica e ricerca,
a condizione che ne venga citata la fonte.

List of publications

Peer-reviewed journals

P. Saccomandi, C. M. Oddo, L. Zollo, D. Formica, **R. A. Romeo**, C. Massaroni, M. A. Caponero, N. Vitiello, E. Guglielmelli, S. Silvestri and E. Schena, ‘‘Feedforward neural network for force coding of an MRI-compatible tactile sensor array based on Fiber Bragg Grating’’, Journal of Sensors, 2015.

A.L. Ciancio, F. Cordella, R. Barone, **R. A. Romeo**, A. Dellacasa Bellingegni, R. Sacchetti, A. Davalli, G. Di Pino, F. Ranieri, V. Di Lazzaro, E. Guglielmelli, L. Zollo, ‘‘Literature Review of peripheral nervous system based Control of Prosthetic Hands: Part I – Control, Sensorization and Clinical Validation’’, Frontiers in Neuroscience, 2016.

R. Barone, **R.A. Romeo**, A.L. Ciancio, A. Davalli, R. Sacchetti, E. Guglielmelli and L. Zollo, ‘‘Multilevel control of an anthropomorphic prosthetic hand for grasp and slip prevention’’, Advances in Mechanical Engineering, 2016.

R.A. Romeo, C.M. Oddo, M.C. Carrozza, E. Guglielmelli and L. Zollo ‘‘Slippage detection with piezoresistive tactile sensors’’, Sensors, 2017.

R.A. Romeo, E. Guglielmelli and L. Zollo, ‘‘On the techniques for sensing slippage with artificial hands: a review’’, in preparation.

International Conferences

R.A. Romeo, F. Cordella, L. Zollo, D. Formica, P. Saccomandi, E. Schena, G. Carpino, A. Davalli, R. Sacchetti and E. Guglielmelli, ‘‘Development and preliminary testing of an instrumented object for force analysis during grasping’’, 37th Annual International Conference of the IEEE Engineering in Medicine and Biology Society, Milan, 2015.

R.A. Romeo, F. Cordella, A. Davalli, R. Sacchetti, E. Guglielmelli and L. Zollo, ‘‘An instrumented object for studying human grasping’’, 15th IEEE International Conference on Rehabilitation Robotics, London, 2017.

National Conferences

F. Cordella, **R.A. Romeo**, A.G. Cutti, R. Sacchetti, A. Davalli, E. Guglielmelli, L. Zollo "Experimental framework for human hand biomechanical analysis", V Congresso del Gruppo Nazionale di Bioingegneria (GNB), June 20-22, 2016, Naples, Italy.

A.L. Ciancio, R.Barone, **R.A. Romeo**, A. Davalli, R. Sacchetti, E. Guglielmelli, L. Zollo, "Multilevel control of an anthropomorphic prosthetic hand for grasp and slip prevention", V Congresso del Gruppo Nazionale di Bioingegneria (GNB), June 20-22, 2016, Naples, Italy.

Patents

(#1) C.M. Oddo, **R.A. Romeo**, L. Zollo, E. Guglielmelli, L. Beccai, "Method for positioning the units of an array of tactile sensors for obtaining a hyper spatial acuity and processing method thereof", 2016, (patent pending n°102016000076248).

(#2) **R.A. Romeo**, L. Zollo, E. Guglielmelli, R. Sacchetti, A. Davalli, "Method for slippage detection between two surfaces", 2016, (patent pending n°102016000105302).